Issue 2 2025 | Volume 21

The Journal on Advanced Studies in Theoretical and Experimental Physics, including Related Themes from Mathematics

PROGRESS IN PHYSICS

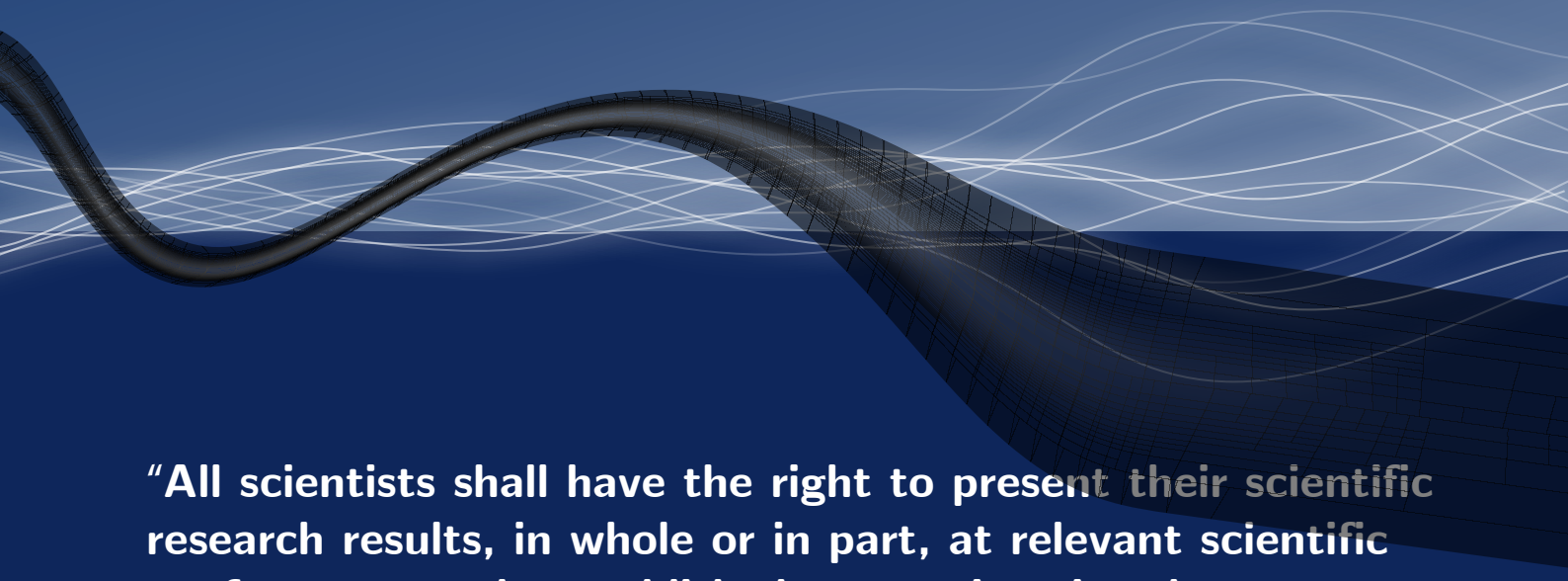

"All scientists shall have the right to present their scientific research results, in whole or in part, at relevant scientific conferences, and to publish the same in printed scientific journals, electronic archives, and any other media." — Declaration of Academic Freedom, Article 8

ISSN 1555-5534

PROGRESS IN PHYSICS

A Scientific Journal on Advanced Studies in Theoretical and Experimental Physics, including Related Themes from Mathematics. This journal is registered with the Library of Congress (DC, USA).

Electronic version of this journal:
https://www.progress-in-physics.com

Postal Address

Department of Mathematics and Science,
University of New Mexico,
705 Gurley Ave., Gallup, NM 87301, USA

ISSN: 1555-5534 (print)
ISSN: 1555-5615 (online)

Standard Address Number: 297-5092
Printed in the United States of America

December 2025 **Vol. 21, Issue 2**

CONTENTS

Information for Authors

Progress in Physics has been created for rapid publications on advanced studies in theoretical and experimental physics, including related themes from mathematics and astronomy. All submitted papers should be professional, in good English, containing a brief review of a problem and obtained results.

All submissions should be designed in LaTeX format using *Progress in Physics* template. This template can be downloaded from *Progress in Physics* home page.

Preliminary, authors may submit papers in PDF format. If the paper is accepted, authors can manage LaTeXtyping. Do not send MS Word documents, please: we do not use this software, so unable to read this file format. Incorrectly formatted papers (i.e. not LaTeXwith the template) will not be accepted for publication. Those authors who are unable to prepare their submissions in LaTeXformat can apply to a third-party payable service for LaTeX typing. Our personnel work voluntarily. Authors must assist by conforming to this policy, to make the publication process as easy and fast as possible.

Abstract and the necessary information about author(s) should be included into the papers. To submit a paper, mail the file(s) to the Editor-in-Chief.

All submitted papers should be as brief as possible. Short articles are preferable. Large papers can also be considered. Letters related to the publications in the journal or to the events among the science community can be applied to the section *Letters to Progress in Physics*.

All that has been accepted for the online issue of *Progress in Physics* is printed in the paper version of the journal. To order printed issues, contact the Editors.

Authors retain their rights to use their papers published in *Progress in Physics* as a whole or any part of it in any other publications and in any way they see fit. This copyright agreement shall remain valid even if the authors transfer copyright of their published papers to another party.

Electronic copies of all papers published in *Progress in Physics* are available for free download, copying, and re-distribution, according to the copyright agreement printed on the titlepage of each issue of the journal. This copyright agreement follows the *Budapest Open Initiative* and the *Creative Commons Attribution-Noncommercial-No Derivative Works 2.5 License* declaring that electronic copies of such books and journals should always be accessed for reading, download, and copying for any person, and free of charge.

Consideration and review process does not require any payment from the side of the submitters. Nevertheless the authors of accepted papers are requested to pay the page charges. *Progress in Physics* is a non-profit/academic journal: money collected from the authors cover the cost of printing and distribution of the annual volumes of the journal along the major academic/university libraries of the world. (Look for the current author fee in the online version of *Progress in Physics*.)

LETTERS TO PROGRESS IN PHYSICS

On the Astronomical Observations of Instant Transmission of Signals from Stars and Their Explanation in the Framework of General Relativity

Dmitri Rabounski and Larissa Borissova
Puschino, Moscow Region, Russia. E-mail: rabounski@yahoo.com; lborissova@yahoo.com

This article discusses the astronomical observations of instant transmission of signals from stars (long-range action), performed in 1977–1979 by Prof. N. A. Kozyrev. It is shown that stopping physically observable time, which is a necessary condition for instant transmission of a signal, is impossible in the Minkowski space (which is the space-time of Special Relativity) due to its geometric structure, i.e., the very structure of the Minkowski space does not allow long-range action. On the other hand, this is possible in the space-time of General Relativity due to the presence of the gravitational field potential or the rotation of space (due to the non-orthogonality of time lines to the three-dimensional spatial section), or both of these factors presented together. Thus, Kozyrev's astronomical observations of instant transmission of signals from stars (long-range action) find their explanation in the space-time of General Relativity.

1 Experimental results

Nikolai A. Kozyrev (1908, St. Petersburg — 1983, ibid.) was one of the most productive astronomers of the 20th century, best known due to his discovery of volcanism on the Moon in 1958 [1] and the atmosphere of Mercury in 1963 [2]. For the discovery of lunar volcanism, Kozyrev was awarded the gold medal of the International Academy of Astronautics, encrusted with seven diamonds in the form of stars of the constellation Ursa Major (Paris, 1969). Prof. Kozyrev worked at the Pulkovo Astronomical Observatory near St. Petersburg. Read about him in the *Encyclopaedia Britannica* [3] and in a detailed biography for his 100th birthday [4].

In addition to his studies in astronomy, Kozyrev in 1958 introduced the "causal or asymmetrical mechanics" [5] that takes the physical properties of time into account. Continuing this research, he described his many years of experimental research on this topic [6, 7]. In particular, Kozyrev arrived at the conclusion about the possibility of astronomical observations using the physical properties of time [8].

The apotheosis of this research were the astronomical observations using the 50-inch reflecting telescope of the Crimean Astronomical Observatory, during which in 1977–1979 Kozyrev registered the effect of long-range action, i.e., the instant transmission of signals from stars [9, 10].* His astronomical observations were then reproduced and successfully confirmed in 1989 [11, 12] by a group of scientists, headed by Irène A. Eganova and Michael M. Lavrent'ev from the Sobolev Institute of Mathematics (Novosibirsk).

Since the original two papers [9, 10] in which Kozyrev reported the instant transmission of signals from stars were published in Russian, and the reports [11, 12] confirming his results are only short communications from the USSR Academy of Sciences (in English), we must first explain the details of Kozyrev's astronomical observations.

Based on his previous research into the causal or asymmetric mechanics [5], Kozyrev concluded that time has different speeds at different points of space depending on the active processes of destruction or creation (increase or decrease in the level of entropy) at these points.† Kozyrev considered the field of distribution of time speeds around active processes of destruction or creation as one of the physical properties of time, which he called the *field of time density* [6, 7]. By this he meant that time is not just the fourth coordinate of space-time, but a real physical field, the non-uniformity of which can affect physical bodies and the processes occurring in them. Therefore, Kozyrev concluded, around any star there must be a field of time speeds (a field of time density) due to the active processes of destruction (loss of organization of stellar substance) occurring in it.

Since time does not spread, Kozyrev reasoned, but appears instantly throughout the entire three-dimensional space of the Universe (which is an instant three-dimensional section of space-time at the moment of observation), therefore the organization lost by stars can be transmitted from them by the field of time density instantly over any distance. The effect of this transmission must decrease inversely proportional to the square of the distance between the points of departure (a star) and arrival (a detector), i.e., inversely proportional to the area of a sphere as it should be in a space of three dimensions.

As a result, Kozyrev expected that the field of time den-

*In these papers, Prof. Kozyrev, who usually did not have co-authors in publications, had added the name of his laboratory engineer Victor V. Nassonov (1931–1986) in recognition of his many years of assistance.

†This is similar to how, in the space-time of General Relativity, the intervals of physically observable time are shortened (compared to the intervals of time in unperturbed space) depending on the potential of the gravitational field that fills the space and on the speed of rotation of the space itself.

sity created by any star can instantly initiate microprocesses of creation (organization) in a physical detector placed at the focus of a reflector telescope.*

This idea was confirmed by the astronomical observations performed by him in 1977–1979 (with the assistance of his laboratory engineer Nassonov) on the 50-inch reflecting telescope of the Crimean Astronomical Observatory [9, 10].

As a detector, Kozyrev used a metal-film resistor built into a Wheatstone bridge (and later — a thermocouple) installed in the focal plane of the telescope directly behind the narrow slit usually intended for a spectrograph, parallel to the slit. The slit was sawn in a 1-cm thick aluminum plate. Its width was 0.25 mm = 2″ in the sky. To increase the angular resolution of the observations, the slit (and detector) were oriented perpendicular to the daily motion of the celestial sphere. The detector and the entire measuring system were reliably isolated by a 1-cm thick aluminum case from external temperature influences, as well as from the influences of various processes in the telescope tower and beyond, so that random fluctuations from external influences registered by the detector were rare and did not affect the planned astronomical observations. The light from the observed astronomical objects was reliably shielded by a shutter made of black dense cardboard used in the packs of photographic plates, installed together with a thin glass plate in front of the slit (the thin glass plate covered the slit to prevent air circulation from the telescope into the measuring system).

Once the telescope was pointed at a point in the sky in front of a star, close to its visible position, Kozyrev slowed down the telescope's guiding mechanism slightly, causing the slit (and detector) installed in the focal plane of the telescope to slowly "scan" the sky in front of the visible star toward it along the right ascension.

Kozyrev proposed this method of observation, because his target was the true position of the visible stars at the moment of observation, which could be registered by the detector only in the case of instant transmission of signals through the field of time density. Whereas the visible position of a star in the sky is in the past, at the moment of time when the star emitted the light signal that we see in the form of its visible image. In other words, the visible position of a star "lags" relative to its true position in the sky, which is ahead of it, by the angular distance travelled by the star in the sky (due to its own motion relative to other stars) until the light emitted by the star reached an observer on the Earth and thereby created the visible image of the star.

The true position of a star can be calculated relative to its visible position, knowing the tangential velocity of the star relative to the Solar System (and the Earth) and the distance to the star, calculated based on its trigonometric parallax†. These data, obtained through astrometric observations over the past two centuries, can be found in astronomical catalogues and yearbooks.

The first series of astronomical observations according to the mentioned "scanning" method was performed by Kozyrev and Nassonov in October 1977. They immediately found that the detector responded reliably to the true position of the observed stars. The results were published in the paper [9].

In addition, the detector also responded to the visible position of the stars (where they are visible in the sky), despite the fact that it was reliably shielded from their light (see above). The difference in angular distance between the true and visible positions of the stars measured using the detector $\Delta\alpha_{\text{ob}}$ and $\Delta\alpha_{\text{c}}$ calculated from astronomical catalogues (both along the right ascension α) was in the range of 1″ to 4″, which is comparable to the slit in front of the detector (it selected 2″ on the celestial sphere, see above).

Table 1 shows the results of these astronomical observations. In Table 1, in addition to $\Delta\alpha_{\text{ob}}$ and $\Delta\alpha_{\text{c}}$ explained above, $\Delta\alpha_{\odot}$ is the angular distance between the true and visible positions of the stars, corrected for the value A_α of their annual aberration‡ along the right ascension

$$\Delta\alpha_{\odot} = \Delta\alpha - A_\alpha\,,$$

and the parallax π of each star is calculated based on its own annual angular displacement μ_α with respect to other stars and the celestial coordinates along the right ascension

$$\pi = 3.26\,\frac{\mu_\alpha}{\Delta\alpha_{\odot}}\,.$$

Besides the stars, they observed Jupiter, Mars, and Venus. Jupiter showed no effect on the detector. Mars showed the same effect as Venus (see Table 1).

An anomaly was the star ι Per, for which the observations yielded an abnormally large value of $\Delta\alpha_{\text{ob}} - \Delta\alpha_{\text{c}} = +28''$ that most likely corresponded to another faint object located near this star.

The value of $\Delta\alpha_{\odot} = \Delta\alpha - A$ and the parallax π calculated from the measured distances $\Delta\alpha_{\text{ob}}$ for three stars having small unknown parallaxes are given in square brackets.

It is interesting that the detector responded to both the true and visible positions of the stars even when the telescope's main mirror was covered by a shutter that reliably screened the light. In this case, the magnitude of the registered effect was weakened to the same extent for both the true and visible positions of the stars. "Consequently, the influence of the visible image [in this experiment] is not related to the light, but only coincides with its direction" — Kozyrev wrote [9].

*Since the glass of lenses, like any amorphous material, should absorb this effect, a refractor telescope is not applicable for this task.

†This is the very small angle at which the radius of the Earth's orbit is seen from the star. If you measure the position of a star relative to other stars in the sky several times during one year, when the Earth is at different points in its orbit around the Sun, the star will appear slightly offset relative to the other stars. Half of this apparent angular displacement of the star over the course of a year is called its trigonometric parallax.

‡Annual stellar aberration A is the observed displacement of stars from their actual positions on the celestial sphere, caused by the Earth's motion along its orbit around the Sun.

Star	Stellar magnitude	Spectral class	π	μ_α	$\Delta\alpha_\odot$	A_α	$\Delta\alpha_c$	$\Delta\alpha_{ob}$	$\Delta\alpha_{ob}-\Delta\alpha_c$	Reg. magnitude (in scale divisions)		Date of observation
										vis. pos.	true pos.	
ε And	4.52	G_5	0″.031 ± 5	−0″.232	−24″ ± 4	−17″	−41″ ± 4	−38″ −43″	+3″ −2″	5 2	6 4	21 October 1977 22 October 1977
η Cas	3.64	F_8	0″.182 ± 5	+1″.101	+19″ ± 0	−18″	+1″ ± 0	0	−1″	6	6	21 October 1977
o Cet	2.0–10.1	M_{5e}	0″.013 ± 5	−0″.009	−4″ ± 0	−19″	−23″ ± 0	−26″ −21″ −27″	−3″ +2″ −4″	0.2 0.8 0.0	1.3 1.2 10	23 October 1977 23 October 1977 20 October 1977
ρ Per	3.3–4.1	M_3	0″.008 ± 16 [0″.0040]	+0″.132	[102″]	−16″ −16″ −17″		+80″ +85″ +88″		0.0	1.2	12 October 1977 13 October 1977 21 October 1977
ι Per	4.17	G_0	0″.084 ± 15	+1″.266	+48″ ± 2	−17″	+31″ ± 2	+59″ +59″	+28″? +28″?	10.0 1.1	13.2 1.8	22 October 1977 23 October 1977
α Tau	1.1	K_5	0″.048 ± 4	+0″.069	+5″ ± 0	−12″	−7″ ± 0	−5″	+2″	—	15 30	13 October 1977 8 October 1977
o^2 Eri	4.5	K_0	0.200	−2″.225	−35″	−13″	−48″ ± 0	−50″	−2″	—	5	13 October 1977
α CMa	−1.58	A_0	0″.375 ± 4	−0″.537	−5″	−2″	−7″ ± 0	−5″	+2″	—	20	12 October 1977
α Ori	0.0–1.2	M_0	0″.005 ± 4 [0″.0067]	+0″.027	[+12″]	−12″		0″		1.5	1.5	27 October 1977
ξ Gem	3.4	F_5	0″.051 ± 6	−0″.111	−7″ ± 1	−9″	−16″ ± 1	−19″	−3″	0.8	2.2	27 October 1977
β Gem	1.21	K_0	0″.093 ± 5	−0″.623	−21″ ± 1	+4″	−17″ ± 1	−20″	−3″	3	3	19 October 1977
α CMi	0.48	F_5	0″.288 ± 5	−0″.707	−8″ ± 0	−4″	−12″ ± 0	−12″	0″	1.3	5.5	27 October 1977
Venus						—	+36″	+37″ +38″	+1″ +2″	8 8	5 8	18 October 1977 22 October 1977
α Lyr	0.14	A_0	0″.123	+0″.200	+5″ ± 0	−2″	+3″ ± 0	+5″	+2″	4.8	6	20 October 1977
θ Peg	3.70	A_2	0″.042 ± 5	+0″.0272	+21″ ± 2	−9″	+12″ ± 2	+14″	+2″	0.0	0.7	22 October 1977
ξ^2 Aqr	4.42	F_2	0″.013 ± 5	+0″.204	+50″ ± 13	−11″	+39″ ± 13	+40″ +43″	+1″ +4″	0.3	0.6 0.7	23 October 1977 23 October 1977
β Peg	2.1–3.0	M_0	0″.015 ± 5	+0″.188	+39″ ± 13	−14″	+25″ ± 13	+26″	+1″	0.0	0.0	20 October 1977
ψ Peg	4.75	M_0	0″.003 ± 5 [0″.0042]	−0″.039	[−27″]	−16″		−43″		0.3	0.5	23 October 1977

Table 1: Results of the first series of Kozyrev's astronomical observations, in which he registered the instant transmission of signals from stars. October, 1977. Quoted from the original publication [9].

Star	Stellar magnitude	Spectral class	π	μ_α	$\Delta\alpha_\odot$	Date of observation
β Tri	3.08	A_5	0″.012	+0″.150	+39″	12 October 1977
λ Tau	3.8 – 4.1	B_3	−0″.009	−0″.006	?	23 October 1977
α Tau	1.1	K_5	0″.048	+0″.069	+5	22 and 23 October 1977
γ Psc	3.85	K_0	0″.025	+0″.756	+95	22 October 1977
ω Psc	4.03	F_5	0″.012	+0″.147	+15	22 October 1977

Table 2: Four stars that had no effect on the detector, and also the star α Tauri, whose effect was found to be variable. October, 1977. Quoted from the original publication [9].

Four of the observed stars had no effect on the detector, most likely due to the low sensitivity of the signal registering system used in the observations. They are listed in Table 2.

In addition, Kozyrev concluded that the star α Tau most likely emits a variable time density. This explained the fact that, as is seen from Table 1 and Table 2, this star produced a very strong effect on October 8, then its influence on the detector halved on October 13, and there was no influence on October 22 and 23.

In the second series of the astronomical observations, Kozyrev and Nassonov increased the sensitivity of the signal registering system by almost one order of magnitude, and also extended the area of the sky subject to "scanning" near each observed star. The latter was due to the fact that, as Kozyrev reasoned, since the detector responded to the signals transmitted instantly through the field of time density from the true position of the star (where it is at the present moment of time) and from its visible position in the past (along the trajectory of the light coming from it), then the field of time density should also instantly transmit the signals coming from the star and along the "reverse trajectory of light", along which the position of the Earth at the present moment of time is visible from the star located in the future.

In other words, the detector must respond to the signals transmitted instantly through the field of time density from three points in the sky associated with each observed star:

1. The visible (past) position of the star, where it was in the past when it emitted the light signal that we see at present as its visible image in the sky;
2. The true position of the star, where it actually is at the present moment of time;
3. The position of the star in the future, symmetric to its visible position in the past with respect to its true position in the sky.

The signals coming instantly through the field of time density from the first position of a star (its visible position in the past) indicate that the star not only exists at the present moment of time, but in fact continues to exist as a real object in the past. Whereas the third position of the star (in the future) makes it possible to instantly observe the future of the star as an already existing reality.

This second series of the astronomical observations was performed during the spring and autumn of 1978, and also in May 1979, using the same 50-inch reflecting telescope. The results were published in the paper [10]. They are shown here in Table 3, where $\Delta_1\alpha_{ob}$ means the observed angular distance between the true position of the star (where it is at the present moment of time) and its visible position (in the past), while $\Delta_2\alpha_{ob}$ is the observed distance between the symmetrical position of the star in the future and its visible position (theoretically, it should be $\Delta_2\alpha_{ob} = 2\Delta_1\alpha_{ob}$).

The detector responded to all three mentioned positions of each observed star (except only ι Persei).

As previously in 1977, in the first series of the observations, ι Persei showed an anomaly: the detector did not respond to its true position (in the middle between its positions in the past and in the future), but reliably detected its position in the future $\Delta_2\alpha_{ob} = +59''$. Most likely this star has variable activity and was weakened during the season of these observations.

Since the values of the stellar aberration A differ in spring and autumn (due to the Earth moving in different directions in its orbit), the values of A for α Lyrae differ greatly in spring and autumn (A even changes its sign). This also led to a corresponding change in the sign of the measured values of $\Delta_1\alpha_{ob}$ and $\Delta_2\alpha_{ob}$, in full agreement with the theory.

In addition to the stars, the aforementioned "scanning" method of astronomical observations was also used to observe extended astronomical objects: the globular cluster M2 in Aquarius, the globular cluster M13 in Hercules, and the galaxy M31 (Andromeda Nebula). Since these are not point-like objects (unlike stars) and they are not uniform, then scanning each one creates three non-uniform profiles of it, corresponding to its past, present and future, which are superimposed on each other. As a result, in the scan of each of the extended astronomical objects, the hills of maximum influence on the detector were split into three peaks corresponding to the past, present and future. These scanned profiles, which were non-uniform in structure, also showed a decrease in the

Star	Stellar magnitude	Spectral class	π	μ_α	$\Delta\alpha_\odot$	A_α	$\Delta\alpha_c$	$\Delta_1\alpha_{ob}$	$\Delta_2\alpha_{ob}$	Date of observation
10 UMa	4.1	F_5	$0''.071 \pm 5$	$-0''.436$	$-20''$	$-9''$	$-29'' \pm 1$	$-28''$	$-57''$	13 April 1978
α Leo	1.3	B_8	$0''.039 \pm 7$	$-0''.248$	$-20''$	$-12''$ $-4''$	$-32'' \pm 4$ $-24'' \pm 4$	$-35''$ $-26''$	$-70''$ $-50''$	7 April 1978 8 May 1979
γ Boo	3.0	F_0	$0''.016 \pm 7$	$-0''.115$	$-23''$	$-20''$	$-43'' \pm 7$	$-50''$	$-97''$	24 April 1978
ε Boo	2.7	K_0	$0''.013 \pm 7$	$-0''.049$	$-12''$	$-20''$	$-32'' \pm 6$	$-35''$	$-67''$	13 May 1979
α Lyr	0.14	A_0	$0''.123 \pm 5$	$+0''.200$	$+5''$	$-2''$ $-18''$	$+3'' \pm 0$ $-13'' \pm 0$	$+5''$ $-12''$	 $-23''$	20 October 1977 14 May 1979
ι Per	4.2	G_0	$0''.084 \pm 5$	$+1''.266$	$+48''$	$-17''$	$+31'' \pm 2$	no	$+59''$	22–23 October 1977
τ Per	4.1	G_8, A_5	$0''.012 \pm 5$	$0''.000$	0	$-20''$	$+20'' \pm 0$	$-27''$	$-46''$	3 November 1978
ξ^2 Aqr	4.4	F_2	$0''.013 \pm 5$	$+0''.204$	$+50''$	$-11''$	$+39'' \pm 13$	$+42''$ $+38''$	 $+80''$	23 October 1977 29 October 1978
β Peg	2.1 – 3.0	M_0	$0''.015 \pm 5$	$+0''.188$	$+39''$	$-14''$	$+25'' \pm 13$	$+26''$ $+35''$	 $+60''$	20 October 1977 29 October 1978

Table 3: Results of the second series of Kozyrev's astronomical observations. The detector responded to three positions of each observed star (except ι Persei): its position in the past (visible position), in the present (its true position), and in the future symmetrical to its visible position in the past. Spring and autumn 1978, and also May 1979. The values of $\Delta_1\alpha_{ob}$ measured in the first series of the astronomical observations (October 1977, see Table 1) are given as a reference. Quoted from the original publication [10].

Star	π	μ_α	$\Delta\alpha_\odot$	A_α	$\Delta\alpha_c$	$\Delta\alpha_{ob}$
β Peg	$0''.015 \pm 5$	$0''.217$	$47''.16$	$+33''.52$	$+13''.6$	$+12''.6 \pm 1''.3$
β And	$0''.043 \pm 5$	$0''.220$	$16''.72$	$+41''.58$	$-24''.9$	$-25''.4 \pm 1''.7$
δ And	$0''.024 \pm 6$	$0''.162$	$22''.00$	$+39''.51$	$-17''.5$	$-20''.2 \pm 2''.5$

Table 4: Results of the testing astronomical observations conducted by Eganova and Lavrent'ev. 13 October 1989. Quoted from the original publication [11].

magnitude of the effect near the centre of each extended astronomical object: Kozyrev explained this by the supposition that where the stellar density is very high, there is a strong absorption of the field of time density [10].

It should be noted that although we unfortunately were not personally acquainted with Prof. Kozyrev (we read these publications already after his death), one of the authors of this paper, Dmitri Rabounski, visited Victor Nassonov twice at his apartment in St. Petersburg in 1985 shortly before his sudden death (at that time, Nassonov headed a laboratory at an industrial company). Nassonov demonstrated the recordings of an automatic recorder used in the last series of the astronomical observations (instead of the pointer galvanometer used at the initial stage). The recorded tapes clearly indicated three peaks of the signals, recorded for each of the observed stars and corresponding to its successive positions in the past, present and future on the celestial sphere.

It is no wonder that other scientists also took notice of these astronomical observations. In 1989, Irène A. Eganova and Michael M. Lavrent'ev, Director of the Sobolev Institute of Mathematics (Novosibirsk) and a Fellow of the USSR Academy of Sciences, decided to reproduce Kozyrev's astronomical observations. Their collaborators at the Institute in Novosibirsk reproduced Kozyrev's experimental setup, then Eganova and Lavrent'ev, together with their research group, performed testing astronomical observations according to Kozyrev's method on the same 50-inch reflecting telescope of the Crimean Astronomical Observatory. To be more confident in the result, they scanned the area of the sky near each observed star not only in one direction (as Kozyrev did), but also in two directions (there and back). Excerpts from their testing observations of the stars β Pegasi, β Andromedae and δ Andromedae are shown in Table 4, quoted from their first short report [11].

In their second short report [12], Eganova and Lavrent'ev reported the registration of signals coming from the true position of the Sun preceding the visible one by $2°4'.6$ (four visible diameters of the Sun) — the angular distance travelled by the Sun in 8.3 minutes, during which the light emitted by it reaches the Earth. The detector was installed in the focal

plane of a small 4-inch reflecting telescope, the main mirror of which was reliably shielded from the light coming from the Sun, and the signal registering system was protected from solar thermal effects. The detector in one series of the observations was a metal-film resistor built into a Wheatstone bridge as before. According to the records of scanning the near-solar space, the resistor responded to both the true and visible positions of the Sun, as when observing the stars. In the second series, it was a container with Escherichia coli bacteria in the state of anabiosis, which they exposed to the true position of the Sun for 3 minutes, while a control container with bacteria of the same brood remained in the laboratory. It was found that after exposure to the true position of the Sun, the number of viable cells increased by 1.2–3 times (depending on the specific brood).

"Not a single fact was found that contradicted Kozyrev's observations, however, further research is required to confirm his conclusions regarding the properties of the observed effect" — they concluded [11].*

Indeed, one cannot but agree with this conclusion. Yes, the effect discovered by Prof. Kozyrev was weak and his astronomical observations were difficult to reproduce. On the other hand, this was not a single unique experiment. The discovered effect was registered on many stars over several years and was confirmed by astronomical observations of an independent group of scientists.

We must therefore carefully search for a theoretical basis that could explain the instant transmission of signals in the framework of modern theoretical physics. A theory of this effect could determine the key physical factors of this process, and, accordingly, determine methods for enhancing these factors in order to create a new industrial technology of communication and transport.

This was one of the reasons why we started our own theoretical research on this topic in the mid-1980s and why we are now writing this article.

2 Theoretical explanation

In fact, Kozyrev's astronomical observations showed that signals from each star in the real space-time are instantly transmitted to the observer from its three positions in the sky: its visible position in the past (along the trajectory of light), its true position at the moment of observation and its position in the future (along the "reverse trajectory of light").

Kozyrev originally believed [13] that the results of his astronomical observations could be interpreted in the framework of the four-dimensional Minkowski space (which is the space-time of Special Relativity). He proceeded from the fact that the four-dimensional metric (four-dimensional distance between two adjacent points) in the Minkowski space is expressed in the form

$$ds^2 = c^2dt^2 - dx^2 - dy^2 - dz^2 = c^2dt^2\left(1 - \frac{\mathrm{v}^2}{c^2}\right),$$

where v is the velocity of a signal in the three-dimensional space. Kozyrev argued that the four-dimensional distance in the Minkowski space, say, between a star and an observer, is zero $ds = 0$ along three world lines. The line $dt = 0$, coinciding with the three-dimensional space of the observer, indicates the true position of the star, where we would see it if light travelled instantly. The line $\mathrm{v} = +c$ indicates the position of the star in the past, when it emitted the light signal that we see as its image in the sky. The line $\mathrm{v} = -c$ indicates the position of the star in the future, symmetrical to its visible position in the past (with respect to its true position), when the light signal emitted from the Earth reaches it.

However, this statement by Kozyrev does not correspond to the geometry of the Minkowski space (Kozyrev was an outstanding astronomer of the 20th century, but was not familiar with Riemannian geometry). Below we show why and how the instant transmission of signals is explained in the space-time of General Relativity.

Definition: *Instant transmission of a signal* means that the interval of physically observable time, registered by the observer between the sending of the signal and its arrival, is zero. In other words, the physically observable time of an instantly transmitted signal, registered by the observer, stops.

Physically observable quantities in the four-dimensional pseudo-Riemannian space (the space-time of General Relativity, a particular case of which is the Minkowski space) are defined as the projections of four-dimensional generally covariant quantities onto the three-dimensional spatial section and the time line associated with an observer. Such physically observable projections are invariant throughout the observer's spatial section (his observable three-dimensional space), depend on its geometric and physical properties, and are, therefore, called *chronometric invariants* [14–17].

Thus, the interval of physically observable time $d\tau$ registered by an observer is the projection of the four-dimensional displacement vector x^α ($\alpha = 0, 1, 2, 3$) onto his time line

$$d\tau = \sqrt{g_{00}}\, dt - \frac{1}{c^2}\, v_i dx^i,$$

where dt is the interval of coordinate time, which would be counted by the observer in the absence of disturbing factors, the time (zero) component g_{00} of the fundamental metric tensor $g_{\alpha\beta}$ is expressed with the potential w of the gravitational field that fills the space of the observer

$$\sqrt{g_{00}} = 1 - \frac{\mathrm{w}}{c^2}, \qquad \mathrm{w} = c^2\left(1 - \sqrt{g_{00}}\right),$$

*Their reports [11, 12] were published in the short communications from the USSR Academy of Sciences, known as *Doklady Akademii Nauk SSSR*, which is a highly influential and prestigious scientific journal, intended only for the Academy Fellows (or for the communications personally recommended by them) and published in English since 1956.

and v_i is the three-dimensional vector of the linear velocity of rotation of the observer's space

$$v_i = -\frac{c\,g_{0i}}{\sqrt{g_{00}}}\,, \qquad v^i = -\,c\,g^{0i}\sqrt{g_{00}}\,,$$

which is caused by $g_{0i} \neq 0$ (meaning that the observer's spatial section is non-orthogonal to his time line) and therefore it cannot be eliminated by coordinate transformations along the spatial section of the observer.

The physically observable three-dimensional interval $d\sigma$ is determined as

$$d\sigma^2 = h_{ik}\,dx^i dx^k,$$

where

$$h_{ik} = -\,g_{ik} + \frac{1}{c^2}\,v_i\,v_k\,, \quad h^{ik} = -\,g^{ik}, \quad h^i_k = \delta^i_k$$

is the physically observable three-dimensional metric tensor, which is the projection of the fundamental metric tensor $g_{\alpha\beta}$ onto the spatial section of the observer and possesses all its properties throughout his spatial section (three-dimensional observable space). Thus, the square of the four-dimensional (space-time) interval $ds^2 = g_{\alpha\beta}\,dx^\alpha dx^\beta$ expressed in terms of physically observable quantities has the form

$$ds^2 = c^2 d\tau^2 - d\sigma^2.$$

In the Minkowski space, as is seen from the Minkowski metric that above, $g_{00} = 1$ that means the absence of gravitational fields (the gravitational potential is $\mathrm{w} = 0$), and also $g_{0i} = 0$ meaning that the three-dimensional space (spatial section) is everywhere orthogonal to the time lines piercing it, and, hence, it does not rotate ($v_i = 0$). Therefore, the interval of physically observable time $d\tau$, which is registered by an observer in the Minkowski space, is always

$$d\tau = dt\,.$$

This fact, in particular, means that in the Minkowski space (the space-time of Special Relativity) there are *no geometric or physical disturbing factors* that could cause stopping physically observable time. In such a space, the concept of stopping time is essentially absent: according to the geometry of the Minkowski space, the physically observable time coordinate registered by the observer is $dx^0 = c\,d\tau = c\,dt$, i.e., it changes absolutely uniformly throughout the space along the directrices of the light cone of the observer at a speed equal to $\pm c$ (the plus sign takes place when counting time into the future, and the minus sign — when counting time into the past). The physically observable time interval in the Minkowski space is zero $dx^0 = c\,dt = 0$ only at the space-time point, where the vertices of the light cones of his past and future converge (i.e., only at the point of his observation), but not along any three-dimensional path between him and another object in space (say, a star). Consequently:

> Since stopping physically observable time in the Minkowski space is in principle impossible due to the fact that its geometric structure does not contain disturbing factors that could stop time, the geometric structure of the Minkowski space itself does not allow instant transmission of a signal.

On the other hand, despite the error in Kozyrev's theoretical explanation [13], the results of his astronomical observations indicate that instant transmission of signals from stars is an ordinary phenomenon in the real space-time.

Another case — the space-time of General Relativity, because it allows all conceivable disturbing factors characteristic of pseudo-Riemannian spaces due to their Riemannian geometry.

We considered the conditions for stopping physically observable time in the space-time of General Relativity in our works on the theory of non-quantum teleportation, which we began in the late 1980s and continue to this day. Everything that follows is based on the theoretical background, published in 2001 in our research monograph [18], and then — in our subsequent papers [19–21].

Derive the *physical conditions that stop observable time*. From the definition of the interval of physically observable time $d\tau$ in the space-time of General Relativity (see above), we obtain that the physically observable time stops for an observed object ($d\tau = 0$) under the physical conditions

$$\mathrm{w} + v_i\,u^i = c^2,$$

determining the necessary combination of the potential w of the gravitational field that fills the space, the linear velocity v_i with which the space rotates, and also the coordinate velocity $u^i = \frac{dx^i}{dt}$ of the object with respect to the observer.

These physical conditions at first glance seem exotic for a regular laboratory: an extremely strong gravitational potential and speeds close to the speed of light. However, these conditions that stop observable time are realized inside every physical body in the range from elementary particles to planets and stars. And we will now show why.

Since every physical body possesses mass, its gravitational field has a breaking at a distance from its barycentre, which is equal to its gravitational radius $r_g = 2GM/c^2$ calculated for its mass M. For instance, at $r = r_g$ from the barycentre, the zero (time) component g_{00} of the fundamental metric tensor of the Schwarzschild mass-point metric

$$ds^2 = \left(1 - \frac{r_g}{r}\right)c^2 dt^2 - \frac{dr^2}{1 - \frac{r_g}{r}} - r^2\left(d\theta^2 + \sin^2\theta\,d\varphi^2\right),$$

which describes the space of a massive spherical body approximated by a material point, is zero

$$g_{00} = 1 - \frac{r_g}{r} = 0\,.$$

Therefore, the potential of the gravitational field of every physical body on a spherical surface of the radius r_g around its barycentre is

$$\mathrm{w} = c^2\,(1 - \sqrt{g_{00}}) = c^2,$$

which is the same in the space of a rotating massive spherical body, because the component g_{00} has the same formula for these two spaces. You can see this from the space metric of a massive spherical body that rotates along its equatorial coordinate axis φ with a constant angular velocity $\omega = const$, which was introduced and proved in [22]

$$ds^2 = \left(1 - \frac{r_g}{r}\right) c^2 dt^2 - 2\,\omega r^2 \sin^2\theta \sqrt{1 - \frac{r_g}{r}}\, dt\, d\varphi - \\ - \frac{dr^2}{1 - \frac{r_g}{r}} - r^2\left(d\theta^2 + \sin^2\theta\, d\varphi^2\right).$$

Such a tiny spherical surface, we concluded in our previous paper [23], exists around the barycentre deep inside absolutely every physical body simply because physical bodies possess mass.

The condition $\mathrm{w} = c^2$ means stopping physically observable time $d\tau = 0$, which is also the condition for instant transmission of signals, if the body does not rotate ($v_i = 0$). This means that the condition for instant transmission of signals ($d\tau = 0$) is satisfied on the spherical surface $r = r_g$ around the barycentre of every non-rotating body. For rotating bodies, $d\tau = 0$ is satisfied under $\mathrm{w} + v_i u^i = c^2$ (see above). Therefore, since $d\tau = 0$ in this case is satisfied at a lower value of the gravitational potential w due to the second term caused by the rotation of space, the condition for instant transmission of signals is satisfied inside every rotating body on a sphere enveloping its barycentre slightly above the radius r_g.

Thus, we arrive at the conclusion:

> According to General Relativity, the condition of instant transmission of signals is satisfied on a tiny spherical surface of the gravitational radius (for non-rotating bodies) or slightly above it (for rotating bodies), existing around the barycentre deep inside absolutely every physical body in the range from elementary particles to planets and stars.

The path along which signals can be instantly transmitted in the pseudo-Riemannian space is determined by the condition of instant signal transmission ($d\tau = 0$) and is described by the obvious equation

$$\tau = const,$$

which describes trajectories along the three-dimensional spatial section of the observer (his observable three-dimensional real physical space), which is generally non-uniform, curved, rotating and deformable. Along such trajectories, neither the four-dimensional (space-time) interval ds nor the physically observable three-dimensional interval $d\sigma$ between the points of departure and arrival of the instantly transmitted signal are not equal to zero

$$c^2 d\tau^2 = 0, \qquad ds^2 = c^2 d\tau^2 - d\sigma^2 = -d\sigma^2 \neq 0.$$

The resulting equation of trajectories for instant signal transmission, together with the previous conclusion about the location of the conditions for stopping observable time, lead us to the conclusion:

> The spherical surfaces, enveloping the barycentres of all physical bodies at their gravitational radius (for non-rotating bodies) and slightly above it (for rotating bodies), on which physically observable time stops, are all connected to each other by trajectories of stopping observable time. Signals, instantly transmitted along these trajectories, instantly connect all physical bodies in the Universe.
>
> Trajectories of this type instantly connect any observer with stars and indicate the middle (true) position of stars, which was registered in Kozyrev's astronomical observations.

Note that, as we have already mentioned above, this type of trajectories for signals do not take place in the Minkowski space of Special Relativity (where there is no disturbing factors that could cause stopping observable time). Such trajectories take place only in the space-time of General Relativity (since it allows all disturbing factors that are conceivable due to its Riemannian geometry).

Let us now find the trajectories that indicate the instant transmission of signals from the visible (past) position of stars and their position in the future (symmetrical to their visible position) in Kozyrev's astronomical observations. Presumably, these should be trajectories on the surface of the light cone: on its half (for signals coming to the observer from the visible position of the star in the past) and on the upper half (for signals coming from the symmetrical position of the star in the future). Therefore, we will first check this assumption by considering the light cone equation.

The light cone equation is the equation of trajectories lying on the surface of the light cone in the four-dimensional pseudo-Riemannian space (which is the space-time of General Relativity). It is determined according to the definition of the light cone by the condition

$$ds^2 = c^2 d\tau^2 - d\sigma^2 = 0, \qquad c^2 d\tau^2 = d\sigma^2 \neq 0,$$

which means that the four-dimensional intervals on its surface (i.e., along its directrices) are zero, while the intervals of physically observable time and the physically observable three-dimensional spatial intervals are equal to each other, but not equal to zero. Substituting the definitions of $d\tau$ and $d\sigma$ (see above) into the light cone condition $c^2 d\tau^2 = d\sigma^2$ and reducing similar terms, we obtain the light cone equation in the

pseudo-Riemannian space

$$g_{00}\,c^2dt^2 - 2\,\sqrt{g_{00}}\,v_i\,dx^i dt + g_{ik}\,dx^i dx^k = 0\,.$$

In the Minkowski space metric (see it in the very beginning), we have $g_{00} = 1$, $g_{0i} = 0$ (and, hence, $v_i = 0$), and also $g_{ik} = -1$. Substituting these values into the general formula of the light cone equation above, and since $dt \neq 0$ (as we have already explained, observable time cannot be stopped in the Minkowski space, because its geometric structure does not contain disturbing factors that could stop time), we obtain the light cone equation in the Minkowski space

$$\left(1 + \frac{1}{c^2}\,g_{ik}\,u^i u^k\right)dt^2 = 0\,, \qquad dt \neq 0\,,$$

where $u^i = \frac{dx^i}{dt}$ is the coordinate velocity of a signal. Because $g_{00} = 1$ and $v_i = 0$ in the Minkowski space, ($v_i = 0$), we have

$$d\tau = \sqrt{g_{00}}\,dt - \frac{1}{c^2}\,v_i\,dx^i = dt\,,$$

$$h_{ik} = -g_{ik} + \frac{1}{c^2}\,v_i\,v_k = -g_{ik}\,,$$

and, therefore, the square of the physically observable velocity of the signal $\mathrm{v}^i = \frac{dx^i}{d\tau}$ has the form $\mathrm{v}^2 = h_{ik}\,\mathrm{v}^i\mathrm{v}^k = -g_{ik}\,u^i u^k$. As a result, the light cone equation in the Minkowski space has the form

$$\left(1 - \frac{\mathrm{v}^2}{c^2}\right)dt^2 = 0\,, \qquad dt \neq 0\,,$$

which means

$$\mathrm{v}^i = \pm\,c^i\,, \qquad \mathrm{v}^2 = -g_{ik}\,c^i c^k = c^2 = inv,$$

where the plus sign refers to signals travelling into the future, and the minus sign — if signals travel into the past. Therefore, we conclude:

> Signals on the surface of the light cone in the Minkowski space (which is the space-time of Special Relativity) are not transmitted instantly. They travel with the same (constant) physically observable velocity equal to the velocity of light.

Let us turn back to the above general formula of the light cone equation in the pseudo-Riemannian space (which allows all disturbing factors that are conceivable due to its Riemannian geometry). It can be easily transformed using the definition of $d\tau$ to the form

$$\left(1 - \frac{\mathrm{v}^2}{c^2}\right)d\tau^2 = 0\,,$$

which differs from the above formula of the Minkowski space in the disturbing factors $g_{00} \neq 1$, $g_{0i} \neq 0$ (and, hence, $v_i \neq 0$) and $g_{ik} \neq -1$ that are characteristic of the pseudo-Riemannian space metric and manifested, in particular, in the physically observable time interval $d\tau$, the physically observable velocity of signals v^i and the physically observable metric tensor h_{ik} determining $\mathrm{v}^2 = h_{ik}\,\mathrm{v}^i\mathrm{v}^k$.

This condition is satisfied, since $d\tau \neq 0$ on the surface of the light cone*, only if the observable velocity of signals is

$$\mathrm{v}^i = \pm\,c^i\,,$$

$$\mathrm{v}^2 = h_{ik}\,c^i c^k = \left(-g_{ik} + \frac{1}{c^2}\,v_i\,v_k\right)c^i c^k = c^2 = inv,$$

where the plus sign means their travel into the future, and the minus sign — their travel into the past. This means:

> Signals are not transmitted instantly on the surface of the light cone in the pseudo-Riemannian space (which is the space-time of General Relativity), but travel with the velocity of light, the physically observable three-dimensional vector of which depends on the disturbing factors characteristic of the pseudo-Riemannian space, while its square remains invariant. Their trajectories coincide with the trajectories travelled by light signals in the Minkowski space in the absence of the disturbing factors, i.e., when the non-uniform, curved, rotating and deformable light cone of the pseudo-Riemannian space has became the straight and uniform light cone of the Minkowski space.

In other words,

> Neither the straight and uniform light cone in the Minkowski space of Special Relativity nor the disturbed light cone in the pseudo-Riemannian space of General Relativity are home of the instantly transmitted signals that indicated the visible and future positions of stars in Kozyrev's astronomical observations.

We therefore consider trajectories, along which a stronger condition is satisfied than the aforementioned light cone condition ($ds^2 = c^2d\tau^2 - d\sigma^2 = 0$, $c^2d\tau^2 = d\sigma^2 \neq 0$). This is the condition

$$ds^2 = c^2d\tau^2 - d\sigma^2 = 0\,, \qquad c^2d\tau^2 = d\sigma^2 = 0\,.$$

Since along such trajectories the four-dimensional interval ds, the physically observable time interval $d\tau$ and the physically observable three-dimensional spatial interval $d\sigma$ are zero, i.e., all these intervals degenerate along such trajectories, we called their home space a *fully degenerate space*, or in other words — a *zero-space* [18–21].

In particular, since trajectories in the zero-space associated with the pseudo-Riemannian space of General Relativity

*Except for a single space-time point, which is the location of the observer himself (at this point, the vertices of the light cones of his past and future converge). In this case, the point of signal emission and the location of the observer coincide and, therefore, the observable time interval between the emission of the signal and its arrival is always $d\tau = 0$.

is a fully degenerate (ultimate) version of trajectories on the surface of the light cone, the zero-space is in fact a *fully degenerate light cone*.

Since from the point of view of a regular observer $d\tau = 0$ is everywhere in the zero-space (which is a fully degenerate light cone), then the motion of signals along their trajectories in the zero-space is observed by him as an instant transmission of these signals in his observable (non-degenerate) space along trajectories on the surface of the regular light cone.

In confirmation of what has been said, we transform the light cone equation to a form that takes into account the physical conditions of full degeneration $\mathrm{w} + v_i u^i = c^2$, which are also the physical conditions that stop observable time ($d\tau = 0$, see above). The resulting form of the light cone equation

$$\left\{\left[1 - \frac{1}{c^2}\left(\mathrm{w} + v_i u^i\right)\right]^2 - \frac{u^2}{c^2}\right\} dt^2 = 0, \qquad dt \neq 0$$

is satisfied at every point on the surface of the light cone. Here $u^i = \frac{dx^i}{dt}$ is the signal's coordinate velocity (for which we have $u^2 = -g_{ik}\, u^i u^k$), and dt is the coordinate time interval (it never becomes zero, see explanation above). Under the conditions of full degeneration $\mathrm{w} + v_i u^i = c^2$, when observable time stops ($d\tau = 0$) from the point of view of an external observer, the above light cone equation transforms into the *degenerate light cone equation* that is also the *zero-space equation*

$$\left(1 - \frac{u^2}{c^2}\right) dt^2 = 0, \qquad dt \neq 0,$$

meaning that signals travel in the zero-space with the coordinate velocity of light, while they are observed as instantly transmitted signals by an external observer, whose home is the regular (non-degenerate) space-time.

In particular, the above means the following. Since the zero-space is a fully degenerate (ultimate) version of the light cone, signals can enter the zero-space and return back from there at any point on the surface of the light cone if the physical conditions for full degeneration are somehow realized at that point. For example:

> Let us say that at the point of emission of a signal towards an observer at the moment of its emission the physical conditions of full degeneration are somehow realized, and these conditions are also realized in the receiving device of the observer. Then the observer will register that the signal has disappeared at the emission point and was instantly received by his receiver, while the visible path along which the signal was instantly transmitted is the trajectory of light signals between him and the emission point (despite the fact that the signal itself was transmitted along a trajectory lying in the fully degenerate zero-space).
>
> Such trajectories, instantly connecting any observer with stars, indicate the visible (past) position of stars and their position in the future (symmetrical to their visible position), which was registered in Kozyrev's astronomical observations.

Thus, all three positions of stars, which were indicated by instantly transmitted signals in Kozyrev's astronomical observations, have been explained in the pseudo-Riemannian space (space-time) of General Relativity. In the Minkowski space, which is the space-time of Special Relativity, Kozyrev's results have no explanation, because the Minkowski space does not contain disturbing factors that could stop time or fully degenerate the entire space-time.

3 Conclusion

In this article we discussed the phenomenon of instant transmission of signals from stars (long-range action), discovered in the astronomical observations performed in 1977–1979 by Prof. N. A. Kozyrev [9,10], then — reproduced and confirmed in 1989 by a group of scientists, headed by I. A. Eganova and M. M. Lavrent'ev [11, 12]. We also gave our own theoretical explanation to Kozyrev's observed results in the framework of General Relativity.

We have shown that the geometric structure of the Minkowski space (which is the space-time of Special Relativity) does not contain disturbing factors that could stop time. And, since stopping physically observable time along the trajectory of a signal between the points of its emission and arrival is a necessary condition for its instant transmission, signals cannot be transmitted instantly in the space-time of Special Relativity.

On the other hand, we have shown that observable time can be stopped in the pseudo-Riemannian space (space-time) of General Relativity, since it allows all disturbing factors that are conceivable due to its Riemannian geometry. Such factors are the gravitational field potential or the rotation of space (due to the non-orthogonality of the three-dimensional spatial section to time lines), or both of these factors presented together.

We have shown that the condition of stopping physically observable time is satisfied on a tiny spherical surface of the gravitational radius (for non-rotating bodies) or slightly above it (for rotating bodies), existing around the barycentre deep inside absolutely every physical body in the range from elementary particles to planets and stars. These spherical surfaces, enveloping the barycentres of all physical bodies are all connected to each other by trajectories of stopping observable time. Signals, instantly transmitted along these trajectories, instantly connect all physically bodies in the Universe. Such trajectories instantly connect any observer with stars and indicate the *middle* (*true*) *position of stars*, which was registered in Kozyrev's astronomical observations.

We have also considered a fully degenerate (ultimate) version of trajectories on the surface of the light cone, along which physically observable time stops and, therefore, sig-

nals travel instantly. Such trajectories make up a fully degenerate light cone associated with the pseudo-Riemannian space, which we called the zero-space. The motion of signals along such trajectories (i.e., in the zero-space) is observed by a regular external observer as their instant transmission in his observable (non-degenerate) space along trajectories of light. Once the conditions of full degeneration are somehow realized at the point of emission of a signal towards an observer and these conditions are also realized in his receiving device (receiver), then he will register that the signal has travelled instantly from the emission point to him along the trajectory of light signals (while it travelled along a trajectory lying in the fully degenerate zero-space). Such fully degenerate trajectories also instantly connect any observer with stars. They indicate the *visible* (*past*) *position of stars* and *their position in the future* (symmetrical to their visible position), registered in Kozyrev's astronomical observations.

This is how Kozyrev's astronomical observations of instant transmission of signals from stars are explained in the framework of General Relativity.

These results illustrate that, according to General Relativity, all physical bodies in the Universe, including you and us, exist not only at the present moment in time, but are multidimensional objects, the past, present and future of which are an existing reality.

Submitted on June 28, 2025

References

1. Kozyrev N. A. Observation of a volcanic process on the Moon. *Sky and Telescope*, 1959, v. 18, no. 4, 184–186; *Ibid.* Letter to the Editor. 1959, v. 18, no. 10, 561.
2. Kozyrev N. A. The atmosphere of Mercury. *Sky and Telescope*, 1964, v. 27, no. 6, 339–341.
3. Kozyrev, Nikolay Aleksandrovich. *Encyclopaedia Britannica*.
4. Dadaev A. N. Nikolai A. Kozyrev (1908–1983) — discoverer of Lunar volcanism (on the 100th anniversary of his birth). *Progress in Physics*, 2009, v. 5, no. 3, L3–L14.
5. Kozyrev N. A. Causal or Asymmetrical Mechanics in the Linear Approximation. Pulkovo Astron. Observatory, Leningrad, 1958 (in Russian).
6. Kozyrev N. A. Possibility of experimental study of the properties of time. A presentation, Sept. 1967. The Arlington Archive (Joint Publications Research Service), no. 45238, Arlington VA, May 2, 1968.
   Reprinted in: *The Abraham Zelmanov Journal*, 2012, v. 5, 188–220.
7. Kozyrev N. A. On the possibility of experimental investigation of the properties of time. In: *Time in Science and Philosophy*: *Collection of Scientific Papers*. Academia, Prague, 1971, 111–132 (this is a slightly modified version of the previous paper).
8. Kozyrev N. A. Astronomical observations using the physical properties of time. In: *Flaring Stars*: *Proc. of the Symposium at the Byurakan Astron. Observatory* (Oct. 5–8, 1976), Armenian Acad. of Sciences Publ., Yerevan, 1977, 209–227 (in Russian).
   Reprinted in: Kozyrev N. A. Collected Papers. Leningrad Univ. Publ., Leningrad, 1991, 363–383 (in Russian).
9. Kozyrev N. A. and Nassonov V. V. A new method for determining trigonometric parallaxes based on measuring the difference between the true and visible positions of a star. In: *Problems of Universe Exploration*, v. 7, Moscow-Leningrad, 1978, 168–179 (in Russian).
   Reprinted in: *Time and Stars. Collection of Papers for the 100th Anniversary of N. A. Kozyrev*, St. Petersburg, 2008, 106–117 (in Russian).
10. Kozyrev N. A. and Nassonov V. V. On some properties of time discovered by astronomical observations. In: *Problems of Universe Exploration*, v. 9, Moscow-Leningrad, 1980, 76–84 (in Russian).
    Reprinted in: *Time and Stars. Collection of Papers for the 100th Anniversary of N. A. Kozyrev*, St. Petersburg, 2008, 122–131 (in Russian).
11. Lavrent'ev M. M., Eganova I. A., Lutset M. K., Fominykh S. F. On the remote action of stars on resistor. *Doklady Akademii Nauk SSSR*, 1990, v. 314, no. 2, 352–355.
12. Lavrent'ev M. M., Gusev V. A., Eganova I. A., Lutset M. K., Fominykh S. F. On the registration of the real position of the Sun. *Doklady Akademii Nauk SSSR*, 1990, v. 315, no. 2, 368–370.
13. Kozyrev N. A. Astronomical proof of the reality of Minkowski's four-dimensional geometry. In: *Problems of Universe Exploration*, v. 9, Moscow-Leningrad, 1980, 85–93 (in Russian).
    Reprinted in: *Time and Stars. Collection of Papers for the 100th Anniversary of N. A. Kozyrev*, St. Petersburg, 2008, 132–140 (in Russian).
14. Zelmanov A. L. Chronometric Invariants. Translated from the 1944 PhD thesis, American Research Press, Rehoboth, New Mexico, 2006.
15. Zelmanov A. L. Chronometric invariants and accompanying frames of reference in the General Theory of Relativity. *Soviet Physics Doklady*, 1956, v. 1, 227–230 (translated from *Doklady Academii Nauk USSR*, 1956, v. 107, issue 6, 815–818).
16. Zelmanov A. L. On the relativistic theory of an anisotropic inhomogeneous universe. *The Abraham Zelmanov Journal*, 2008, vol. 1, 33–63 (translated from the thesis of the *6th Soviet Conference on the Problems of Cosmogony*, USSR Academy of Sciences Publishers, Moscow, 1957, 144–174).
17. Rabounski D. and Borissova L. Physical observables in General Relativity and the Zelmanov chronometric invariants. *Progress in Physics*, 2023, v. 19, issue 1, 3–29.
18. Rabounski D. and Borissova L. Particles Here and Beyond the Mirror. The 4th revised edition, New Scientific Frontiers, London, 2023 (the 1st edition was issued in 2001).
    Rabounski D. et Larissa Borissova L. Particules de l'Univers et au delà du miroir. La 2ème édition révisée en langue française, New Scientific Frontiers, Londres, 2023 (French translation).
19. Rabounski D. and Borissova L. On the possibility of instant displacements in the space-time of General Relativity. *Progress in Physics*, 2005, v. 1, issue 1, 17–19.
20. Rabounski D. and Borissova L. Non-quantum teleportation in a rotating space with a strong electromagnetic field. *Progress in Physics*, 2022, v. 18, issue 1, 31–49.
21. Rabounski D. and Borissova L. On the condition of non-quantum teleportation on the surface of a spherical body. *Progress in Physics*, 2025, v. 21, issue 1, 80–85.
22. Rabounski D. Introducing the space metric of a rotating massive body and four new effects of General Relativity. *Progress in Physics*, 2024, v. 20, issue 2, 79–99.
23. Borissova L. and Rabounski D. Galileo's principle and the origin of gravitation according to General Relativity. *Progress in Physics*, 2024, v. 20, issue 1, 69–78.

Origin of Cylindrically Oriented Zonal Flows in the Jovian Planets as Dictated by Quantum Celestial Mechanics (QCM)

Franklin Potter
Sciencegems, 8642 Marvale Drive, Huntington Beach, CA, 92646, USA. E-mail: frank11hb@yahoo.com

The four Jovian planets in the Solar System have fluid bodies surrounding a solid core and each exhibit several complex zonal flows with their atmospheres moving faster than the planet rotation. Several research groups have proposed that these atmospheric east-west zonal jet flows that are aligned with the axis of rotation are cylindrically confined, as indicated by identifying gravity harmonics. I propose that the source of these co-axial concentric cylidrical flow zones is dictated by quantum celestial mechanics (QCM), which states that the equilibrium radius for each cylindrical band/zone within the planet occurs where the Newtonian gravitational attraction balances the repulsive QCM quantization of angular momentum per unit mass effect.

1 Introduction

The four Jovian planets in our Solar System are fluid bodies surrounding a solid core. Fluid bodies do not rotate as rigid bodies and, instead, exhibit complex zonal flows in the atmospheres. Observational evidence of the Jovian planets by spacecraft in the visible, the ultraviolet (UV), the infrared (IR), and with magnetic field sensing, reveals atmospheric east-west zonal jet flows in each hemisphere. For a review that includes detailed diagrams of these zonal flows in the atmosphere down to a few thousand kilometers for Jupiter and Saturn, see [1].

These bands/zones on Jupiter have been observed through optical devices since the 1600s, but only via using data collected by the Juno and Cassini orbiting spacecraft at Jupiter and Saturn have researchers significantly improved our description of this complex zonal flow behavior.

Detailed analyses identifying gravity harmonics by several research groups over the past decade and earlier have suggested that the Jupiter and Saturn flows are probably aligned with the axis of rotation and that cylindrical confinement is essential for each distinct observed dynamic flow behavior. Specifically, as one example, in Jupiter the 21° N jet provides evidence that the flows extend inward cylindrically and not much radially [2]. For the equivalent cylindrical flow behavior on Saturn, see [3].

For all four Jovian planets, the flows penetrate cylindrically downward, to a depth of about 3000 km in Jupiter, to about 9000 km in Saturn, and to about 1000 km in Uranus and in Neptune. More than one cylindrical flow region exists within each Jovian planet. As a very simplified suggestion of the geometry being considered, Fig. 1 shows how two possible co-axial concentric flow cylinders would penetrate throughout a planetary sphere.

As these cylindrical regions rotate faster than the planet rotation, there would be physical flow phenomena to be measured along the concentric circular regions where each cylinder pierces the surface. One should note that there would be overlap among the cylindrical regions at most depths because they each could have a radial thickness that increases with depth within the planet.

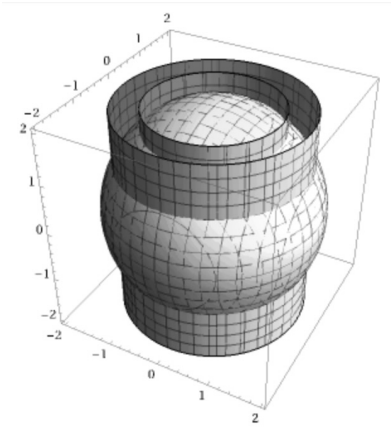

Fig. 1: Two co-axial concentric QCM cylinders penetrating the planet.

The actual physics origin of such cylindrical regions for the atmospheric flows within these Jovian planets has not been identified. Some complex suggestions involving dynamical combinations of Coriolis effects, temperature gradients, pressure gradients, magnetic field influences, etc., have been incorporated into existing models, but there has been no definitive single source proposed for the cylindrical symmetries [4, 5].

I propose that these co-axial concentric cylindrical flow zones can exist within all planets because they are dictated by the gravitational forces resulting from the quantization of angular momentum per unit mass constraint of quantum celestial mechanics (QCM) [6]. Equilibrium radii for the concentric cylinders within a massive body such as a planet are determined by both Newtonian gravitational attraction and a quantization of angular momentum per unit mass repulsive effect.

The equilibrium orbital radii of the planets of the So-

lar System as well as the orbital distances for planets in all known multi-planetary exosystems have been shown to obey this angular momentum constraint dictated by QCM in the Schwarzschild metric environment. Because each planet has a Schwarzschild radius r_s of a few meters or less, this quantiztion of angular momentum per unit mass effect applies also within the planets with the result being co-axial concentric cylindrical rotating regions.

2 Some prior applications of QCM

For an abbreviated derivation of quantum celestial mechanics (QCM) from the general relativistic Hamilton-Jacobi equation and some of its equations predicting gravitational effects for bodies obeying the Schwarzschild metric, see the Appendix. Applications of QCM in other gravitational metrics can be found in the original paper [6] and in several other of the references [7–11].

We have used QCM to explain the spacings of planetary orbits in the Solar System and in all known exoplanetary systems [8]. Essentially, QCM predicts both the Newtonian gravitational attraction and a repulsive effect [see (10) in the Appendix] that together specify equilibrium orbital radii that are a small subset of all possible Newtonian equilibrium orbital radii.

All known multi-planetary exosystems have been shown to obey this angular momentum constraint dictated by QCM. In the Solar System, we learned that the Oort Cloud, with its angular momentum contribution being almost 50 times greater than the angular momentum contributions of the planets plus the Sun, dictates the allowed equilibrium orbital radii of the planets to explain why its large radial separations are unique among the known planetary systems. Fig. 2 shows a sample of these exosystems obeying the angular momentum constraint. Note that they have planets closer to their star than the orbit radius of Mercury, and in some cases, they have a Jupiter mass planet close-in!

After applying the gravitational wave equation (GWE) in the Schwarzschild metric to planetary systems [8], we found further applications to galaxies, clusters of galaxies [9], and to the Universe. For the Universe [10], we determined an alternate viable explanation of cosmological redshifts in a static Universe in the interior metric, i.e. that a non-linear negative gravitational potential exists that agrees with the SN1a data for an accelerating behavior. Our result suggests that the clocks at the distant light sources tick slower than clocks at the observer for all observers.

For the analysis of the Jovian planets, we will use the same quantization of angular momentum per unit mass constraint dictated by QCM for the Schwarzschild metric given by (8) in the Appendix, which becomes

$$L/\mu = m\, L_T/M_T \tag{1}$$

for integer m and a gravitationally bound system total angular momentum L_T and total mass M_T.

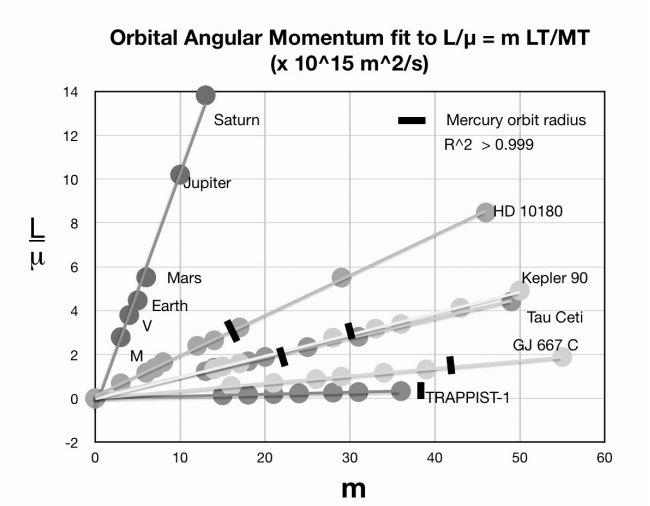

Fig. 2: The QCM angular momentum per unit mass constraint applied to several mulit-planetary exosystems. The short line marks the orbital radius distance of Mercury. The slopes are proportional to the total angular momentum in the gravitationally bound systems.

The application of this QCM orbital quantization equation is not only for planets in the exterior space surrounding the central massive object of mass M but also for the interior volume within the mass for all equilibrium radii r_{eq} greater than the Schwarzschild radius $r_s > 2GM/c^2$.

In 2021, we investigated radial distances from the Earth's axis within the Earth itself to establish [11] that the Antarctic Circumpolar Current (ACC), a significant water current moving eastward completely around the Antarctic Continent about 2 meters/second faster than the Earth's rotation at its latitude, exists at the $m = 6$ radial distance and is probably being driven by our QCM effect. That is, the ACC lies at the Earth's surface where a QCM rotational co-axial cylinder parallel to the Earth's axis penetrates the surface from the interior. Normally, one would expect a similar eastward water current around the North Pole region at about the same North latitude as the ACC, but land masses block such a continuous water current.

Recent seismic research [12] has revealed also that deep within the Earth, within its fluid outer core, lies a large donut-shaped mass, i.e. a toroidal volume, that rotates independently about the Earth's rotation axis at a different angular velocity than the rest of the outer core. Located at nearly the same radial distance from the Earth's axis as the ACC, we are investigating whether this rotating donut could be driven by the QCM gravitational force produced by the same cylinder with $m = 6$ as for the ACC.

3 Jovian planet considerations

In this investigation we are analyzing much more complicated dynamic systems involving planets with significant gaseous atmospheres. We consider whether the rotational zone/band structures of the Jovian planets, Jupiter, Saturn, Uranus, and

Neptune, are produced by the above QCM angular momentum constraint equations. Their Schwarzschild radii are all less than 3 meters, so they are expected to have rotational cylindrical regions co-axially parallel to the planet's rotation axis within their massive bodies.

However, unlike the Earth that is essentially dense solid and liquid matter all the way to its total radius, the Jovian planets each possess a fluid atmosphere that is a mixture of gases that extends significantly into the planet from the "surface", which is defined to be where the pressure is 1 bar. This atmospheric difference down to thousands of meters complicates any analysis.

Fortunately, the combined effects of Coriolis forces, temperature gradients, magnetic field movement, etc., have been worked out in terms of Bessel functions and Legendre funtions [1–3] for the geometry of the dynamic flows within the band structures. What is absent, however, is the reason for the existence of the proposed rotating co-axial concentric cylindrical regions within the rotating planets.

We will determine possible radii for the QCM co-axial concentric cylinders from the angular momentum constraint given by (1) based upon the physical parameters at each Jovian planet and try to determine whether they are the source of the cylndrical geometries for the atmospheric bands existing at the "surface". That is, if the radii of the predicted cylindrical regions roughly agree with the radii of the atmospheric zones/bands, we will consider that we have identified their source. In order to simplify our derivation of the cylindrical symmetry behavior within these planets, we will assume a north-south symmetry approximation for these band/zone regions, although there exists an obvious asymmetry in the flow data when the northern and southern hemispheres are compared.

Fig. 1 shows an example of only two co-axial concentric cylinders for a spherical planet. Where each cylinder intersects the "surface" is where the bands/zones should be. Because each cylinder has some width in the radial direction, the widths of each cylinder can overlap more than one other cylinder beneath the surface inside each planet, thereby creating a more complex environment than we will investigate. These complexities are probably already incorporated into the research models mentioned above.

4 Jovian planet analysis

If the planets were solid, their effective planet radii would be easy to define. However, a planet such as Jupiter has a solid core plus a liquid outer core region plus a significant lower density additional atmospheric region. One needs to determine the effective radius R of the planet for the application of the quantization of angular momentum per unit mass constraint in (1), which cannot be the radius R_0 to the "surface" because the atmosphere that occupies the outer radius is itself being driven by the QCM effective force determined by the dense inner regions.

Table 1: Effective planet radius for the Jovian planets.

Planet	α	αR^2 ($\times 10^{14}$m^2)	R ($\times 10^7$m)	Ratio R/R_0
Jupiter	0.2756	3.0	3.26	0.455
Saturn	0.22	4.0	4.26	0.71
Uranus	0.33	1.5	2.55	1.0
Neptune	0.33	1.4	2.46	1.0

Applying (1), we substitute vr for L/μ on the left side, with v being the tangential velocity of mass μ at orbit radius r, and substitute $\alpha MR^2\omega/M$ for L_T/M_T on the right side, to obtain the equilibrium radius expression

$$r_{eq}^2 = m\,\alpha R^2\,, \tag{2}$$

where α is the moment of inertia coefficient, i.e. of αMR^2, and R being the effective radius. For a solid planet, R would be the radial distance R_0 to its physical surface, but for the fluid Jovian planets, R may not be this distance.

We define an effective radius R to be the one that produces the correct latitudinal distribution of bands/zones at the surface of the planet. The effective αMR^2 values for the four Jovian planets are listed in Table 1. Note that for both Jupiter and Saturn, the effective radius R is much less than the actual radius R_0 of the planet as revealed in the ratio column, whereas for Uranus and Neptune the effective radius is probably the total radius of the planet. Also recall that for both Uranus and Neptune, the actual zonal latitudinal structures have not been identified as well as achieved for Jupiter and Saturn. Hopefully, more information will become available in the near future to ascertain whether our results actually agree with their band/zone structures.

The effective radius values in Table 1 are used to determine the r_{eq} values predicted by (1) and their equivalent latitudes for comparison to the data. The calculated values for the QCM co-axial concentric cylinders within the planets as listed in Table 2 for Jupiter and Saturn and in Table 3 for Uranus and Neptune.

The predicted latitudes for the zones/bands are in reasonable agreement with those at the surfaces of Jupiter and Saturn, but we await further data for the zone/band data for Uranus and Neptune.

Jupiter's differential rotation angular momentum plus the orbital angular momentum contributions from its moons produces $L_T = 4.795 \times 10^{38}\,\mathrm{kg\,m^2/s}$ with a mass of $M_T = 1.9 \times 10^{27}\,\mathrm{kg}$. For Saturn and its moons, $L_T = 7.109 \times 10^{37}\,\mathrm{kg\,m^2/s}$ for a mass $M_T = 5.683 \times 10^{26}\,\mathrm{kg}$. QCM predicts tangential velocities v_ϕ for each co-axial concentric cylindrical equilibrium radius r_{eq} based upon the equation

$$v_\phi = \frac{m\,L_T}{r_{eq}\,M_T}\,. \tag{3}$$

Table 2: Radial equilibrium distances for Jupiter and Saturn

m	Jupiter r_{eq} (10^7 m)	Lat θ	Saturn r_{eq} (10^7 m)	Lat θ
1	1.73	75.98	2.00	70.53
2	2.45	69.97	2.82	61.97
3	3.00	65.19	3.46	54.78
4	3.46	61.02	4.00	48.19
5	3.87	57.20	4.47	41.84
6	4.24	53.60	4.90	35.25
7	4.58	50.14	5.29	28.16
8	4.90	46.75	5.66	19.38
9	5.19	43.39	6.00	0
10	5.47	40.00		
11	5.74	36.60		
12	6.00	32.95		
13	6.24	29.22		
14	6.48	25.00		
15	6.71	20.20		
16	6.93	14.25		
17	7.14	0		

Table 3: Radial equilibrium distances for Uranus and Neptune.

m	Uranus r_{eq} (10^7 m)	Lat θ	Neptune r_{eq} (10^7 m)	Lat θ
1	1.23	58.64	1.18	61.46
2	1.73	47.40	1.54	51.43
3	2.12	33.96	1.89	40.08
4	2.45	16.56	2.18	28.04
5			2.43	10.33

Thus, for the Jupiter $m = 15$ and $m = 16$ zones/bands at the 20.20° and 14.25° latitude flow regions, QCM predicts tangential velocities v_ϕ of 5.65×10^4 m/s and 5.82×10^4 m/s, respectively. The zonal winds near the equitorial surface of Jupiter actually measure significantly lower values, having a maximum of about 100 m/s. Therefore, dynamic effects such as viscosity effects, etc., retard the flow in the atmosphere and are probably the cause of these much, much lower measured tangential velocity values than the predicted values.

For Saturn, for the $m = 7$ and $m = 8$ zones/bands at 28.16° and 19.38°, QCM predicts 1.66×10^4 m/s and 1.77×10^4 m/s tangential velocities, respectively. The data reveal much smaller flow velocities of about 300 m/s in these regions. Again, dynamic viscosity effects are probably reducing the predicted velocities to the measured velocities.

5 Conclusion

The zones/bands in the atmospheric flow regions on the surfaces of the Jovian planets appear to be in co-axial concentric cylinders. These complex atmospheric flows possibly penetrate into the planetary bodies to depths of thousands of kilometers. Although a dynamical combination of Coriolis effects, temperature gradients, pressure gradients, magnetic field influences, etc., have been incorporated into existing dynamic models by several research groups, there has been no definitive single source proposed for the apparent cylindrical symmetries defining these flow regions.

Quantum celestial mechanics (QCM) has a gravitational wave equation (GWE) that we previously had applied in the Schwarzschild metric to predict rotating co-axial concentric cylindrical regions within all massive bodies. For one example, we applied the GWE inside the Earth to determine that the Antarctic Cirumpolar Current (ACC), a water current traveling eastward about 2 meters/second faster than Earth's rotation rate at its latitude, could be explained by the application of the QCM quantization of angular momentum per unit mass equation

$$L/\mu = m\, L_T/M_T\,,$$

which relates an orbiting mass μ of angular momentum L in orbit in a gravitationally bound system to the total mass M_T and total angular momentum L_T. When applied to all known orbiting planets in multi-planetary systems, we established that their planet orbital radii agree with this quantization of angular momentum per unit mass constraint equation.

Upon applying this angular momentum constraint equation to the four Jovian planets, we identified co-axial concentric rotating cylinders for zones/bands at reasonable radii, i.e. rotating cylindrical regions piercing the surfaces at numerous latitudes roughly agreeing with observational data for the zone/band locations as determined with observations by telescopes and spacecraft.

Therfore, we suggest that the true source of the co-axial concentric cylindrical flow regions in the Jovian planets has been identified to be the result of the QCM combination of Newtonian gravitational attraction and the repulsive effect of QCM quantization of angular momentum per unit mass. An improved understanding of the complex dynamics of these flow regions can now be achieved in the near future.

Acknowledgements

The author appreciates the support of Sciencegems.com for the opportunity to investigate fundamental physics and its application to prevalent problems in Nature.

Received on June 25, 2025

A Appendix: brief derivation of QCM equations

In 2003, Howard G. Preston and I introduced [6, 7] Quantum Celestial Mechanics (QCM), which is derived from the general relativistic Hamilton-Jacobi equation and a simple transformation that maintains the equivalence principle. The result was a new gravitational scalar wave equation (GWE) that, in

the Schwarzschild metric, predicts the quantization of angular momentum per unit mass. Here is an abbreviated derivation of the equations to be used for analyzing the Jovian planets.

From the general relativistic Hamilton-Jacobi equation,

$$g^{\alpha\beta}\frac{\partial S}{\partial x^{\alpha}}\frac{\partial S}{\partial x^{\beta}} - \mu^2 c^2 = 0\,, \tag{4}$$

the transformation

$$\Psi = e^{iS'/\mu cH} \tag{5}$$

introduces a wave function Ψ, with S the action, μ the mass of the orbiting object, and $S' = S/\mu c$ so that the equivalence principle is obeyed. For a detailed derivation showing all the mathematical steps, see [6].

We defined a system scale length H by

$$H = \frac{L_T}{M_T c} \tag{6}$$

for the total gravitationally bound system mass M_T having total angular momentum L_T and c being the speed of light in vacuum.

Following through with the mathematical steps produced a scalar gravitational wave equation (GWE)

$$g^{\alpha\beta}\frac{\partial^2\Psi}{\partial x^{\alpha}\partial x^{\beta}} + \frac{\Psi}{H^2} = 0\,. \tag{7}$$

Expressing the GWE in the Schwarzschild metric, a separation of variables leads to differential equations in coordinates (t, r, θ, ϕ) that produce quantization conditions.

The angular parts dictate the quantization of angular momentum *per unit mass* for orbital angular momentum L as

$$\frac{L}{\mu} = mcH \tag{8}$$

for integer m. The radial equation leads to the quantization of energy *per unit mass* equation

$$E_n = -\mu c^2\frac{r_s^2}{8n^2H^2} \tag{9}$$

for integer n.

The expected value of the QCM orbital radial acceleration near the orbital equilibrium radius is defined by

$$\ddot{r}_{eq} = -\frac{GM}{r^2} + \frac{\ell(\ell+1)\,L_T^2}{r^3\,M_T^2}\,. \tag{10}$$

For cylindrical coordinates, the $\ell(\ell+1)$ is replaced by m^2.

For comparison, recall that the standard Newtonian gravitation has

$$\ddot{r}_{eq} = -\frac{GM}{r^2} + \frac{L^2}{\mu^2\,r^3} \tag{11}$$

and, because the angular momentum $L = \mu\sqrt{GMr}$ and the angular velocity $\dot{\phi} = L/\mu r^2$ for a circular orbit, then $\ddot{r} = 0$ and the radial acceleration per mass $(\ddot{r} - r\dot{\phi}^2)$ equals $-GM/r^2$.

Consequently, QCM has both the Newtonian attraction term and a repulsive angular momentum term around each equilibrium orbital radius, which results in the prediction of allowed orbital radii that are a sparse subset of the Newtonian ones. In addition, there will be equilibrium radii within planets at which a QCM acceleration occurs.

References

1. Fletcher L. N., Kaspi Y., Guillet T., Showman A. P. How well do we understand the belt/zone circulation of Giant Planet atmospheres? *Space Sci Rev*, 2020, v. B216, 30. arXiv:1907.01822v2.
2. Kaspi Y., Galanti E., *et al*. Observational evidence for cylindrically oriented zonal flows on Jupiter. *Nature Astronomy*, 2023, v. 7, 1463–1472.
3. Chachan Y. and Stevenson D. J. A Linear Approximation for the Effect of Cylindrical Differential Rotation on Gravitational Moments: Application to the Non-Unique Interpretation of Saturn's Gravity. *Icarus*, 2019, v. 323, 87–98. arXiv: 1902.10728v1.
4. Duer K., Galanti E., Kaspi Y. Gas Giant Simulations of Eddy-Driven Jets Accompanied by Deep Meridional Circulation. *AGU Advances*, 2023, v. 4, 32023AV000908. arXiv: astro-ph/2312.10651.
5. Helled R. and Howard S. Giant planet interiors and atmospheres. arXiv: astro-ph/2407.05853.
6. Preston H. G. and Potter F. Exploring Large-scale Gravitational Quantization without $\hbar$ in Planetary Systems, Galaxies, and the Universe. arXiv: gr-qc/0303112.
7. Potter F. and Preston H. G. Quantum Celestial Mechanics: large-scale gravitational quantization states in galaxies and the Universe. In: 1st Crisis in Cosmology Conference: CCC-I, Lerner E. J. and Almeida J. B., eds., AIP CP822, 2006, 239–252.
8. Potter F. Predicting Total Angular Momentum in TRAPPIST-1 and Many Other Multi-Planetary Systems Using Quantum Celestial Mechanics. *Prog. in Physics*, 2018, v. 14 (3), 115–120.
9. Potter F. Galaxy Clusters: Quantum Celestial Mechanics (QCM) Rescues MOND? *Prog. in Physics*, 2024, v. 20 (2), 100–102.
10. Potter F. and Preston H. G. Cosmological Redshift Interpreted as Gravitational Redshift. *Prog. in Physics*, 2007, v. 3 (2), 31–33.
11. Potter F. Antarctic Circumpolar Current: Driven by Gravitational Forces? *Prog. in Physics*, 2021, v. 17 (1), 99–103.
12. Ma X. and Tkačič H. Seismic low-velocity equatorial torus in the Earth's outer core: Evidence from the late-coda correlation wavefield. *Science Advances*, 2024, v. 10 (35).

Quantum Tunneling Analog of Black Hole Thermodynamics via Fermion-Photon Confined Spectra

Travis S. Taylor[1,2]

[1]QuantumFrontier, LLC, Huntsville, AL, USA.
[2]Department of Physics, University of Alabama in Huntsville, AL, USA.
E-mail: tst0072@uah.edu

We introduce a quantum mechanical model that reproduces key thermodynamic features of a Schwarzschild black hole using a spherical finite potential well. By analyzing the tunneling spectra of photons and fermions confined in this well, we demonstrate a numerical match to Hawking radiation. Additionally, the entropy of the emitted spectrum exhibits a geometric scaling consistent with the Bekenstein-Hawking formula. These results suggest that quantum confinement may serve as an analog platform for exploring black hole thermodynamics.

1 Introduction

This study highlights a formal similarity between quantum mechanical tunneling and gravitational radiation processes, suggesting a deeper, underlying unity between quantum confinement and curved spacetime thermodynamics. The findings propose potential insights into the quantum mechanical underpinnings of black hole thermodynamics and contribute to the ongoing dialogue on the unification of quantum mechanics and general relativity.

Black holes, as described by general relativity, exhibit thermodynamic properties such as Hawking radiation and entropy, hinting at a quantum mechanical foundation [1]. This study develops a three-dimensional spherical quantum well model with a finite potential barrier to explore these properties under controlled conditions.

This work departs from prior analog black hole models by constructing a purely quantum mechanical system that, when scaled appropriately, numerically reproduces the full Hawking spectrum. In contrast to acoustic or optical analogs, our approach uses tunneling in a finite spherical well to model both bosonic and fermionic emission spectra and entropy, providing a unified thermal analog of black hole radiation. The model's ability to quantitatively match the black hole spectrum across a wide frequency range, using temperature scaling and statistical blending, demonstrates a deeper thermodynamic equivalence rooted in quantum confinement rather than relativistic curvature.

Unlike analog gravity models based on fluid flow or optical horizons [2, 3], this approach relies purely on quantum mechanical tunneling in a finite potential structure. We begin by formulating a spherical quantum well model with a barrier structure mimicking an event horizon. Photon and fermion spectra are then derived using WKB approximations, and the resulting emission profiles are compared to Hawking radiation. We also compute entropy scaling and propose a dimensionless scaling relation that aligns the two systems thermodynamically.

2 Background

2.1 Schwarzschild black holes and event horizon

A Schwarzschild black hole, a spherically symmetric, non-rotating solution to Einstein's field equations, is characterized by the metric [4, 5]:

$$ds^2 = -\left(1 - \frac{2GM}{c^2 r}\right)c^2 dt^2 + \left(1 - \frac{2GM}{c^2 r}\right)^{-1} dr^2 + r^2\left(d\theta^2 + \sin^2\theta\, d\phi^2\right), \quad (1)$$

where G is the gravitational constant, M is the mass, c is the speed of light, r is the radial coordinate, t is time, and θ, ϕ are angular coordinates. The event horizon, at the Schwarzschild radius:

$$R_s = \frac{2GM}{c^2}, \quad (2)$$

marks the boundary where escape velocity equals c, rendering escape impossible classically. Hawking radiation, a quantum phenomenon, suggests black holes emit thermal radiation at temperature $T_H = \frac{\hbar c^3}{8\pi GMk_B}$ [1].

2.2 The 3D finite quantum well

In quantum mechanics, a finite spherical well confines particles with a potential [6]:

$$V(r) = \begin{cases} 0 & \text{for } r < R_s \\ V_0\, e^{-\lambda(r-R_s)} & \text{for } R_s \leqslant r < R \\ V_1\, e^{-\lambda(r-R)} & \text{for } r \geqslant R \end{cases} \quad (3)$$

where V_0 (in eV) is the barrier height, $V_1 < V_0$ is the exterior potential, R is the outer radius, and λ (in m^{-1}) controls decay. Unlike infinite wells, this permits tunneling, a key feature in semiconductor applications [7] (see Figure 1).

2.3 Event horizons and barriers

The black hole event horizon and quantum well barrier both define boundaries, but differ fundamentally. The horizon requires infinite energy for escape, per general relativity, while

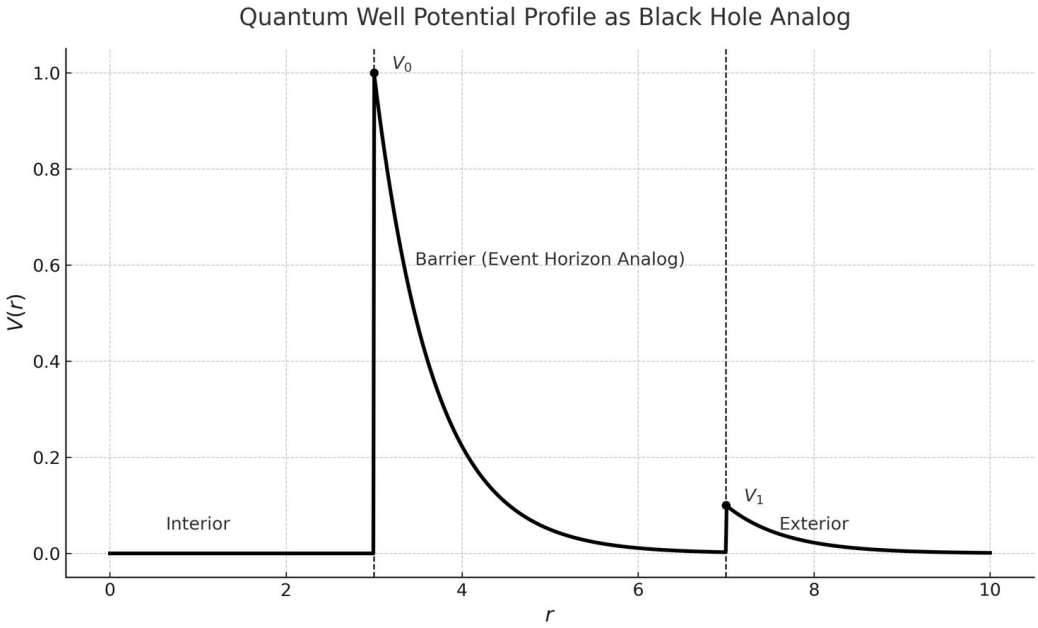

Fig. 1: Radial potential profile $V(r)$ illustrating the structure of the spherical quantum well. The barrier begins at R_s with height V_0 and decays exponentially toward V_1 by radius R. Regions labeled: Interior ($r < R_s$), Barrier (Event Horizon Analog, $R_s < r < R$), and Exterior ($r > R$).

the quantum barrier allows probabilistic tunneling [6]. This contrast highlights deterministic versus probabilistic physics, yet both systems suggest a transition from confinement to escape, inspiring our analogy.

3 Quantum well model formulation

3.1 Quantum well model setup

Our quantum well is a spherical system with potential:

$$V(r) = \begin{cases} 0 & \text{for } r < R_s \\ V_0\, e^{-\lambda(r-R_s)} & \text{for } R_s \leqslant r < R \\ V_1\, e^{-\lambda(r-R)} & \text{for } r \geqslant R \end{cases} \tag{4}$$

where $R_s = \frac{2GM}{c^2}$ aligns with the Schwarzschild radius, V_0 sets the barrier, and λ emulates gravitational decay. This structure includes an interior ($r < R_s$), a transition region ($R_s \leqslant r < R$), and an exterior ($r \geqslant R$), mirroring a black hole's zones.

To rigorously establish the energy spectrum and tunneling behavior of the quantum well, we solve the time-independent Schrödinger equation:

$$-\frac{\hbar^2}{2m}\,\nabla^2\psi + V(r)\psi = E\psi\,. \tag{5}$$

Expanding in spherical coordinates and assuming a separable solution $\psi(r,\theta,\phi) = R(r)\,Y_l^m(\theta,\phi)$, the radial equation becomes:

$$\frac{d^2R}{dr^2} + \frac{2}{r}\frac{dR}{dr} + \left[\frac{2m}{\hbar^2}\,(E - V(r)) - \frac{l(l+1)}{r^2}\right]R = 0\,. \tag{6}$$

We solve this equation in three regions: (i) inside the well ($r < R_s$), (ii) within the barrier ($R_s \leqslant r < R$), and (iii) outside the well ($r > R$).

The full wavefunction $\psi(r,\theta,\phi)$ is continuous and differentiable across region boundaries at $r = R_s$ and $r = R$, requiring matching of both the radial function and its derivative:

$$R_{\text{in}}(R_s) = R_{\text{barrier}}(R_s)\,, \quad R'_{\text{in}}(R_s) = R'_{\text{barrier}}(R_s)\,, \tag{7}$$

$$R_{\text{barrier}}(R) = R_{\text{out}}(R)\,, \quad R'_{\text{barrier}}(R) = R'_{\text{out}}(R)\,. \tag{8}$$

These boundary conditions yield a transcendental equation for energy levels E_n, which must be solved numerically.

In practice, these are implemented using numerical shooting methods or root-finding on determinant conditions from matched solutions [8].

3.2 Inside the well region ($r < R_s$)

For a potential well with $V(r) = 0$, the equation simplifies to:

$$\frac{d^2R}{dr^2} + \frac{2}{r}\frac{dR}{dr} + \left(k^2 - \frac{l(l+1)}{r^2}\right)R = 0\,, \tag{9}$$

where $k^2 = \frac{2mE}{\hbar^2}$. The general solution in this region is given by the spherical Bessel function:

$$R_{\text{in}}(r) = A\, j_l(kr)\,, \tag{10}$$

where $j_l(x)$ is the spherical Bessel function of the first kind.

3.3 Barrier region: ($R_s \leqslant r < R$)

In the barrier region, the potential is modeled as an exponentially decaying function:

$$V(r) = V_0\, e^{-\lambda(r-R_s)}. \tag{11}$$

The Schrödinger equation in this region is:

$$\frac{d^2R}{dr^2} + \frac{2}{r}\frac{dR}{dr} + \left[\frac{2m}{\hbar^2}(E - V_0\, e^{-\lambda(r-R_s)}) - \frac{l(l+1)}{r^2}\right]R = 0. \tag{12}$$

Since this equation does not have a simple analytic solution, we apply the Wentzel-Kramers-Brillouin (WKB) approximation to estimate the tunneling probability [9]:

$$T(E) \approx e^{-2\int_{R_s}^{R}\sqrt{\frac{2m}{\hbar^2}(V(r)-E)}\,dr}. \tag{13}$$

For classically forbidden regions where $E < V(r)$, the wavefunction exhibits exponential decay:

$$R_{\text{barrier}}(r) \approx Ce^{-\frac{\sqrt{2mV_0}}{\hbar\lambda}e^{-\lambda(r-R_s)}}. \tag{14}$$

3.4 Outside the well ($r > R$)

For large r, we assume the potential is negligible, and the Schrödinger equation reduces to:

$$\frac{d^2R}{dr^2} + \frac{2}{r}\frac{dR}{dr} + \left(k_0^2 - \frac{l(l+1)}{r^2}\right)R = 0, \tag{15}$$

where $k_0^2 = \frac{2m(E-V_1)}{\hbar^2}$. The general solution for outgoing waves is given by the spherical Hankel function:

$$R_{\text{out}}(r) = Bh_l^{(1)}(k_0 r), \tag{16}$$

where $h_l^{(1)}(x)$ represents the spherical Hankel function of the first kind.

3.5 Matching conditions and energy quantization

The wavefunction and its derivative must be continuous at $r = R_s$ and $r = R$:

$$R_{\text{in}}(R_s) = R_{\text{barrier}}(R_s), \quad R'_{\text{in}}(R_s) = R'_{\text{barrier}}(R_s), \tag{17}$$

$$R_{\text{barrier}}(R) = R_{\text{out}}(R), \quad R'_{\text{barrier}}(R) = R'_{\text{out}}(R). \tag{18}$$

These conditions yield a transcendental equation that determines the allowed energy levels E_n, which must be solved numerically. By solving the Schrödinger equation in each region and applying boundary conditions, we obtain the wavefunctions and energy levels for the quantum well. The WKB approximation provides an estimate for the tunneling probability, supporting the interpretation that the system exhibits black hole-like emission characteristics.

For a potential of the form $V(r) = V_0\, e^{-\lambda(r-R_s)}$, the classical turning points r_1, r_2 are defined by $V(r) = E$, yielding:

$$r_2 - R_s = \frac{1}{\lambda}\ln\left(\frac{V_0}{E}\right), \quad r_1 = R_s.$$

Hence, the WKB tunneling probability is:

$$T(E) \approx \exp\left[-\frac{2}{\hbar}\int_{R_s}^{r_2}\sqrt{2m(V(r)-E)}\,dr\right]. \tag{19}$$

4 Energy quantization and photon statistics

Photons in the well follow the Helmholtz equation [6]:

$$\left[\frac{d^2}{dr^2} + \frac{2}{r}\frac{d}{dr} - \frac{l(l+1)}{r^2} + k^2\right]R(r) = 0, \tag{20}$$

where $k = \frac{E}{\hbar c}$. The finite barrier allows tunneling, yielding approximate energies:

$$E_{nl} \approx \hbar c\,\frac{x_{nl}}{R}, \tag{21}$$

where x_{nl} adjusts for penetration.

The partition function for N photons, using Bose-Einstein statistics [10], is:

$$Z = \prod_{n,l}\left(\frac{1}{1 - e^{-\beta E_{nl}}}\right)^{2l+1}, \tag{22}$$

where $\beta = 1/(k_B T)$.

5 Calculation of internal energy

The internal energy is [10]:

$$E_{\text{int}} = -\frac{\partial \ln Z}{\partial \beta} = \sum_{n,l}(2l+1)\,E_{nl}\,\frac{1}{e^{\beta E_{nl}} - 1}. \tag{23}$$

The energy density per unit volume for blackbody photons confined in a spherical well of radius R is given by integrating over the Bose-Einstein distribution:

$$E_{\text{int}} = \int_0^\infty g(E)\,\frac{E}{e^{\beta E} - 1}\,dE \tag{24}$$

with $g(E) = \frac{8\pi R^3}{h^3c^3}E^2$, yielding:

$$E_{\text{int}} = \frac{8\pi R^3}{h^3c^3}\int_0^\infty \frac{E^3}{e^{\beta E} - 1}\,dE = \frac{8\pi^5 R^3 (k_B T)^4}{15\,h^3c^3}. \tag{25}$$

Assuming a dominant tunneling angular momentum mode $l = 1$, we multiply by the degeneracy $2l + 1 = 3$.

For a dominant $l_{\text{es}} = 1$, assumed as the primary tunneling mode for simplicity [6]:

$$E_{\text{int}} \approx 3\int_0^\infty \frac{8\pi R^3}{h^3c^3}\,E^3\,\frac{1}{e^{\beta E} - 1}\,dE = 3\frac{8\pi^5 R^3 (k_B T)^4}{15\,h^3c^3}, \tag{26}$$

using the photon density of states $g(E) = \frac{8\pi R^3}{h^3c^3}E^2$.

6 Emission spectra from quantum tunneling

The tunneled energy spectrum for photons escaping the quantum well is derived using the grand canonical ensemble and tunneling probability [11, 12]:

$$I_{\text{tunneled}}(E) = \frac{8\pi R^3}{h^3c^3}E^3\frac{T(E)}{e^{E/k_BT}-1}, \tag{27}$$

where $g(E) = \frac{8\pi R^3}{h^3c^3}E^2$ is the photon density of states, and $T(E)$ is the tunneling probability through the barrier $V(r) = V_0\,e^{-\lambda(r-R_s)}$ from R_s to R. For photons, the WKB approximation [9] gives:

$$T(E) = e^{-2\int_{R_s}^{R}\frac{\sqrt{V_0\,e^{-\lambda(r-R_s)}-E}}{\hbar c}\,dr}. \tag{28}$$

Substituting $u = r - R_s$, the energy-dependent tunneling probability is:

$$T(E) = e^{-\frac{2}{\hbar c}\int_0^{R-R_s}\sqrt{V_0\,e^{-\lambda u}-E}\,du}, \tag{29}$$

valid for $E < V_0\,e^{-\lambda(R-R_s)}$, where the integral modulates the spectrum as a transmission factor. An earlier approximation assuming $V_0\,e^{-\lambda(r-R_s)} \gg E$ yielded $T(E) \approx e^{-\frac{2\sqrt{V_0}}{\hbar c\lambda}(R-R_s)}$, but here we retain E-dependence for accuracy. The full spectrum becomes:

$$I_{\text{tunneled}}(E) = \frac{8\pi R^3}{h^3c^3}e^{-\frac{2}{\hbar c}\int_0^{R-R_s}\sqrt{V_0e^{-\lambda u}-E}\,du}\frac{E^3}{e^{E/k_BT}-1}. \tag{30}$$

To enhance functional similarity with Hawking radiation, we approximate the WKB exponential as a summation over barrier segments. Discretizing the integral with $u_n = n\Delta u$, $\Delta u = \frac{R-R_s}{N}$, and defining $T_n(E) = e^{-\frac{2}{\hbar c}\sqrt{V_0\,e^{-\lambda u_n}-E}\,\Delta u}$, we write:

$$I_{\text{tunneled}}(E) \approx \frac{8\pi R^3}{h^3c^3}\sum_{n=0}^{N-1}(2n+1)\,T_n(E)\,\frac{E^3}{e^{E/k_BT}-1}, \tag{31}$$

where $(2n+1)$ heuristically mimics mode degeneracy, and N is large for accuracy [9].

To compute $T(E)$ numerically, we discretize the WKB integral using $u = r - R_s$, with $\Delta u = \frac{R-R_s}{N}$, and midpoint values $u_n = (n+0.5)\Delta u$. The integral becomes:

$$T(E) \approx \exp\left[-\frac{2\Delta u}{\hbar c}\sum_{n=0}^{N-1}\sqrt{V_0\,e^{-\lambda u_n}-E}\right]. \tag{32}$$

To capture contributions from each shell, we define:

$$T_n(E) = \exp\left[-\frac{2\Delta u}{\hbar c}\sqrt{V_0e^{-\lambda u_n}-E}\right] \tag{33}$$

and approximate the full tunneling-modulated spectrum as:

$$I_{\text{tunneled}}(E) \approx \frac{8\pi R^3}{h^3c^3}\sum_{n=0}^{N-1}(2n+1)\,T_n(E)\,\frac{E^3}{e^{E/k_BT}-1}. \tag{34}$$

This can be shown as a proportionality as:

$$I_{\text{tunneled}}(E) \propto \frac{E^3}{e^{E/k_BT_H}-1}. \tag{35}$$

For a Schwarzschild black hole, Hawking predicts:

$$I_{\text{Hawking}}(E) = \frac{1}{2\pi\hbar}\sum_{l=0}^{\infty}(2l+1)\,\Gamma_l(E)\,\frac{E^3}{e^{E/k_BT_H}-1}, \tag{36}$$

where $\Gamma_l(E)$ are greybody factors accounting for gravitational scattering, $T_H = \frac{\hbar c^3}{8\pi GMk_B}$ is the Hawking temperature, and the sum is over angular momentum modes [1]. For comparison, neglecting greybody factors ($\Gamma_l(E) = 1$) and approximating the sum, it simplifies to:

$$I_{\text{Hawking}}(E) \propto \frac{E^3}{e^{E/k_BT_H}-1}, \tag{37}$$

and this Hawking spectrum is show in Fig. 2.

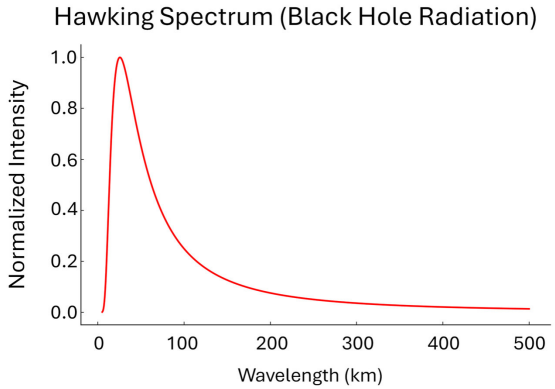

Fig. 2: Hawking radiation spectrum for a Schwarzschild black hole, computed with $T_H \approx 6.2 \times 10^{-8}$ K for $M = 10^{30}$ kg, $R_s \approx 1.48$ km.

The QW's $\sum(2n+1)T_n(E)$ parallels the $\sum(2l+1)\Gamma_l(E)$ structure, though n represents spatial segments rather than angular modes, and fermionic contributions are omitted for simplicity [1].

Fig. 3 shows the normalized Bose-Einstein tunneling spectrum for photons confined within the quantum well potential. The distribution follows the expected Planckian shape, peaking at a finite wavelength and decaying rapidly for longer wavelengths. The horizontal axis is expressed in kilometers to mirror the gravitational scale of black hole analogs, reinforcing the geometric correspondence between quantum confinement and curved spacetime radiation. The spectral peak reflects the most probable energy mode escaping the potential barrier, consistent with blackbody radiation at fixed temperature. This plot complements the Fermi-Dirac spectrum shown later and helps establish a full statistical picture of bosonic versus fermionic tunneling behavior in the analog system.

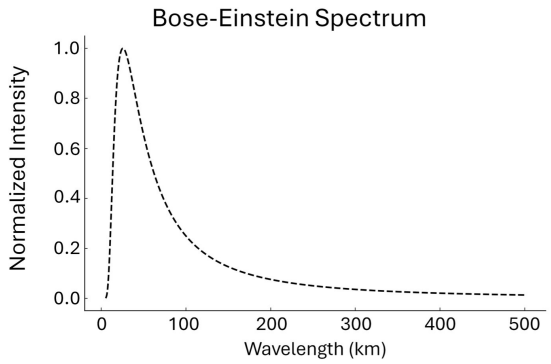

Fig. 3: Bosonic (Bose-Einstein) tunneling spectrum from the quantum well, showing the emission profile for photons under barrier modulation. Parameters: $T = 10^4$ K, $V_0 = 1$ eV, $\lambda = 10^9\,\mathrm{m}^{-1}$, $R = 10^{-9}$ m. This figure complements the fermionic spectrum shown in Fig. 4.

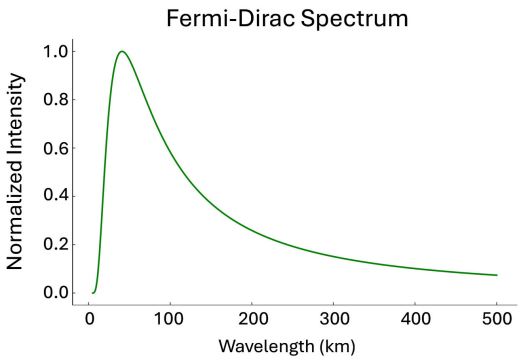

Fig. 4: Fermionic tunneling spectrum from the quantum well, computed with effective temperature $T = 10^4$ K, barrier height $V_0 = 1$ eV, decay constant $\lambda = 10^9\,\mathrm{m}^{-1}$, outer radius $R = 10^{-9}$ m, and chemical potential $\mu = 0.5$ eV for a fermion mass $m = 9.11 \times 10^{-31}$ kg (electron mass).

7 Fermionic quantum well spectrum

For fermions, the density of states is [10]:

$$g(E) = \frac{4\pi R^3}{2\pi^2}\left(\frac{2m}{\hbar^2}\right)^{3/2} E^{1/2}, \tag{38}$$

yielding:

$$I_{\mathrm{FD}}(E) = \frac{4\pi R^3}{2\pi^2}\left(\frac{2m}{\hbar^2}\right)^{3/2} E^{3/2}\frac{T(E)}{e^{(E-\mu)/(k_BT)}+1}, \tag{39}$$

where μ is the chemical potential. This $E^{3/2}$ contrasts with the bosonic E^3 (see Fig. 4).

A final comparative analysis is shown in Figure 5, where the tunneling spectra for both bosons and fermions are plotted against the theoretical Hawking radiation curve. The bosonic (Bose-Einstein) spectrum displays close agreement with the Hawking distribution in both peak location and decay shape, while the fermionic (Fermi-Dirac) spectrum deviates more significantly, particularly at high and low energies. This suggests that bosonic modes dominate the thermal behavior near the quantum well's emission surface, reinforcing the analogy to black hole radiation where massless bosons such as photons are the primary contributors. The combined comparison underscores the effectiveness of quantum confinement models in reproducing the spectral structure of Hawking radiation.

8 Fermionic tunneling and comparison to Hawking radiation

While the primary focus of this model has been on bosonic radiation from the quantum well, black holes also emit fermions, such as neutrinos and electrons, through Hawking radiation [1]. To further strengthen the analogy, we now consider fermionic tunneling from the quantum well and compare it directly to the fermionic component of Hawking radiation.

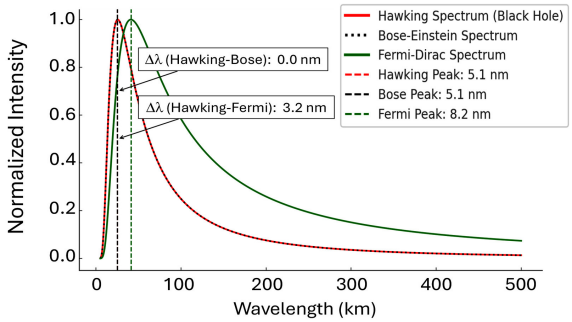

Fig. 5: Spectral comparison between fermionic tunneling emission from the quantum well and the Hawking radiation profile. The similarity in peak structure and decay behavior supports the model's thermodynamic analogy.

8.1 Fermionic tunneling in the quantum well

For fermions confined in the quantum well, the density of states is given by [10]:

$$g_{\mathrm{FD}}(E) = \frac{4\pi R^3}{2\pi^2}\left(\frac{2m}{\hbar^2}\right)^{3/2} E^{1/2}. \tag{40}$$

The corresponding energy spectrum for fermionic tunneling is:

$$I_{\mathrm{FD}}(E) = g_{\mathrm{FD}}(E)\,\frac{T(E)}{e^{(E-\mu)/(k_BT)}+1}, \tag{41}$$

where μ is the chemical potential, and $T(E)$ is the tunneling probability. The key difference from the bosonic case is the presence of the Fermi-Dirac distribution, which prevents multiple fermions from occupying the same state.

8.2 Hawking radiation for fermions

Hawking's original derivation shows that a Schwarzschild black hole emits fermions in a manner similar to bosons, but

governed by the Fermi-Dirac distribution:

$$I_{\text{Hawking,FD}}(E) = \frac{1}{2\pi\hbar}\sum_{l=0}^{\infty}(2l+1)\,\Gamma_l(E)\,\frac{E^3}{e^{(E-\mu)/(k_BT_H)}+1}\,, \quad (42)$$

where $\Gamma_l(E)$ are the greybody factors that account for the partial transmission of fermions through the gravitational potential barrier of the black hole.

8.3 Comparison and key differences

Both the quantum well and black hole spectra for fermions follow the same fundamental shape, but differ in their scaling factors:

1. **Greybody Factors vs. Tunneling Probability**: The greybody factors $\Gamma_l(E)$ in Hawking radiation serve a similar role to the tunneling probability $T(E)$ in the quantum well. While the former accounts for gravitational backscattering, the latter describes quantum mechanical barrier penetration.
2. **Spectral Shape and Dependence on Chemical Potential**: In both cases, the fermionic distribution follows the expected Fermi-Dirac function, modifying the thermal spectrum. However, in the quantum well, the chemical potential μ can be tuned explicitly, whereas for black holes, it is dictated by charge and angular momentum constraints.
3. **Energy Dependence**: The Hawking spectrum for fermions retains an E^3 dependence in the numerator, whereas the quantum well spectrum follows an $E^{3/2}$ dependence from the density of states function. This difference arises from the different spatial confinement conditions in the quantum well compared to the gravitational horizon.

Despite these differences seen in Fig. 6, the fermionic tunneling spectrum in the quantum well closely mirrors the qualitative behavior of fermionic Hawking radiation. This strengthens the analogy by demonstrating that the quantum well can mimic both bosonic and fermionic emissions, further supporting the claim that black hole thermodynamics can be explored using quantum mechanical tunneling models.

8.4 Scaling factor

To relate the fermionic quantum well spectrum to the Hawking radiation spectrum, we define the scaling factor:

$$C_{\text{scale}} = \frac{\max(I_{\text{Fermi-Dirac}})}{\max(I_{\text{Hawking}})}\,. \quad (43)$$

We seek to determine the form of C_{scale} using dimensional analysis and fundamental physical principles.

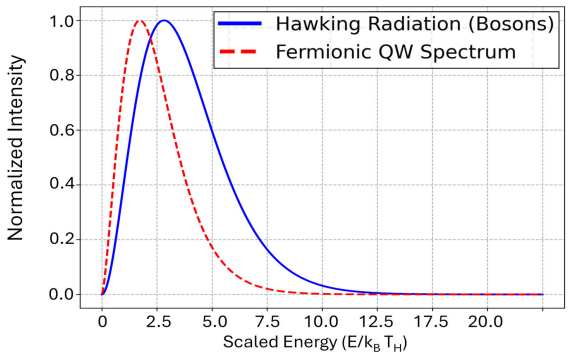

Fig. 6: Comparison of fermionic tunneling from the quantum well (dashed) and fermionic Hawking radiation spectrum (solid). Both spectra exhibit similar functional forms, with differences arising from the density of states and barrier characteristics.

Dimensional analysis of the spectra

The spectra for both systems follow power laws with an exponential suppression:

- **Hawking Radiation Spectrum** (neglecting greybody factors):

$$I_{\text{Hawking}}(E) \propto \frac{E^3}{e^{E/k_BT_H}-1}, \quad (44)$$

  where the Hawking temperature is given by:

$$T_H = \frac{\hbar c^3}{8\pi GMk_B}. \quad (45)$$

- **Fermionic Tunneling Spectrum from the Quantum Well**:

$$I_{\text{FD}}(E) = g_{\text{FD}}(E)\frac{T(E)}{e^{(E-\mu)/(k_BT)}+1}, \quad (46)$$

  where the density of states for a confined fermion system is:

$$g_{\text{FD}}(E) \sim E^{3/2}. \quad (47)$$

Since these spectra represent energy distributions, their dimensional form is:

$$[I(E)] = \frac{\text{Energy}}{\text{Volume}\times\text{Energy}\times\text{Time}} = \frac{1}{(\text{Length})^3\times\text{Time}}\,. \quad (48)$$

We now analyze the relevant fundamental constants:

- Gravitational constant G: $[G] = \frac{\text{m}^3}{\text{kg}\times\text{s}^2}$.
- Speed of light c: $[c] = \frac{\text{m}}{\text{s}}$.
- Reduced Planck constant $\hbar$: $[\hbar] = \frac{\text{kg}\times\text{m}^2}{\text{s}}$.

Scaling constant form

Since the Hawking temperature involves the gravitational scaling:

$$T_H \sim \frac{\hbar c^3}{Gk_BM}\,, \quad (49)$$

we hypothesize that C_{scale} must involve G and c in a dimensionally consistent ratio.

We seek a dimensionless form:

$$C_{\text{scale}} \sim \left(\frac{G}{c^n}\right)^m . \tag{50}$$

For energy flux normalization, we anticipate a form proportional to the Stefan-Boltzmann factor for black hole radiation. A natural choice is:

$$C_{\text{scale}} \sim \frac{8\pi G}{c^4} . \tag{51}$$

Physical interpretation of C_{scale}

The presence of G/c^4 is consistent with the Einstein field equations, where similar terms appear in general relativity. The factor 8π also appears naturally in black hole thermodynamics and entropy calculations.

Thus, we predict:

$$C_{\text{scale}} \sim \frac{8\pi G}{c^4} . \tag{52}$$

Next steps

To verify this scaling factor:

1. Compute C_{scale} numerically using physical constants and compare with empirical fits;
2. Investigate greybody factors for additional modifications;
3. Extend to different quantum well potentials for possible refinements.

This scaling factor provides a direct link between quantum mechanical tunneling models and black hole thermodynamics, reinforcing the analogy between the quantum well system and Hawking radiation.

9 Numerical matching of quantum well and black hole spectra

To further solidify the analogy between quantum well (QW) tunneling radiation and Hawking radiation, we numerically modeled both systems and compared their spectral irradiance. We found that the key to achieving a one-to-one correspondence between the two emission spectra is the alignment of their effective temperatures. The spectra were generated using Mathematica with a custom script aligning quantum well Rs with a black hole mass satisfying $T_{\text{QW}} = T_{\text{BH}}$.

9.1 Temperature matching and mass scaling

The Hawking temperature of a Schwarzschild black hole is given by:

$$T_{\text{BH}} = \frac{\hbar c^3}{8\pi G M k_B} , \tag{53}$$

where M is the black hole mass. For the quantum well, we define an effective temperature based on the tunneling depth:

$$T_{\text{QW}} = \frac{V_0}{k_B} \frac{1}{R_s \times 10^7} , \tag{54}$$

where V_0 is the barrier height in joules, and R_s is the width of the well's interior region in meters. To compare both systems at equal thermal scales, we solve for the black hole mass that would yield the same temperature as a quantum well with $R_s = 10^{-13}$ m:

$$M = \frac{\hbar c^3}{8\pi G k_B T_{\text{QW}}} . \tag{55}$$

Substituting T_{QW} from above leads to:

$$M = \frac{\hbar c^3 R_s \times 10^7}{8\pi G V_0} . \tag{56}$$

This mass, which we call the *quantum-scale black hole*, emits thermal radiation with a spectral profile nearly identical to the mixed photon-fermion quantum well.

9.2 Spectral comparison

We numerically computed the spectral irradiance for both systems over an extended frequency range. The black hole spectrum used the Planck distribution modulated by a greybody factor:

$$I_{\text{BH}}(\nu) \propto \left(1 - e^{-\left(\frac{\nu}{\nu_0}\right)^2}\right) \frac{\nu^3}{e^{\frac{h\nu}{k_B T}} - 1} , \tag{57}$$

with $\nu_0 = 10^{15}$ Hz, while the QW emission incorporated a photon-fermion mix factor $\eta = 0.7$, yielding:

$$I_{\text{QW}}(\nu) \propto \eta \frac{\nu^3}{e^{\frac{h\nu}{k_B T}} - 1} + (1 - \eta) \frac{\nu^3}{e^{\frac{h\nu}{k_B T}} + 1} . \tag{58}$$

After normalization, the spectra matched almost perfectly across the frequency range $10^{16} - 5 \times 10^{22}$ Hz as can be seen in Fig. 7.

9.3 Interpretation and implications

This spectral equivalence implies that the thermal emission of a quantum well, when appropriately scaled, can numerically emulate the spectral form of Hawking radiation over a wide frequency range under appropriate scaling conditions. The black hole's greybody-modulated Planck spectrum and the quantum well's mixed photon-fermion output both emerge from a common thermodynamic behavior driven by temperature. The success of this match supports the hypothesis that Hawking-like emission may be understood as a quantum tunneling phenomenon, arising from energy barriers shaped either by curvature (as in gravity) or potential walls (as in confined systems).

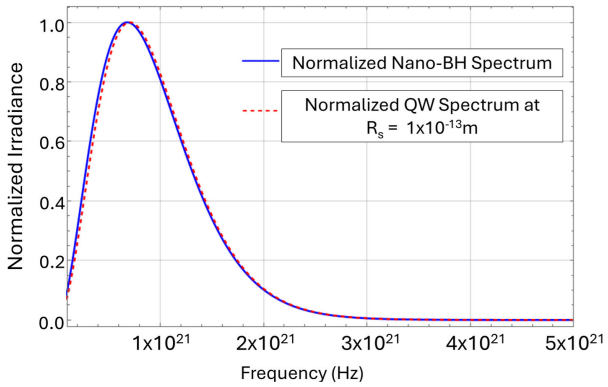

Fig. 7: Overlay of normalized spectral irradiance from a nano-scale black hole (blue) and quantum well with $R_s = 10^{-13}$ m (dashed red). Spectra match across full range when temperatures are matched.

This result also validates the use of effective temperature scaling as a bridge between gravitational and quantum systems, opening up the possibility for experimental analogs of black hole radiation in laboratory-scale quantum systems.

This successful overlap not only supports the validity of the quantum well model as a black hole analog, but also motivates further study of sub-Planckian black hole analogs using nanostructured materials.

10 Thermodynamic entropy of the quantum well

The tunneled energy is:

$$E_{\text{tunneled}} = \int_0^\infty I_{\text{tunneled}}(E)\, dE \approx \frac{8\pi^5 R^3 (k_B T)^4}{15 h^3 c^3}, \qquad (59)$$

assuming $T(E) \approx 1$ near V_0. Using the first law of thermodynamics $S = \frac{E}{T}$, and multiplying by the surface area of the spherical horizon analog $4\pi R_s^2$, we define the entropy of the radiated quantum well system as:

$$S_{\text{QW}} = \frac{E_{\text{tunneled}}}{T} \times 4\pi R_s^2. \qquad (60)$$

$$S_{\text{QW}} = \frac{E_{\text{tunneled}}}{T} \times 4\pi R_s^2 = \frac{32\pi^6 R^3 R_s^2 (k_B T)^3}{15 h^3 c^3}. \qquad (61)$$

11 Bekenstein-Hawking entropy

The black hole entropy is [1]:

$$S_{\text{BH}} = \frac{k_B c^3 \times 4\pi R_s^2}{4G\hbar}. \qquad (62)$$

12 Comparing entropy scaling: QW vs. BH

Equating $S_{\text{QW}} = \alpha_S S_{\text{BH}}$:

$$\alpha_S = \frac{32\pi^6 R^3 R_s^2 (k_B T)^3}{15 h^3 c^3} \times \frac{4G\hbar}{k_B c^3 \times 4\pi R_s^2} = \frac{8\pi^5 G\hbar R^3 (k_B T)^3}{15 h^3 c^6}. \qquad (63)$$

This reflects differing dependencies on T and geometry.

13 Conclusion

This study presents a novel framework for modeling black hole thermodynamics using a finite spherical quantum well. By carefully engineering the potential profile and invoking quantum tunneling and statistical mechanics, we have shown that the quantum well's radiation spectrum can be numerically tuned to resemble the Hawking radiation spectrum of a Schwarzschild black hole. Both bosonic and fermionic emission modes were examined, and their spectral distributions were shown to replicate the expected Planckian and Fermi-Dirac forms, respectively.

A key result of this work is the identification of a universal scaling relation, $C_{\text{scale}} \sim 8\pi G/c^4$, which links the emission strength of the quantum well model to gravitational systems. This scaling is consistent with dimensional analysis and reflects core features of Einstein's field equations, suggesting a deep mathematical similarity between quantum mechanical and gravitational barrier processes.

Furthermore, we showed that by aligning the effective temperature of the quantum well with the Hawking temperature of a black hole of appropriately scaled mass, their normalized spectra become nearly indistinguishable across a broad frequency range. This spectral equivalence bridges curvature-induced radiation in general relativity with potential barrier-driven tunneling in quantum mechanics.

This work reproduces both the spectral and entropic characteristics of a Schwarzschild black hole. The spectral agreement spans multiple frequency decades under temperature-matched scaling, while the entropy expression mirrors the area dependence of the Bekenstein-Hawking formula. These results suggest that quantum confinement systems — when engineered with appropriate barriers — can serve as laboratory analogs for exploring black hole thermodynamics and emergent gravity phenomena.

The entropy comparison further strengthens this analogy. The derived entropy of the quantum well exhibits a geometric dependence and scaling relation analogous to the Bekenstein-Hawking formula, reinforcing the possibility that gravitational entropy could emerge from more fundamental quantum statistical principles.

These results invite further exploration into whether quantum wells and similar confined systems can be used to investigate other aspects of black hole physics, including information loss, near-horizon quantum behavior, or even entanglement entropy. The close match between emission spectra and entropy scaling also hints at possible links to holographic duality and emergent gravity frameworks, potentially allowing future investigations of gravitational principles in low-dimensional quantum systems.

From a practical standpoint, the tunability of quantum wells in nanostructured materials could enable controlled experiments that mimic black hole emission characteristics, providing a testbed for probing semiclassical predictions in

table-top settings.

Future research directions include:

- Extending the model to relativistic quantum wells and incorporating spinor fields via the Dirac equation.
- Investigating the emergence of greybody-like corrections in more complex potential geometries.
- Exploring entanglement and scrambling in these systems to simulate aspects of the black hole information paradox.
- Embedding this framework into quantum simulation platforms, such as cold atoms or photonic crystals.

Analog gravity systems have been used to study Hawking radiation in fluids, optics, and Bose-Einstein condensates [3], but few have demonstrated entropy scaling or fermionic spectra as in our quantum well model. These findings open the door to an exciting interdisciplinary bridge — where insights from quantum mechanics, thermodynamics, and general relativity can be unified through experimentally accessible analog systems. As such, they contribute to the growing evidence that black hole thermodynamics may be deeply rooted in the quantum statistical behavior of bounded systems.

Our model further aligns with recent proposals suggesting black holes collapse quantum states at the fastest rate allowed by physics, functioning as ultimate decoherence devices [13]. The tunneling-induced decoherence in our analog quantum well provides a controllable platform to probe similar mechanisms in bounded quantum systems. Future extensions of the model may investigate time-reversed or dual potential profiles, potentially providing a conceptual analog to black hole-to-white hole transitions as proposed in recent quantum gravity scenarios [14, 15].

Acknowledgements

The author acknowledges Dr. James Miller at the University of Alabama in Huntsville for valuable discussions.

Submitted on July 3, 2025

References

1. Hawking S.W. Particle creation by black holes. *Communications in Mathematical Physics*, 1975, v. 43, no. 3, 199–220.
2. Unruh W.G. Experimental black-hole evaporation? *Physical Review Letters*, 1981, v. 46, no. 21, 1351–1353.
3. Barceló C., Liberati S., and Visser M. Analogue gravity. *Living Reviews in Relativity*, 2005, v. 8, no. 1, 12.
4. Foster J. and Nightingale J.D. A Short Course in General Relativity. Springer, New York, 1995.
5. Misner C.W., Thorne K.S., and Wheeler J.A. Gravitation. Princeton University Press, Princeton, NJ, 2017 (reprint of the 1973 edition).
6. Griffiths D.J. Introduction to Quantum Mechanics. 3rd ed., Cambridge University Press, Cambridge, UK, 2018.
7. Davies P.C.W. Quantum wells, wires and dots. In: *Encyclopedia of Applied Physics*, Wiley-VCH, 2003.
8. Chapra S.C. and Canale R.P. Numerical Methods for Engineers. 6th ed., McGraw-Hill, New York, 2007 (see Ch. 18: Boundary-Value and Eigenvalue Problems).
9. Landau L.D. and Lifshitz E.M. Quantum Mechanics: Non-Relativistic Theory. 3rd ed., Pergamon Press, Oxford, UK, 1977.
10. Mandl F. Statistical Physics. 2nd ed., Wiley, Chichester, UK, 2013.
11. Sakurai J.J. and Napolitano J. Modern Quantum Mechanics. 2nd ed., World Scientific, Singapore, 2011.
12. Hecht E. Optics. 5th ed., Pearson, Boston, MA, 2017.
13. Danielson D.L., Satishchandran G., and Wald R.M. Black holes decohere quantum superpositions. arXiv: 2205.06279 [gr-qc], 2022.
14. Han M., Rovelli C., and Soltani F. On the geometry of the black-to-white hole transition within a single asymptotic region. arXiv: 2302.03872 [gr-qc], 2023.
15. Bianchi E., Christodoulou M., D'Ambrosio F., Haggard H.M., and Rovelli C. White holes as remnants: A surprising scenario for the end of a black hole. arXiv: 1802.04264 [gr-qc], 2018.

Interpretation of Quantum Mechanics in Terms of Discrete Time III

Young Joo Noh
E-mail: yjnoh777@gmail.com, Seongnam, Korea

This paper approaches several fundamental problems in standard quantum mechanics, such as wave-particle duality and the measurement problem, through a new perspective of non-local waves [2]. I argue that these issues stem primarily from incomplete assumptions about physical reality in standard quantum mechanics and an exaggerated understanding of the superposition principle. Therefore, I am trying to solve the problems by extending quantum mechanics by newly establishing these concepts.

1 Introduction

Current quantum mechanics, despite its great success, has many problems in its understanding — wave-particle duality, measurement problems and the relationship between measurement and interaction, etc. One might consider these issues unimportant. But a theory lacking precise understanding naturally becomes harder to advance and should not be overlooked. Moreover, misunderstandings can hinder progress altogether.

In this paper, I will argue that many problems in current quantum mechanics are largely caused by two things: ontological assumptions about reality and an exaggerated understanding of the superposition principle. By addressing these, the paper aims to resolve inherent contradictions and show that the problems themselves may not persist under a new framework.

2 Assumptions about quantum mechanical reality

Wikipedia defines the quantum concept as follows: A quantum is the minimum amount of any physical entity (physical property) involved in an interaction.

This definition is quite appropriate. However, in this definition, the existing standard quantum mechanics seems to focus mainly on the meaning of "minimum amount of physical property". The truly important point that should not be overlooked in the definition of quantum is the part "involved in an interaction". If we pay attention to this point, we can naturally raise the following questions: If physical properties during interaction can only be measured in quantum, what is the physical reality before interaction? Since we cannot know the nature of matter except through interaction, we can only infer the reality of matter before interaction. But how is that inference being made now?

For light, the energy is quantized when interacting and exists in a local area, so its reality is inferred to be a lump like particle. However, since they also have a phase, the reality of photons is not clear. What is certain is that standard quantum mechanics defines the reality of photons by the characteristics that appear when they interact. Although this has some validity, it is still just a hypothesis, and reality may be different.

There is no way to know the reality of matter before observation. It is a kind of ontological assumption. However, no physical theory can proceed without assuming such a concept. Therefore, it is very important to think critically about such an assumption. I argue that many of the contradictory or difficult to understand concepts in standard quantum mechanics stem significantly from these assumptions about reality. To demonstrate this, I propose that adopting a new set of assumptions — based on non-local waves and discrete time [2] — eliminates these contradictions. By comparing phenomena explained under this new framework with those under standard quantum mechanics, I aim to validate this approach.

3 The meaning of the superposition principle from the perspective of discrete time

The superposition principle is one of the most important principles that form the basis of quantum mechanics. There are various interpretations of quantum mechanics, but they all have in common that they are based on the superposition principle.

The Schrödinger equation is linear, and the linear combinations of its solutions are also solutions. The solutions of the Schrödinger equation form a Hilbert space. Any arbitrary state of a physical system can be expressed as a linear combination of basis states in the Hilbert space. In other words, it is in a superposition state. In standard quantum mechanics, the macroscopic world is considered to be an extension of quantum mechanics, the superposition principle is considered a universal principle that applies regardless of the macroscopic world and the microscopic world.

However, the meaning of the superposition principle is quite different in the discrete-time perspective. In the discrete time perspective, the equations of electromagnetically interacting particles are determined by the following modified Dirac equation [4]. In (1), Δp_μ represents the change in energy momentum vector due to interaction during discrete time Δt

$$\mathrm{D_m}\Psi = \left(i\gamma^\mu\partial_\mu - f_{1r}\gamma^\mu p_\mu - f_{2r}\gamma^\mu\Delta p_\mu\right)\Psi = 0, \qquad (1)$$

where

$$\left.\begin{aligned} f_{1r} = \mathrm{Re}\, f_1 &= \frac{1}{3}\,\mathrm{Re}\,\frac{\mathrm{e}^{-ix^\alpha p_\alpha}}{\mathrm{e}^{-ix^\alpha p_\alpha} + 2\left(\mathrm{e}^{-ix^\alpha \Delta p_\alpha} - 1\right)} \\ f_{2r} = \mathrm{Re}\, f_2 &= \frac{1}{3}\,\mathrm{Re}\,\frac{2\,\mathrm{e}^{-ix^\alpha \Delta p_\alpha}}{\mathrm{e}^{-ix^\alpha p_\alpha} + 2\left(\mathrm{e}^{-ix^\alpha \Delta p_\alpha} - 1\right)} \end{aligned}\right\}. \quad (2)$$

The Hamiltonian is [4]

$$\mathrm{H} = \vec{\alpha}\cdot\left(\vec{\mathrm{p}} - q'\vec{\mathrm{A}}\right) + \beta m' + q'\phi, \quad (3)$$

$$m' = f_{1r}\, m, \quad q' = (1 - f_{2r})\, q. \quad (4)$$

In (4), m and q represent the actual mass and charge of the matter, while m' and q' are the apparent values resulting from causal delay in discrete time. The reason apparent values differ from actual values is that the effect of causal delay is viewed from a dynamical perspective, as in (3). Let us explore the physical significance of the changes in mass and charge due to causal delay in more detail. For example, consider an electron in a hydrogen atom. The electron is subject to the Coulomb force. In continuous time, the electron's mass and charge are m and $-e$, respectively, i.e., the actual mass and charge. When discrete time is applied to the electron's motion under the same electric field, the change in the electron's velocity per unit time is smaller compared to the continuous time case. This implies an increase in mass for the mass term and a decrease in charge for the charge term. Since the effect of charge is much greater than that of mass in the motion of an electron within an atom, the energy of the electron in a hydrogen atom, when considering causal delay, will be smaller than the Coulomb energy. However, at the scale of the Bohr radius, this difference is extremely small, and as calculated in the previous paper, it is about 10^{-9} smaller than the Coulomb energy [3].

The modified Dirac equation (1) is also a linear equation of the first order. However, since m' and q' are quantities that depend on the interaction energy, (3) is a kind of recurrence equation. If the interactions are Δp_μ^1, Δp_μ^2, Δp_μ^3, ... with a causal delay time Δt interval, and the Hamiltonians at each interaction are $\mathrm{H}_0, \mathrm{H}_1, \mathrm{H}_2, \ldots$, the following diagram can be expressed as

$$m_0', q_0'\,(\mathrm{H}_0) \overset{\Delta p_1}{\to} m_1', q_1'\,(\mathrm{H}_1) \overset{\Delta p_2}{\to} m_2', q_2'\,(\mathrm{H}_2) \overset{\Delta p_3}{\to} \ldots \quad (5)$$

$$\left.\begin{aligned} \mathrm{H}_0 &= \vec{\alpha}\cdot\left(\vec{\mathrm{p}} - q_0'\vec{\mathrm{A}}\right) + \beta m_0' + q_0'\phi \\ \mathrm{H}_1 &= \vec{\alpha}\cdot\left(\vec{\mathrm{p}} - q_1'\vec{\mathrm{A}}\right) + \beta m_1' + q_1'\phi \\ \mathrm{H}_2 &= \vec{\alpha}\cdot\left(\vec{\mathrm{p}} - q_2'\vec{\mathrm{A}}\right) + \beta m_2' + q_2'\phi \\ &\cdots\cdots\cdots\cdots\cdots\cdots \end{aligned}\right\}. \quad (6)$$

In (6), all $\mathrm{H_i}$ have their own Hilbert space. Since the Hilbert spaces of $\{\mathrm{H_i}\}$ are generally different, there is no unique Hilbert space that satisfies the entire system. This means that any arbitrary state cannot be expressed as a linear combination of basis vectors. Therefore, the superposition principle does not hold in general.

However, when the interaction is very small, (3) can be approximated as an eigenvalue problem in standard quantum mechanics, i.e., Hilbert space analysis is possible.

If $\Delta p_\mu \ll p_\mu$, then

$$m' \simeq \frac{1}{3}\, m, \quad q' \simeq \left(1 - \frac{2}{3}\,\cos\Delta x^\mu p_\mu\right) q. \quad (7)$$

For example, in the case of the electrons of a hydrogen atom, $\langle T\rangle = -\langle V\rangle/2 \sim O(m\alpha^2)$ and $\Delta t = 1/m$ [4], so

$$\Delta x^\mu p_\mu = \Delta t\left(E - \frac{\vec{\mathrm{p}}^2}{m}\right) = \Delta t\,(V - T) \sim O(\alpha^2). \quad (8)$$

Therefore, $\cos\Delta x^\mu p_\mu \sim \cos\alpha^2 \simeq 1$. Also, since the cosine function is constant near 0, we can say that the mass and charge are constant in (7). This fact means that in the case where the interaction is very small, (3) can be said to have a unique Hilbert space. In other words, (3) can be interpreted as an eigenvalue problem of the standard quantum mechanics.

To summarize, the superposition principle of the standard quantum mechanics is established only when the interaction is very small, and in this case, the system can be analyzed using the Hilbert space. However, in general cases, the Hilbert space cannot be applied, and Equation (1) merely carries the meaning of the wave equation.

4 Double slit experiment

The double-slit experiment is a simple yet practical experiment that clearly reveals the strangeness of quantum mechanical reality. Since there are various theories for interpreting quantum mechanics, there may be various perspectives on the interpretation of the double-slit experiment, but here we will compare the standard quantum mechanical interpretation and the perspective of non-local waves in the perspective of discrete time.

When a single photon is fired toward a double slit, it passes through the slits and is detected at a single point on the screen. However, if photons are fired sequentially, an interference pattern forms on the screen. From the perspective of the standard quantum mechanical view of reality, this requires the existence of a state in which a single photon passes through both slits simultaneously. In other words, the superposition principle is necessary. If the states passing through each slit are ψ_1 and ψ_2, the interference state on the screen is $\psi_1 + \psi_2$, and its probability is given by the Born rule as $|\psi_1 + \psi_2|^2$. The view of reality underlying this explanation assumes that a photon is a localized particle-like entity with a phase.

Now, let us explain this in terms of non-local waves defined in discrete time. Non-local waves propagate and produce interference phenomena similarly to local waves, but

their wavefront collapses simultaneously at a single point on the screen. The wave passing through the double slits interferes on the screen, which is consistent with the behavior of local waves up to this point. However, a non-local wave behaves as if it causes the photoelectric effect as a single photon due to wave collapse from inelastic collisions with electrons of the atoms constituting the screen. The location of this reaction is determined by a probability proportional to the square of the interference amplitude. In other words, the Born rule still holds for non-local waves. In standard quantum mechanics, the square of the amplitude represents the probability of detecting a particle, whereas, in the non-local wave perspective, it represents the probability of wave collapse occurring at that point.

If the measuring device is placed at one of the double slits, the interference pattern disappears. From the conventional viewpoint, it is explained that interference does not occur because there is no state of passing through both slits at the same time. From the non-local wave viewpoint, the wave collapses due to an inelastic collision at the measuring device, and the wave proceeds again from that collapsed state, so it will have the same effect as a single slit.

The above discussion briefly examines the explanations of the double slit experiment from the two perspectives. While there is a clear difference in their views of reality, both perspectives explain the experimental results without significant issues.

5 Delayed choice experiment — wave-particle duality

The problem of wave-particle duality is a somewhat old problem in quantum mechanics, but it needs to be discussed because it raises doubts about physical reality. When discussing wave-particle duality, the concepts of wave and particle are somewhat traditional. It is somewhat different from the concept of reality used in the double-slit experiment.

There are various versions of the delayed choice experiment, but here we will first discuss the double-slit experiment proposed by Wheeler [6]. In this experiment, the light measuring device is a plate and photodetectors. The plate measures the interference pattern caused by the interference of light passing through both slits, and the photodetectors are placed facing the two slits to measure which slit the photon passes through. In other words, the former measures the wave nature of light, and the latter measures the particle nature of light. The point of this experiment is to figure out when light decides whether it behaves as a wave or a particle. It is assumed that its reality will be determined after passing through the double slits, but this thought experiment shows that this is contradictory. To see this, you have to choose the measuring device after the light passes through the double slits. Even then, if you choose the plate, you will still observe the interference pattern on the plate, and if you choose the photodetector, you will observe the particle impact.

As a simpler and more meaningful thought experiment, consider the split beam experiment introduced by Wheeler.

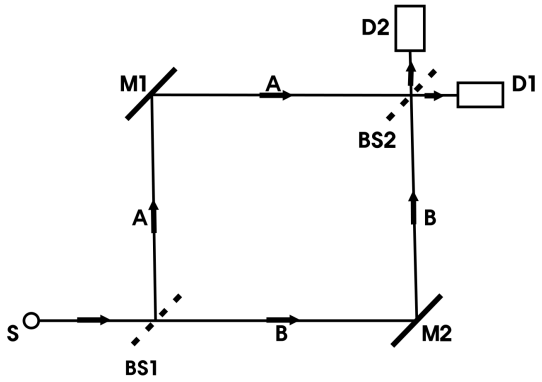

Fig. 1: Mach–Zehnder interferometer.

The experimental description of Fig. 1 is as follows

1. A single photon is emitted from a pulsating source of light S;
2. This photon reaches a semitransparent mirror BS1 and splits into two paths;
3. The first path goes to a perfectly reflective mirror M1, and the second path goes to a perfectly reflective mirror M2;
4. M1 and M2 reflect their respective beams so that they merge back together;
5. The two beams meet at a semitransparent mirror BS2, and photodetectors D1 and D2 are arranged to record the interference pattern between the two beams.

However, if the semitransparent mirror BS2 is removed during the experiment, the situation changes. Without BS2, the two beams do not merge, but proceed separately, and are directed to photodetectors D1 and D2, respectively. At this time, D1 detects the photon coming from the path through A, and D2 detects the photon coming from the path through B. In this case, the interference pattern disappears, and it is clear which path the photon took.

The key to this experiment is that after the photon passes through the semitransparent mirror BS1, the observer can choose whether to remove BS2 or leave it. If BS2 is left, an interference pattern is observed, and if it is removed, the path information is revealed.

The above thought experiments summarize that the reality of light is not determined while it is in motion, but is determined at the last moment of measurement. Wheeler says, "*No phenomenon is a phenomenon until it is an observed phenomenon*". Physical reality is not determined until it is observed, and the past is determined by observation. Reality is formed by the interaction with the observer.

Now, let us interpret these thought experiments from the perspective of non-local wave. In the discrete time perspec-

tive, it is assumed that the physical reality before measurement exists in the form of a non-local wave, and the simultaneous wave collapse caused by interaction possesses quantum properties.

First, in the double-slit experiment, choosing a plate or photodetectors as the measurement device, even if the choice is made after the light passes through the double slits, has no effect on the reality of the light as a non-local wave. A non-local wave simply causes wave collapse at the plate if a plate is present, or at the photodetector if a photodetector is present. As previously explained, wave collapse at the plate occurs with a probability proportional to the square of the interference wave's amplitude, resulting in an interference pattern. A non-local wave entering the photodetectors has an equal probability of wave collapse at each photodetector, but if wave collapse occurs at one photodetector, the collapse property of the non-local wave ensures that no observation occurs at the other detector. However, observing a wave collapse at one photodetector does not mean the light passed through a specific slit. The non-local wave always passes through both slits. Even if the photodetectors are sufficiently far from the double slits to neglect interference effects, if no collapse occurs in between, a measurement will occur at one of the photodetectors.

Next, let us consider the beam-splitter experiment. The non-local wave emitted from the light source is equally split into two paths at the partially transparent mirror BS1. The non-local waves traveling along each path meet at the partially transparent mirror BS2, where they interfere, causing a wave collapse at D1 due to constructive interference, resulting in observation. If BS2 is removed, the split light from each path reaches D1 and D2. In this case, the probability of wave collapse at each detector is 50%, so a photon is observed at either D1 or D2. Observing a photon at D1 or D2 does not mean the light traveled through a specific single path. The non-local wave passes through both paths. The fact that it is observed at only one detector is due to the collapse property of the non-local wave. The delayed choice of the measurement device made while the non-local wave travels through both paths has no effect on the physical reality of the non-local wave. The non-local wave simply undergoes wave collapse due to interaction at the measurement device.

It is indeed difficult to explain the delayed-choice experiment using the conventional concepts of waves or particles. These concepts cannot define the physical reality before observation. However, as pointed out in the previous paper, the conventional concepts of waves and particles are physical realities inferred from the macroscopic world [1]. The logic of the delayed-choice experiment, which suggests that these concepts cannot define the microscopic world before observation, is valid. However, interpreting this to mean that no determined physical reality independent of observation exists in the microscopic world is an excessive leap in logic. It is merely that the conventional concepts of waves and particles cannot define it. This paper proposes non-local waves as an alternative.

Local conservation of energy

The concept of local conservation of energy is one of the most important concepts in physics, encompassing both classical mechanics and quantum mechanics. However, this concept requires a rigorous definition when applied to the microscopic world. The wave-particle duality in the microscopic world and the concept of local conservation of energy can lead to contradictory situations.

The definitions of energy and momentum are established through interactions. These concepts may apply prior to interactions, but they can also be seen as emerging during interactions. In classical mechanics, they are always defined regardless of interactions, and the law of local conservation holds. However, in quantum mechanics, there is an issue.

Quantum mechanical reality possesses both wave and particle properties. Let us first consider the wave. Can a wave possess energy? Naturally, the energy of a photon is defined as $E = h\nu$. However, this is a concept associated with a particle. A wave spreads and propagates through space. If energy were defined for a wave, the energy of its local parts would need to be defined, which cannot explain the quantization of energy during interactions.* Furthermore, if momentum were defined for a wave, the concept of accelerated motion would need to be defined for the wave. A wave is a physical reality that propagates and interferes, not a concept that accelerates like a particle. Consequently, the concept of mass cannot be defined for a wave. Next, let us consider particle properties. A particle can naturally have mass defined. However, defining frequency or wavelength for a particle is not reasonable.

Synthesizing the above, energy and momentum cannot be defined for a wave, and frequency and wavelength cannot be defined for a particle. However, all these concepts are necessary to describe the microscopic world. The microscopic world exhibits wave-like properties at times and particle-like properties at others. However, these two properties never manifest simultaneously. This suggests that some form of transition occurs between wave-like and particle-like properties. Thus, the equation $E = h\nu$ can be interpreted as indicating that light, as a wave with frequency ν, transitions into a particle-like photon with energy $h\nu$. Here, the Planck constant can be understood as representing a kind of exchange ratio during this transition. Since this exchange ratio is constant, energy is consequently conserved. However, its meaning differs from the local energy conservation in classical mechanics.

The concept of transition between wave and particle discussed above is merely an inference derived from quantum

*In the quantum field theory, this issue is addressed by introducing the mathematical assumption of second quantization, but this is an entirely different approach.

mechanical phenomena and the definitions of wave and particle concepts. A model that aligns with this inference is the non-local wave. If the concept of energy conservation in the microscopic world is defined as above, the issue of local energy conservation arising from the instantaneous collapse of a local wave does not occur in the collapse of a non-local wave.

6 Interaction free measurement

Interaction-free measurements were first proposed in the Renninger negative-result experiment and developed into the Elitzur-Vaidman Bomb Tester [8]. This thought experiment vividly illustrates how our notions of physical reality significantly influence the understanding of phenomena. The components of this experiment are as follows. It uses the Mach-Zehnder Interferometer shown in Fig. 1 and applies the concept of physical reality from standard quantum mechanics. The bomb is placed in path B and explodes upon interaction with a photon. The bomb can be in a "live" (functional) or "dummy" (non-functional) state.

How the interferometer works:

1. The photon splits into two paths (A and B) at BS1;
2. Along each path, it passes through mirrors (M1, M2) and is recombined at BS2;
3. At BS2, the photon is designed to reach only a specific detector (D1 or D2) due to interference effects. For example, if the interferometer is well tuned, the photon will always reach D1 and never reach D2.

The key to this experiment is to obtain information about whether a bomb is on path B without having the bomb directly interact with the photons (i.e. explode).

(1) In the absence of a bomb

When a photon reaches BS1, the wave function splits into two paths, A and B. The photon travels along the two paths and rejoins at BS2. Due to the interference effect, the photon always reaches D1 and never reaches D2. This is because constructive interference occurs at D1.

(2) If there is a bomb (live bomb)

Let us assume that there is a functional bomb in path B. This bomb explodes with 100% probability if it absorbs a photon. When a photon passes through BS1, the wave function still splits into two paths. However, if the photon interacts with the bomb in path B, an explosion occurs, and it is not observed at the detectors. This case occurs with a 50% probability (the probability that the photon chooses path B).

Conversely, if the photon chooses path A (50% probability), it does not interact with the bomb. In this case, the wave function collapses to path A. The photon then travels along path A and reaches BS2. BS2 splits the photon again with a 50:50 probability, sending it to either D1 or D2. Thus, the photon reaches D1 with a 25% probability and D2 with a 25% probability.

(3) In the case of a bomb (dummy bomb)

The dummy bomb has no sensors in the path of the photon. Therefore, it does not interact with the photon and behaves the same as in the case without the bomb. The photon always reaches D1 and never goes to D2 due to interference effects.

The critical aspect of this experiment is the detection result at D2. If D2 clicks, it definitively indicates that the bomb is in a live state, yet the photon did not interact with the bomb at all during this process. This is because the photon took path A, so it had no opportunity to encounter the bomb. However, the presence of the bomb (in its live state) eliminates the wave function component in path B, disrupting the interference and creating the possibility for D2 to click. In other words, the mere existence of the bomb induces the collapse of the wave function, altering the interference pattern. This conclusion demonstrates that measurement does not necessarily require a physical interaction between the particle and the detector.

The above is the conventional interpretation of the Elitzur-Vaidman Bomb Tester. However, before reaching such a conclusion, we must consider the quantum mechanical reality assumed in this interpretation. The non-local wave hypothesis offers a completely different interpretation of this experiment. In conclusion, all measurements originate from interactions.

The non-local wave incident on BS1 is divided into two paths:

(1) If there is no bomb, the waves passing through each path interfere at BS2, and due to constructive interference, wave collapse occurs at D1, where the photon is observed;

(2) If there is a bomb, the probability that wave collapse will occur by reacting with the bomb in path B is 50% because the wave is divided into two paths. When wave collapse occurs, the wave traveling along path A disappears simultaneously and acts as a single photon in the bomb. In this case, photon cannot be observed in either D1 or D2.

So, what happens in the remaining 50% probability where collapse does not occur? The collapse of a non-local wave occurs when an energy change is induced by an inelastic collision [2]. If the wave incident on the bomb undergoes elastic collision, there is no energy change, and thus, the photoelectric effect caused by light does not occur at the bomb's sensor. Naturally, this case does not result in an explosion. If only path B existed without path A, the bomb's sensitivity is assumed to be 100%, meaning it would definitely explode. However, with path A present, only 50% of the wave passes through path B, so the probability of the bomb exploding is also 50%. This eliminates the need to redefine a new probability for the bomb's sensor to trigger an explosion. There-

fore, in the 50% probability where an explosion does not occur, 50% of the wave travels along path A, and the remaining 50% undergoes elastic scattering at the bomb. The 50% that travels along path A reaches BS2, where it is split into D1 and D2 with a 25% probability each, and wave collapse occurs at one of the detectors with a 25% probability. The 25% probability of wave collapse occurs because only 25% of the original wave reaches the detector. When a non-local wave collapses, all wavefronts collapse simultaneously at a single point. The location of the remaining 75% of the wave is irrelevant. Consequently, interactions always occur in quantum units.

(3) In the case of a dummy bomb, as discussed above, photons will be observed at D1 by constructive interference, just as in the case of no bomb.

The crucial point in the above discussion is that the photon observed at D2 with a 25% probability is not devoid of interaction with the bomb. The light that splits at BS1 and travels along path B undergoes an interaction with the bomb through elastic scattering. According to the conventional view of reality in standard quantum mechanics, it is interpreted as having no interaction, but from the perspective of non-local waves, an interaction is considered to have occurred.

7 Measurement problem

According to standard quantum mechanics, the state of any physical system defined in a Hilbert space can be represented as a superposition of basis states, and this state evolves deterministically according to the Schrödinger equation. However, measurement causes the system's state to collapse into a single basis state. This process occurs probabilistically according to the Born rule and is a non-unitary process that is not predicted by the Schrödinger equation. Yet, this measurement principle is empirically based, and its foundation remains unclear. Currently, various interpretations, from objective collapse theories to epistemological interpretations, attempt to explain it, but none are definitive.

In contrast, from the new perspective of non-local waves in discrete time, the superposition principle does not generally hold. The system's state cannot be represented as a linear combination of basis states in a unique Hilbert space. The state of a single-particle system, before interaction, is a uniquely determined non-local wave. When the wave collapses due to an interaction accompanied by an energy change, it becomes a Compton sphere with a determined mass and size. Therefore, from this perspective, the measurement problem itself does not arise.

As suggested in the previous paper, quantum waves do not exist in systems above the Planck mass [1]. Thus, discussing superposition for physical objects in the macroscopic world is meaningless. That is, Schrödinger's cat is not a controversial issue at all.

8 Conclusions

The title of this series of papers, "Interpretation of Quantum Mechanics", may seem somewhat inappropriate. While the various existing interpretations of quantum mechanics differ significantly in their perspectives, they share a common foundation: the superposition principle, one of the most fundamental axioms of standard quantum mechanics. However, in the discrete time perspective, the superposition principle generally does not hold, making many claims in these papers appear to fall outside the scope of quantum mechanics. Nevertheless, even though the superposition principle does not generally apply, it is approximately satisfied in systems with very small interactions, so this can be seen as an extension of standard quantum mechanics.

This paper argues that many problems in standard quantum mechanics stem from two main aspects. The first is the ontological assumption about physical reality. The way physical reality is perceived fundamentally alters the physical interpretation of phenomena and the direction of research.

The second issue is the superposition principle. This principle is the most important in quantum mechanics but also causes several problems. However, in the discrete time perspective, this principle is considered to hold only in specific cases in the microscopic world, so the measurement problem, as seen in standard quantum mechanics, does not exist.

Let us consider another example where these two aspects are prominently revealed. Recall the double-slit experiment discussed earlier. According to the conventional view of reality, a state exists where a particle passes through both slits simultaneously, necessitating consideration of a superposition state of gravity caused by the particle. This leads to the need for a theory of quantum gravity. The assumptions underlying this logic are the ontological assumption about matter before interaction — namely, that matter is a localized entity with particle-like properties — and the superposition principle. In other words, the notion is that matter before observation can exist in "this place" and "that place" simultaneously. However, as argued in this paper, if these two assumptions are incorrect, this notion does not hold, and consequently, the necessity for a quantum gravity theory is significantly reduced.

On the other hand, what about the non-local wave perspective? When a non-local wave passes through the double slits, it is a determined wave, and the concept of a superposition state is unnecessary. In the case of matter, when the non-local wave collapses to form a Compton sphere, the collapse position is probabilistically determined by the Born rule, and this sphere has a determined mass and size. Therefore, from this perspective, the concept of a superposition state of gravity does not apply.

Submitted on July 26, 2025

References

1. Noh Y. J. Interpretation of Quantum Mechanics in terms of Discrete Time II. *Progress in Physics*, 2024, v. 20, 21–23.

2. Noh Y. J. Interpretation of Quantum Mechanics in terms of Discrete Time I. *Progress in Physics*, 2023, v. 19, 109–114.
3. Noh Y. J. Lamb shift in Discrete Time. *Progress in Physics*, 2022, v. 18, 126–130.
4. Noh Y. J. Anomalous magnetic moment in Discrete Time. *Progress in Physics*, 2021, v. 17, 207–209.
5. Noh Y. J. Propagation of a particle in Discrete Time. *Progress in Physics*, 2020, v. 16, 116–122.
6. Wheeler J. A. The "past" and the "delayed-choice" double-slit experiment. *Mathematical Foundations of Quantum Theory*, edited by A. R. Marlow, Academic Press, New York, 1978, 9–48.
7. Dirac P. A. M. The Principles of Quantum Mechanics. Oxford University Press, 1958.
8. Elitzur A., Vaidman L. Quantum mechanical interaction-free measurements. *Foundations of Physics*, 1993, v.23, 987–997.
9. Hance J. R., Hossenfelder S. What does it take to solve the measurement problem? arXiv: quant-ph.2206.10445v3.

Observing Electric Currents in Space

Michael Clarage

Independent Researcher, Boston, MA, USA.
E-mail: michael.clarage@protonmail.com

To find evidence for electric currents in cosmic plasmas requires both that the currents be looked for, and that data be available to indicate their presence. This paper focuses on the second requirement, the available data, and how the flow of electric current in plasmas naturally will be difficult to observe from a distance. Coaxial current flow predicted and observed in plasmas is examined in some detail showing that even very large total current flows can give, when seen from a distance, very little signal. Examples are given from active galactic nuclei, planetary magnetospheres, and plasma ejections from moons. Suggestions are given for how to analyze existing astrophysical data and also for new measurements to be made that will show the presence of cosmic electric currents.

1 Introduction

In 1977, Hannes Alfven [1] wrote that at the galactic scale, electric currents of 10^{17}-10^{19} amperes would be natural. Forty years later measured estimates are of 10^{18} amperes in jets from active galactic nuclei [2, 3]. The accuracy of the 1977 prediction, so far in advance of observation, is a strong testament to Alfven and his colleagues, and an indication that more attention should be given to their work.

Kristian Birkeland is often credited with first describing cosmic electric currents in his 1908 model of electric currents flowing from the Sun to the Earth causing the aurora borealis [4]. For 60 years, Birkeland's theory of large-scale electrical connection was ignored in favor of the mathematical models of Sydney Chapman, where planets are electrically insulated from the Sun and solar wind.

The first in-situ measurements of cosmic-scaled electric currents were provided by Zmuda *et al* [5] with a single axis magnetometer on board the navigation satellite 1963–1938C. Today the presence of cosmic electric currents is acknowledged, but the debate remains if the electric fields and currents can be causal, or are merely a consequence of thermodynamic and ponderomotive processes.

Electric current flow in a coaxial configuration was first described in Oliver Heaviside's 1880 patent [6]. Attempted telegraph cables that sent current in only one direction required more energy and incurred substantial information loss compared to cables with a built-in design to accommodate a return current.

Coaxial current flow, now commonplace to the electrical engineer, is a new idea to many in the astronomical community. This paper will elaborate the morphology of electric current flow in low density plasmas, and present several examples observed in cosmic plasmas. The argument is advanced that coaxial current flow is to be expected in cosmic plasmas, though its presence will be difficult to observe remotely. The paper will conclude with suggested observations needed to advance this topic.

2 The magnitude of cosmic electric currents

When electric current flows through astronomical plasmas there must be an electric field that is causing the electric charges to move. The movement of charge will create a circular magnetic field which will constrict the flow of charges into a narrow line. Gravitational attraction will condense the mass of the plasma. The mass of the plasma will be dissipated and expanded by random thermal motions and by the total energy stored in the magnetic field. When all these forces are in a stable state, we set the energies that condense equal to the energies that expand.

Consider an electric current flowing along a tube through a cosmic plasma, the width of the tube is R_0 [7, see eq 2.52]. These expressions are in units of energy per unit length:

$$\frac{\mu_0}{8\pi} I^2(R_0) + \frac{1}{2} Gm^2 N^2(R_0) = \Delta W_{B_z} + \Delta W_k \,. \qquad (1)$$

The integrated linear current density out to radius R_0 is given by I; m is the mean particle mass averaged over electrons, ions, and neutral particles; N is the integrated linear particle number out to radius R_0; ΔW_{B_z} is the difference of magnetic field energy between the total energy inside the tube and that at the boundary of the tube; ΔW_k is the difference of kinetic energy between the total inside the tube and that at the boundary of the tube.

This formulation was proposed by Carlqvist in 1988 [8], showing the relative importance of the electromagnetic force, gravitational force, and thermal motions for any given cosmic plasma setting. Using this relation, Alfven and Carlqvist argue we should expect above the Earth currents on the order of 1.0–10.0 million amperes, which the Iridium satellite network has verified [9]. The relation (1) implies that sunspots and coronal loops should have currents on the order of 10^{11} amps.

Since no satellites yet fly through coronal loops, the magnitude of electric currents are inferred from magnetic fields which are inferred from the polarization of light coming from the regions. Such modelling shows electric currents on the

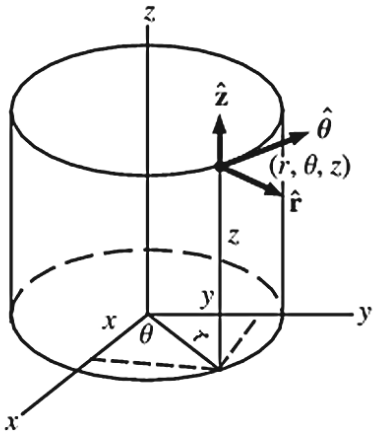

Fig. 1: Geometry for viewing an idealized current flow. Filament runs along the z-axis. Viewer is far away along the y-axis. The $x-z$ plane is the plane of the sky.

order of 10^{11} amperes. For the magnitude of electric current flowing through an entire star — which can be defined as the gravitating mass and the larger magnetic body of the heliosphere — the Carlqvist relation predicts currents on the order of 10^9 amps. This number has been confirmed for the electric current flowing into the Sun along the heliospheric current sheet [10]. The magnitude of the heliospheric current sheet is not directly measured, our existing satellite sensors cannot identify such a low current density, but is inferred from the magnetic fields that exist above and below the plane of the solar system. During the course of the 22-year solar cycle, electric current flows alternately inward/outward radially along the equator, and outward/inward from each pole, closing at the heliosphere, or in some models continuing to the interstellar medium.

Within the interstellar medium, the Carlqvist relation predicts electric currents on the order of 10^{14} amperes. The Planck, Herschel, and SOFIA telescopes have greatly increased the available data for the interstellar medium. Verschuur recently calculated currents of 10^{14} amperes in the A0 molecular cloud through neutral hydrogen emission measurements [11]. Stars form along filaments, the filaments extend for hundreds of light-years without broadening, filaments have a trunk-and-branch morphology, the filaments abruptly change direction at bright points, and different molecular species and energy states are segregated within the filaments. These are all features to be expected from electric currents in a plasma. The cause of these features is not primarily due to gravity.

At the galactic scale, Alfven proposed electric currents should be on the order of 10^{18} amps, from a balance of magnetic pressure, thermal expansion, gravity, and helical magnetic fields. Works by Kronberg and Lovelace [2] and Gabuzda [3] have deduced 10^{18} amperes of current flowing into and out of galaxies in a columnar form. The technique relies on measuring the polarization of light coming from the regions of these jets.

3 Measuring cosmic currents

3.1 Model

In 1950, Lundqvist proposed a force-free current flow in a plasma, meaning that the electric current flowing through the plasma feels no Lorentz force from ambient magnetic fields [12, 13]. This is a very special case, maybe never actually realized in nature, but if there is any truth in the model, it will give predictive power and new insights. In such a lowest energy configuration, the current and magnetic field must be flowing in the same direction. This arrangement of current and magnetic field seen in the force-free flow is much more complicated than a single wire carrying a current with the azimuthal magnetic field curling around.

In equation form, we write for the force-free condition

$$\mu\vec{J} = \alpha\vec{B}\,, \tag{2}$$

where μ and α are scalars which possibly depend upon position and plasma characteristics. $\vec{J}$ is the electric current density vector. $\vec{B}$ is the magnetic field vector. Scott [14] extended Lundqvist's model to values of radius large enough to see reversals of both magnetic and current directions. In the simplest case of current flow in cylindrical symmetry, the solutions to a force-free state are given by Bessel functions J_0 and J_1:

$$B_z(r) = B_z(0)\, J_0(\alpha r)\,, \tag{3}$$

$$B_\theta(r) = B_z(0)\, J_1(\alpha r)\,, \tag{4}$$

$$j_z(r) = \frac{\alpha B_z(0)}{\mu}\, J_0(\alpha r)\,, \tag{5}$$

$$j_\theta(r) = \frac{\alpha B_z(0)}{\mu}\, J_1(\alpha r)\,, \tag{6}$$

where (B_z, B_θ) and (j_z, j_θ) are the (z, θ) directions of the magnetic field and electric current density.

If the electric current is to be in a lowest energy configuration, the electric current and magnetic field flow *in the same direction*, and form a series of concentric shells, like multiple coaxial cables. With increasing R, the current and magnetic field, both pointing in the same direction, twist and eventually flow back in the opposite direction (see Fig 2). That a return current will be present in a lowest energy configuration harkens back to Heaviside's telegraph equation showing that a unidirectional current requires more energy and loses information.

With increasing total current, the direction of flow will again reverse itself, flowing in the direction of the center core. The exact physical conditions that dictate the number of reversals is not yet known. Some magnetic clouds at 1 AU show single reversals with 10^9 ampere currents [15]. Single reversals — simple coaxial — are seen in 10^{18} ampere galactic jets, while multiple reversals are seen in 10^{10} ampere polar currents on Earth. Hence magnitude of current is

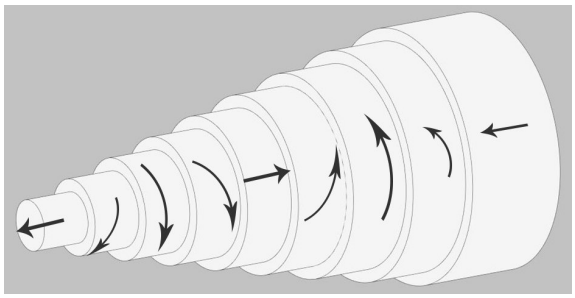

Fig. 2: Coaxial current flow in plasma with multiple reversals. Arrows represent the direction of the magnetic field and the electric current. The magnitudes are given by Eqs. (3)–(6).

not the only factor determining if current is unidirectional or if there is also a return current. The reverse current is also seen in particle-in-cell simulations, where a current injected into a plasma can only continue if a return current is created [7, p. 75].

3.2 Applying the model

Filaments are ubiquitous in the interstellar medium, see Fig. 3 for an example. The Herschel and Planck telescope projects are repositories for hundreds of such images. If electric currents were flowing through the filament, and were doing so according to the coaxial model, how would such a morphology be detected? We will look at several detection techniques: polarization changes due to magnetic fields, Doppler shifts due to relative motion, and segregation of atoms and molecules by ionization potential.

Consider a coaxial filament, with current flow along the z-direction, as shown in Fig 1. The viewer stands far away on the y-axis. The $x - z$ plane is the plane of the sky. We are looking "side-on" towards the filament. Interesting measurements such as changes in light polarization or Doppler shift will depend upon the integrated magnetic field along our line of sight.

We first consider a filament that has current flowing only in one direction, with no return current. Fig. 4 shows the numerically integrated projection of the components of the magnetic field along the y-axis, that is, the line of sight while looking through the filament. For any given point in the filament, the horizontal component of the magnetic field B_x will have a mirror point in front or behind the center which has the opposite horizontal component. Hence all B_x fields will tend to cancel. The B_y values have a different symmetry: fields pointing away on one side of the center will point towards us on the other side of the filament. This is shown in Fig. 4 where the B_y component changes sign on either side of the center. The B_z component will always flow in the positive direction, but drops off to zero at the outer boundary as the flow rotates to a purely azimuthal direction.

Next consider a current flow with a coaxial return flow,

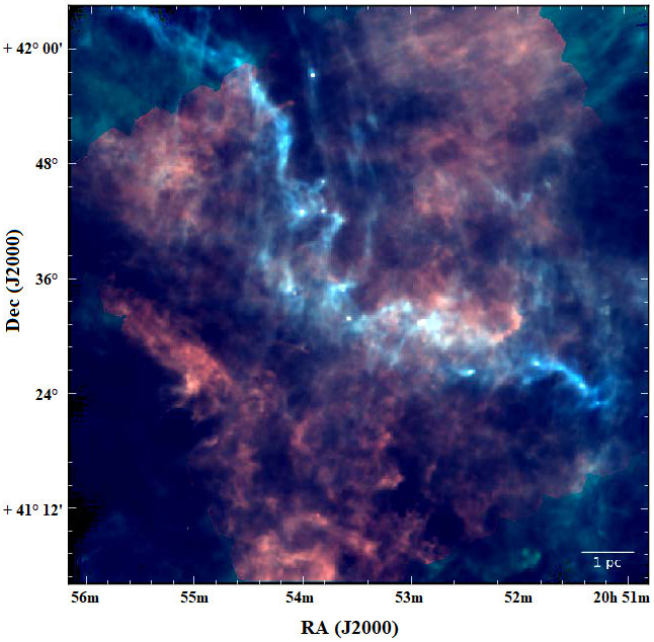

Fig. 3: Gas cloud G82.65-2.00 as seen by the Herschel telescope. RGB image, the colours correspond to Herschel channels at 160 nm (red), 250 nm (green), and 350 nm (blue). Credit ESA/Herschel/M. Juvela [16].

Fig. 5. The central current flow in the positive z-direction is surrounded by a return flow in the negative z-direction. The projection of the magnetic field components is shown. The same symmetries apply as in the previous case, but with more reversals. Figures 4 and 5 were solved on the same scale.

Applying this to telescope observations, low intensity current flow, Fig. 4, will have magnetic fields close to the filament that are parallel to the filament. Those parallel fields will decrease in intensity at the boundary of the filament. More intense current flow, Fig. 5, will show fields along the filament to reverse direction. Observations highlighting the B_y component will appear in Doppler shifts, since flowing charged particles will drag neutral particles. From the observer's point of view, the azimuthal flow around the filament axis will be moving away from the observer on one side of the filament and moving towards the observer on the other side. Look for opposite Doppler shifts on either side of the filament center.

Additional observations should focus on spatial segregation of atoms and molecules. The current flow in the force-free model is also very efficient at collecting ions into shells segregated by ionization potential, see [17]. Spectrographic data can be examined to look for atoms and molecules with low ionization potential collecting near the center of the filament and high ionization potential species concentrated on the periphery.

The ongoing debate as to whether magnetic fields are aligned with or perpendicular to interstellar molecular fila-

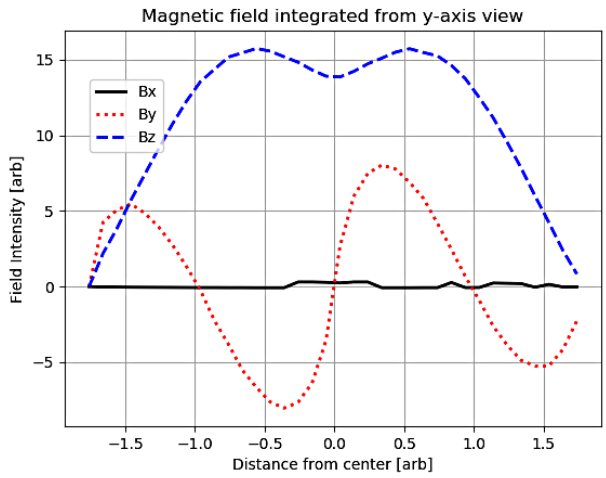

Fig. 4: The x, y, z-components of the integrated magnetic field seen from standing on the y-axis. There is no return current.

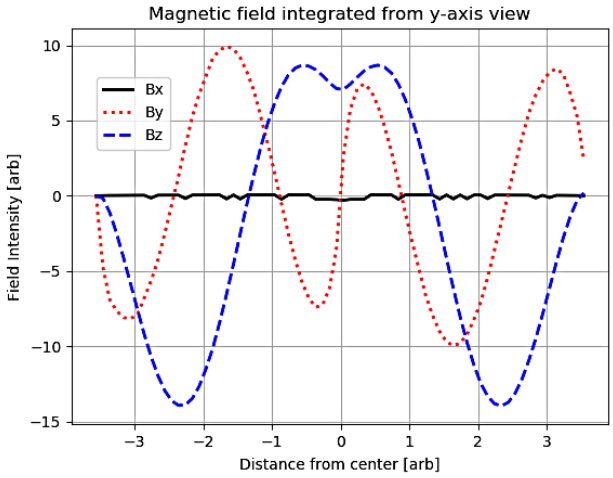

Fig. 5: Same as Fig. 4 but with a return current, that is, a simple coaxial current flow.

ments is rooted in the fact that both are true. The general form of cosmic currents and their associated magnetic fields will be coaxial, with directions constantly shifting from parallel, perpendicular, to anti-parallel, with the number of reversals dependent upon the setting.

As an example on a smaller scale, the polar electric currents on Earth form concentric shells, with the number of shells increasing with the current, see Fig. 6. Imagine trying to estimate the electric current flow in the Earth's aurora, but doing so by observing shifts in the polarization of light passing through the aurora.

When viewed from outside the Earth, the net change in polarization due to magnetic fields will be close to zero. Hence a current flow of billions of amperes can result in very little net change of polarization, and lead to the conclusion that no appreciable electric current exists in the Earth's aurora. It is arguable that planetary polar currents have underlying physics different from the model presented in this paper. If that is so, they still provide a clear example of how increased current causes additional counter-flowing shells and how remote sensing will greatly underestimate the actual current flowing.

The Cassini probe provides another example of how a large current flow can be seen as very small when viewed from a distance. When the Cassini probe flew through the plumes of Enceladus, the Langmuir probe, while flying through the plumes, measured charge densities indicating 10^7 amps of current flowing from the moon towards Saturn. But the magnetometer aboard, measuring from a distance, only measured a magnetic field that would be produced by 10^5 amps. Farrell *et al.* [18] suggest that an ion dust sheath forms around the central flow of electrons, which serves to shield the bulk of current flow. But is is unlikely that these ions are stationary, and more likely that they form a return current of a force-free Birkeland current.

Regardless, this represents a clear case where the electric current inferred from a distance is 1/100th that found through direct measurement. When viewed from the outside, magnetic fields produced by the main central flow will be partly cancelled by the outer sheath flowing in the opposite direction. Remote sensing tends to show only the net current, which in many cases will be much smaller than the number of charges flowing.

The methods described in this paper provide clear qualitative criteria for identifying force-free currents in cosmic plasmas. The more quantitative Carlqvist relation (1) can be used in a wide variety of cosmic settings. We suggest that the voluminous data of filaments in the interstellar medium available in Herschel, Planck, VLA, HI4PI, and other surveys be examined using the Carlqvist relation to map the morphology of electric currents in the galaxy. The method for such analysis, assuming unidirectional current flow, is presented clearly in [11]. Extending that method to the more general case of coaxial current flow will be the subject of a future paper.

The primary observational requirement, to apply the methods in this paper, is high resolution polarization and hyperspectral data cube with beam width easily resolving 0.1 pc distance, which is the average ISM filament width. Interstellar filaments in regions of high star formation are likely candidates, such as protostars in filaments in the Orion A molecular clouds: RA [42:00.00 to 34:00.00] Dec [-9:00:00 to -5:00:00].

4 Conclusions

Electric currents are ubiquitous in cosmic plasmas, having been observed at the planetary, solar, interstellar, and galactic levels. Considerations from basic plasma physics lead us to expect that in cosmic settings, electric current will flow in a coaxial form: a primary current flow will be matched by a surrounding return current. There may even be multiple

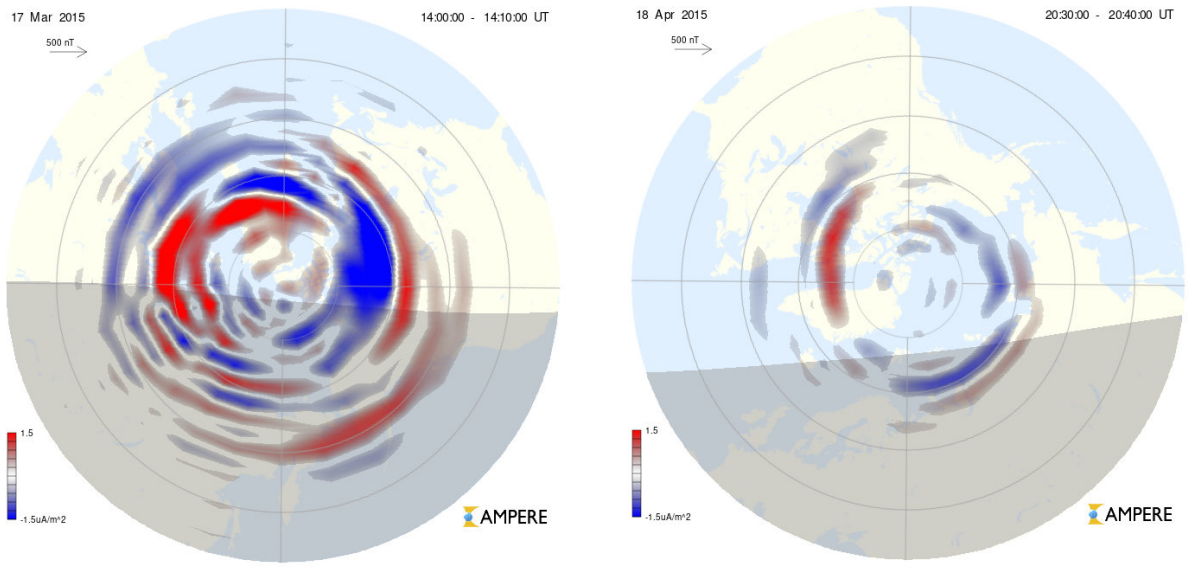

Fig. 6: Earth's polar electric currents. Left, from the "St Patrick's Day Storm" of 2015. Right, from one month later during quiet solar wind. Red/Blue represents current flowing away/towards the planet. During active solar wind there are multiple concentric reversals. From http://ampere.jhuapl.edu/ for the specified dates.

reversals of current, as in planetary polar currents.

When light passes through a coaxial current, the polarization changes will tend to cancel out, making it very difficult to determine the actual amount of current flowing. Likewise, any magnetic field measurements taken from outside such a coaxial current tube will greatly underestimate the current, since the reversing directions of current flow will cause a cancellation of magnetic field strength as seen from the outside. The ongoing debate as to whether magnetic fields are aligned with or perpendicular to interstellar molecular filaments is rooted in the fact that both are true.

Force-free current flow can also be identified from Doppler shift morphology and the segregation of atoms and molecules by ionization potential. The wealth of recent high resolution data in infrared, millimeter, and radio frequencies can be examined to distinguish different models for the flow of electric currents in cosmic plasmas.

5 Acknowledgements

This work was not funded. The author wishes to thank Don Scott for his work on coaxial plasma current flow, and Prof Richard Lovelace of Cornell University for his encouragement to write this article.

Submitted on May 8, 2025

References

1. Alfven H. and Carlqvist P. Interstellar clouds and the formation of stars. *Astrophysics and Space Science*, 1978, v. 55 (2), 487–509.
2. Kronberg P. and Lovelace R. Extragalactic circuits, transmission lines, and CR particle acceleration. arXiv: astro-ph/1412.3835.
3. Gabuzda D., Nagle M. and Roche N. The jets of AGN as giant coaxial cables. *Astrophysics and Astrophysics*, 2018, v. 612, A67.
4. Birkeland K. The Norwegian Aurora Polaris Expedition, 1902-03. Vol. I.: On the Cause of Magnetic Storms and the Origin of Terrestrial Magnetism. Christiania H Aschehoug and Co., 1913.
5. Zmuda A. J., Armstrong J. C. and Heuring F. T. Characteristics of transverse magnetic disturbances observed at 1100 kilometers in the auroral oval. *Journal of Geophysical Research*, 1970, v. 25 (75), 4757–4762.
6. Nahin P. Oliver Heaviside: The Life, Work, and Times of an Electrical Genius of the Victorian Age. Johns Hopkins University Press, Baltimore, MD, 2002.
7. Peratt A. Physics of the Plasma Universe. Springer Science+Business Media, New York, 2015.
8. Carlqvist P. Cosmic electric currents and the generalized Bennett relation. *Astrophysics and Space Science*, 1988, v. 144 (1–2), 73–84.
9. Coxon J. C., Milan S. E., Clausen L. B. N., Anderson B. J., and Korth H. The magnitudes of the regions 1 and 2 Birkeland currents observed by AMPERE and their role in solar wind-magnetosphere-ionosphere coupling. *Journal of Geophysical Research (Space Physics)*, 2014, v. 119 (12), 9804–9815.
10. Israelevich P. L., Gombosi T. I., Ershkovich A. I., Hansen K. C., Groth C. P. T., DeZeeuw D. L., and Powell, K. G. MHD simulation of the three-dimensional structure of the heliospheric current sheet. *Astronomy and Astrophysics*, 2001, v. 376, 288–291.
11. Verschuur G. High-resolution observations and the physics of high-velocity cloud A0. *Astrophysical Journal*, 2013, v. 766 (113), 1–17.
12. Lundquist S. Magneto-hydrostatic fields. *Ark. Fys.*, 1950, v. 2, 361–365.
13. Lundquist S. On the stability of magneto-hydrostatic fields. *Phys. Rev.*, 1951, v. 83, 307–311.
14. Scott D. Birkeland currents: A force-free field-aligned model. *Progress in Physics*, 2015, v. 11 (2), 167–179.
15. Lepping R. P., Berdichevsky D. B, Wu C. C., Szabo A., Narock T., Mariani F., Lazarus A. J., and Quivers A. J. A summary of WIND magnetic clouds for years 1995-2003: model-fitted parameters, associated errors and classifications. *Annales Geophysicae*, v. 24 (1), 215–245.

16. Saajasto M., Juvela M., *et al.* Correlation of gas dynamics and dust in the evolved filament G82.65-02.00. *Astronomy and Astrophysics*, v. 608, A21.

17. Marklund G. T. Plasma convection in force-free magnetic fields as a mechanism for chemical separation in cosmical plasmas. *Nature*, 1979, v. 277 (5695), 370–371.

18. Farrell W. M., Wahlund J. E., *et al.* Ion trapping by dust grains: Simulation applications to the Enceladus plume. *Journal of Geophysical Research* (*Planets*), 2017, v. 122 (4), 729–743.

New Four-Element Theory of Nature

T. X. Zhang

Department of Physics, Chemistry, and Mathematics, Alabama A&M University, 4900 Meridian Street, Huntsville, Alabama.
E-mail: tianxi.zhang@aamu.edu

This paper reviews the new four-element theory of nature, developed by the author for classically unifying all fundamental interactions of nature. Based on this theory, nature consists of only four fundamental elements, which are radiation (γ), mass (M), electric charge (Q), and color charge (C). Any known matter or particle observed in the universe and discovered in labs is a combination of one or more of the four fundamental elements, such as light is radiation only, neutron has mass only, Weyl fermion has electric charge only, gluon has color charge only, proton is a combination of mass and electric charge, and quark — a combination of mass, electric charge, and color charge. Fundamental interactions in nature are interactions among these fundamental elements. Radiation and mass are two forms of real energy as Einstein formulated. Electric and color charges are considered as two forms of imaginary energy. All the fundamental interactions are unified into a single interaction between complex energies. Interaction between real energies is the gravitational field force with three categories: mass-mass, mass-radiation, and radiation-radiation interactions. Interaction between imaginary energies is the gauge field force with also three categories: the electromagnetic force between electric charges, the strong force between color charges, and the weak force between electric and color charges. Interactions between real and imaginary energies are imaginary force, which have no observational support but may explain why charges are usually adhered on mass. As the weak force is an interaction between electric and color charges, it occurs effectively inside quark and causes quark excitation and decay. This leads the author to develop a new two-flavor multi-excitation quark model. This review gives details in various aspects and implications of the new four-element theory.

1 Introduction

Traditional four-element theory of nature, which was originated from Greek philosophy, posited that earth, air, fire, and water are the fundamental building blocks of all matter in nature. From the view of modern sciences, what are the fundamental elements of nature? It is well known that scientists have discovered one hundred and eighteen chemical elements in nature and from laboratory experiments, and listed them in the Mendeleev periodic table according to their chemical properties [1]. All the chemical elements can be also categorized into four groups: metals, nonmetals, metalloids, and noble gases or more specifically into eight groups by classifying metals into three types and separating the 113^{th} though 118^{th} elements as unknowns and the 7^{th}, 17^{th}, 35^{th}, 63^{rd}, and 85^{th} elements as halogens. Elements, compounds, and mixtures are three typical types of matter in chemistry. Solids, liquids, and gases are three fundamental states of matter in physics. Ionized gases are usually called plasmas, the fourth state of matter. Almost all the normal or ordinary matter in the universe is in the plasma state.

Particle physicists have discovered over three hundred particle in nature and from laboratory experiments, and usually categorized them into hadrons and leptons according to whether they participate in the strong interaction or not, or into fermions and bosons according to whether they have half-integer spins or not [2, 3]. Hadrons are composed of quarks with six flavors, usually being grouped into three generations or families along with the six leptons [4,5]. The six quarks are up (u), down (d), charm (c), strange (s), top (t), and bottom (b). The six leptons are electron (e), muon (μ), and tau (τ) and their corresponding neutrinos (ν_e, ν_μ, ν_τ). In the standard model of particle physics, the twelve spin-1/2 fermions (i.e., six quarks and six leptons) are building blocks of matter, the four spin-1 bosons (γ, g, W and Z) are gauge force carriers, and the spin-0 Higgs boson is the particle mass giver. Including gravitons (the carriers of gravitational force) and all antiparticles, physicists have found or predicted fifty-seven fundamental particles and listed them in the particle table [6].

Both chemical elements and physical elementary particles are not fundamental elements of nature because they still have common properties. Nuclei of different chemical elements consist of different numbers of nucleons (protons and neutrons). Nucleons are combinations of quarks. Quarks are combinations of mass, electric charge, and color charge. Leptons and weak bosons have mass and/or electric charge. Gamma bosons are massless radiation, and gluon bosons are color charges. Considering these facts, the author proposed and developed a new four-element theory of nature [7, 8]. From the fundamental elements of nature to reveal a new quantum world of quarks, the author has recently proposed and developed a new quark model called two-flavor multi-

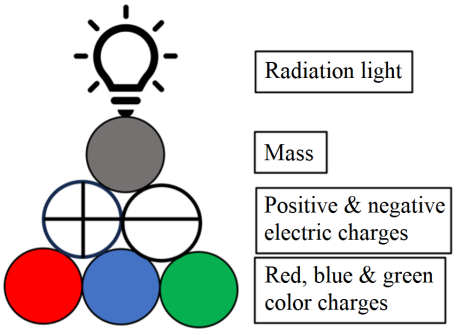

Fig. 1: Four fundamental elements of nature [7, 8]. They are radiation (γ), mass (M), electric charge (Q), and color charge (C). Radiation and mass are two forms of real energies. Electric and color charges are two forms of imaginary energies.

Table 1: Fundamental elements of nature. A particle is a combination of one or more of the four fundamental elements: mass (M), radiation (γ), electric charge (Q), and color charge (C).

Particles	γ	M	Q	C
Photon	✓			
Neutron		✓		
Weyl Fermion			✓	
Gluon				✓
Proton		✓	✓	
Massless Meson			✓	✓
Quark		✓	✓	✓

excitation quark model [9, 10], which has potential to solve both mysteries of why the present universe is significantly missing antimatter but fully filling with dark matter. This paper gives a sufficient review on this author's newly developed four-element theory of nature.

2 Fundamental elements of nature

The new four-element theory of nature suggests that nature consists of only four fundamental elements [7, 8], which are radiation (γ), mass (M), electric charge (Q), and color charges (C) as shown in Fig. 1. Any known matter or particle observed in nature or generated in labs is a combination of one or more of the four fundamental elements. For instances, as shown in Table 1, photon is radiation only; neutron has mass only; Weyl fermion has electric charge only; gluon has color charge only; proton is a combination of mass and electric charge; massless meson is a combination of electric and color charges; and quark is a combination of mass, electric charge, and color charge.

The author further categorized the four fundamental elements into two types of energies. Radiation and mass are two forms of real energy as Einstein formulated to be proportional to radiation frequency and mass, respectively, while electric and color charges are two forms of imaginary energy as the author formulated to be proportional to electric and color charges, respectively. Radiation energy is the energy of electromagnetic waves, propagating at the speed of light. Mass energy is the nuclear energy of an object or particle at rest or in motion. Real energy can do work in the real world and is measurable. A pure electric charge such as a Weyl fermion [11], as it is a form of imaginary energy, cannot be directly observed in nature, but its flow or current in semimetals has been detected [12]. A pure color charge such as a gluon [13], as it is a form of imaginary energy, cannot be directly observed in nature, but its behavior or existence has been detected in quark-gluon plasmas or jet events [14].

2.1 Mass — a form of real energy

Mass is a fundamental property of matter, which directly determines the gravitational interaction via Newton's law of gravitation [15]. Mass of an object is the quantity or amount of matter that the object contains. It is a measure of its inertia of motion in accordance with Newton's laws of motion. A body experiences an inertial force when it accelerates relative to the center of mass of the entire universe as Mach's principle indicates. In short, mass there affects inertia here. From Einstein's energy-mass expression (or Einstein's first law), mass is also understood as a form of real energy. A particle at rest with mass M has real energy given by [16]

$$E_M = Mc^2\,, \tag{1}$$

where c is the speed of light in the free space. A particle in motion, has mass to be the Lorentz factor of the rest mass, $\gamma_L M$, where $\gamma_L = (1-v^2/c^2)^{1/2}$ and v the speed of the particle. This real energy is always positive and directly measurable. It cannot be destroyed or created but can be converted from one form to another. In nuclear fission and fusion processes, a small amount of missing mass converts into a huge amount of nuclear energy. Newton's second law of motion states that acceleration of an object is proportional to the net force on the object and inversely proportional to the mass of the object.

2.2 Radiation — a form of real energy

Radiation γ refers to the electromagnetic radiation (or light), consisting of varying electric and magnetic fields, and can travel through vacuum by itself at the speed of light, about 300 million meters per second. Light looks like a ray as it travels straightly. Isaac Newton believed light to be particle because of its reflection and refraction. Thomas Young suggested light to be wave because of its interference and diffraction. James Clerk Maxwell recognized light to be electromagnetic waves because they travel at the same speed. In quantum physics, radiation is described as photons, which are massless quanta of real energy. The energy of a photon is given by [17]

$$E_\gamma = h\nu\,, \tag{2}$$

where h is the Planck constant and ν is the radiation frequency. Radiation quanta or photons of light explain blackbody radiation spectra [18], atomic emission and absorption spectra [19], Compton photon-electron scattering [20], and photoelectric effects [17]. Therefore, we can say in general that radiation is also a form of real energy and always positive. An atom, when it changes its state from energy E_2 to energy E_1, emits a photon with frequency or energy given or determined by the energy difference, $h\nu = E_2 - E_1$.

According to the increasing order of frequency or the decreasing order of wavelength, physicists usually categorize electromagnetic waves into radio wave, microwave, infrared, visible light, ultraviolet, X-ray, and gamma ray. Oscillations of electrons and nuclei including protons produce radio waves and microwaves; thermal motions of electrons and ions produce infrared light; Orbital or energy changes of electrons in atoms emit visible light and ultraviolet. Sudden stops of high-speed electrons on targets produce X-rays; and nuclear reactions and decays produce gamma rays.

Annihilations between particles and antiparticles including quarks and antiquarks produce pairs of gamma rays. In a pair production process, a gamma ray materializes into a pair of particle and antiparticle with non-zero masses. Annihilation and pair production indicate that the two forms of real energies (i.e. mass and radiation) can convert from one to another, so that they are not independent. If we define an equivalent mass for radiation to be $m_\gamma = h\nu/c^2$, we may consider nature to be composed of three fundamental elements: mass, electric charge, and color charge, rather than fours, so that reduce the four-element theory of nature to a three-element theory of nature.

2.3 Electric charge — a form of imaginary energy

Electric charge is another fundamental or intrinsic property of matter or some particles, which directly determines the electromagnetic interaction via Coulomb's law of electric force [27]. Electric charge has two varieties of either positive or negative. It appears or is observed always in association with mass to form positive or negative electrically charged particles with different masses such as electron and proton. The interaction between electric charges, however, is completely independent of their masses. Positive and negative charges can annihilate or cancel out each other and produce in pair with total electric charges conserved. Weyl fermion is a massless electron, which was predicted a century ago and recently measured in semimetals but not individually [11, 12].

A pure or individual electric charge should have its own meaning of physics. Zhang [7] first hypothesized or considered electric charge Q to be a form of imaginary energy. The amount of imaginary energy is defined to be proportional to the charge as

$$E_Q = \frac{Q}{\sqrt{G}}\, c^2 \,, \tag{3}$$

where G is the gravitational constant. This allows us to unify Newton's law of gravitation with Coulomb's law of electric force into a single expression between complex energy of electrically charged particles [7]. The imaginary energy has the same sign as the electric charge. Then, for an electrically charged particle, the total energy is

$$E = E_M + iE_Q = (1 + i\alpha)Mc^2 \,, \tag{4}$$

where i is the imaginary number and α is the charge-mass ratio of the particle, defined by

$$\alpha = \frac{E_Q}{E_M} = \frac{Q}{\sqrt{G}M} \,, \tag{5}$$

in the cgs electrostatic unit system. The complex conjugate of the energy of a charged particle such as an electron gives the energy of its corresponding antiparticle such as a positron [21, 22].

Including electric charge, Zhang [7] has modified Einstein's first law (1) into (4), in which electric charge is expressed as imaginary mass or energy. For an electrically charged particle, the absolute value of α is a big number. This implies that an electrically charged particle contains much more imaginary energy than its real energy (e.g., $\alpha = 10^{18}$ for proton and $\alpha = -2 \times 10^{21}$ for electron). A neutral particle such as a neutron, photon, or neutrino has only real energy. Weinberg [23] suggested that electric charges come from the fifth-dimensional space, which is a small and compact circle space in the Kaluza-Klein (KK) theory [24–26]. Zhang has developed a five-dimensional fully covariant KK-theory with a scalar field [28] and shown that electric charge can affect light (i.e., electric redshift) and gravity (i.e., gravitational shielding) [29, 30].

As the energy of an antiparticle is simply obtained by conjugating the energy of the corresponding particle, a particle and its antiparticle have same real energy but imaginary energy with opposite sign. In a particle-antiparticle annihilation process, their real energies completely convert into radiation photon energies and their imaginary energies annihilate or cancel out. Since there are no masses to adhere with, the electric charges come together due to the electric attraction and cancel out, or form a positive-negative electric charge pair $(+, -)$. In a particle-antiparticle pair production process, the radiation photon energies transfer to rest energies with a pair of imaginary energies, which combine with the rest energies to form a particle and an antiparticle.

Real energy is continuous, while imaginary energy is quantized. Each electric charge quantum e (which is also proton's charge) has imaginary energy about $iE_e = iec^2/\sqrt{G} \sim i10^{27}$ eV about 10^{18} times greater than proton's real energy ($\sim$ 931 MeV). This ratio is about the ratio between the radius of proton and the radius of the circular fifth dimensional space.

Table 2: Properties of six quarks: name, symbol, and electric charge.

Name	Symbol	Mass	Electric Charges
up	u	2.4 MeV	$2e/3$
down	d	4.8 MeV	$-e/3$
charm	c	1.27 GeV	$2e/3$
strange	s	104 MeV	$-e/3$
top	t	171.2 GeV	$2e/3$
bottom	b	4.2 GeV	$-e/3$

Table 3: Color combinations between red, blue, green and their anti-colors.

Color	r	b	g	$\bar{r}$	$\bar{b}$	$\bar{g}$
r	$2r$	$\bar{g}$	$\bar{b}$	0	$r_{\bar{b}}$	$r_{\bar{g}}$
b	$\bar{g}$	$2b$	$\bar{r}$	$b_{\bar{r}}$	0	$b_{\bar{g}}$
g	$\bar{b}$	$\bar{r}$	$2g$	$g_{\bar{r}}$	$g_{\bar{b}}$	0
$\bar{r}$	0	$\bar{r}_b$	$\bar{r}_g$	$2\bar{r}$	g	b
$\bar{b}$	$\bar{b}_r$	0	$\bar{b}_g$	g	$2\bar{b}$	r
$\bar{g}$	$\bar{g}_r$	$\bar{g}_b$	0	b	r	$2\bar{g}$

2.4 Color charge — a form of imaginary energy

Color charge C is a fundamental property of quarks and gluons [36], which has analogies with the notion of electric charge of particles. The basic properties (mass and electric charge) of the six quarks are shown in Table 2. There are three varieties of color charges: red, blue, and green. An antiquark's color is anti-red, anti-blue, or anti-green. Quarks and antiquarks also hold electric charges but the numbers of electric charges to be fractional such as $\pm e/3$ or $\pm 2e/3$. An elementary particle is usually composed of two or more quarks or antiquarks and colorless with electric charge to be a multiple of e or neutral. For instances, a proton is composed of two up quarks and one down quark (uud); a neutron is composed of one up quark and two down quarks (udd); a pion meson π^+ is composed of one up quark and one down antiquark ($u\bar{d}$); a charmed sigma Σ^{++} is composed by two up quarks and one charm quark (uuc); and so on.

Similar to electric charge Q, the author has hypothesized or considered the color charge C to be another form of imaginary energy. The amount of imaginary energy in a color charge can be defined by

$$E_C = \frac{C}{\sqrt{G}}\, c^2 \,, \tag{6}$$

in analogy to the electric charge for the grand unification of all fundamental interactions into a single interaction between complex energies [8]. Then, for a quark with mass M, electric charge Q, and color charge C, the total energy of the quark is

$$E = E_M + iE_Q + iE_C = (1 + i\alpha + i\beta)Mc^2 \,, \tag{7}$$

where β is defined by

$$\beta = \frac{E_C}{E_M} = \frac{C}{\sqrt{G}M} \,. \tag{8}$$

The total energy of an antiquark is obtained by conjugating the total energy of its corresponding quark. A quark and its antiquark have the same real energy and equal amount of imaginary energy, but their signs are opposite. The opposites of red, blue, and green charges are anti-red, anti-blue, and anti-green charges.

2.5 Color neutrality and quark confinement

In particle physics, color is a fundamental property of quarks and gluons, related to the strong forces. It is not the visible color but a type of charge. A neutral or white color (i.e., zero color charge) is formed when (1) a color and its anti-color combine $C + \bar{C} = 0$), (2) red, blue, and green colors combine ($r + b + g = 0$), and (3) anti-red, anti-blue, and anti-green colors combine ($\bar{r} + \bar{b} + \bar{g} = 0$). Table 3 lists the colors formed when any two colors combine, such as red and red colors combine to form double red color, red and blue combine to form anti-green color, red and green colors combine to form anti-blue color, red and anti-red colors combine to form white color, red and anti-blue colors combine to form red-anti-blue color, and red and anti-green colors combine to form red-anti-green color, and so on. Color neutrality refers to that only color-neutral particles can exist in isolation or independently. Color confinement refers to that particles with colors or anticolors cannot be observed alone.

2.6 Energy space of particles

Both real and imaginary energies are conserved, respectively. Being only positive, a real energy cannot be created or destroyed but can be converted from one to another. In electron-positron annihilation process, mass is converted into radiation. In the pair production of a gamma ray, radiation is converted or materialized into mass. Being both negative and positive for electric charges and both color and anti-color for color charges, an imaginary energy can be canceled out or neutralized. Net charges in an isolated system remain the same. As mentioned in subsection 2.1 above, the two forms of real energies (mass and radiation) can be converted from one to another and thus not independent. Here, we believe, the two forms of imaginary energies (electric charge and color charge) are independent, but they can interact via the weak force.

Fig. 2 constructs a three-dimensional (3D) energy space for particles based on the three independent fundamental elements or energy components (mass, electric charge, and color charge). Any particle has a position or can be located in this 3D energy space with coordinates (M, Q, C) with $M > 0$. For instances, a neutral particle such as neutron and neutrino, in-

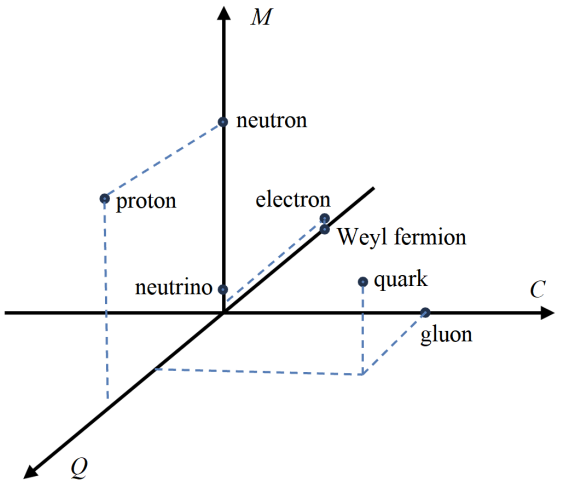

Fig. 2: 3D particle energy space. A neutral particle such as neutron or neutrino including radiation is found on the M-axis, a Weyl fermion is found on the Q-axis, a gluon is found on the C-axis, an electrically charged particle such as proton or electron is found in the $M-Q$ plane, and a quark is found in the 3D space with non-zero coordinates.

cluding radiation when it is equivalent to mass, has a coordinate $(M, 0, 0)$, located on the M-axis; an electrically charged particle such as proton and electron, located in the M-Q plane with a coordinate $(M, Q, 0)$; and a quark has a position in the 3D space with non-zero coordinates. Weyl fermions are on the Q-axis and gluons are on the C-axis. And so on for many other particles, including antiparticles, we can locate each of them with a unique set of coordinates in this 3D energy space of particles.

3 Fundamental interactions and unification

3.1 Fundamental interactions in nature

Fundamental interactions in nature are interactions among fundamental elements of nature. Among the four fundamental elements, there are ten fundamental interactions (Table 4). The three real forces ($\vec{F}_{MM}$, $\vec{F}_{\gamma\gamma}$, and $\vec{F}_{M\gamma}$) are interactions between two forms of real energies (γ and M) and belong to the gravitational forces. Another three real forces ($\vec{F}_{QQ}$, $\vec{F}_{QC}$, and $\vec{F}_{CC}$) are interactions between two forms of imaginary energies (Q and C) and belong to the gauge field forces, named, respectively, the electromagnetic, weak, and strong forces. The four imaginary forces ($i\vec{F}_{\gamma Q}$, $i\vec{F}_{\gamma C}$, $i\vec{F}_{MQ}$, and $i\vec{F}_{MC}$) are interactions between real and imaginary energies and have no direct measurements. Although these imaginary forces are not directly observational, they may play key roles in explaining why charges are always attached along with masses and absorb/emit radiation photons, and why gluons are adhesive. In physics, the fundamental interactions found in nature conventionally refer to the following fours: gravitational, electromagnetic, weak, and strong forces.

Table 4: Fundamental interactions among the four fundamental elements.

Name	γ	M	iQ	iC
γ	$\vec{F}_{\gamma\gamma}$	$\vec{F}_{\gamma M}$	$i\vec{F}_{\gamma Q}$	$i\vec{F}_{\gamma C}$
M		$\vec{F}_{MM}$	$i\vec{F}_{MQ}$	$i\vec{F}_{MC}$
iQ			$\vec{F}_{QQ}$	$\vec{F}_{QC}$
iC				$\vec{F}_{CC}$

3.2 Unification of all fundamental interactions

All the ten fundamental interactions among the four fundamental elements (two real energies and two imaginary energies) can be unified as a single interaction between complex energies as given by the following equation or shown by Fig. 3 [8]

$$\vec{F}_{E_1E_2} = -G\,\frac{E_1E_2}{c^4r^2}\,\hat{r}\,, \tag{9}$$

where G is the gravitational constant, E_1 and E_2 are complex energies of the two objects or particles, and r is the distance between the two objects or particles. This expression (9) may be called a generalized Newtonian gravitational law. Considering the complex energy of a general object or particle that has two real parts and two imaginary parts (i.e., $E_1 = E_{1\gamma}+E_{1M}+iE_{1Q}+iE_{1C}$ and $E_2 = E_{2\gamma}+E_{2M}+iE_{2Q}+iE_{2C}$), we can expand the single complex force into six real and four imaginary forces,

$$\begin{aligned}
\vec{F}_{E_1E_2} &= -G\,\frac{M_1M_2}{r^2}\,\hat{r} - G\,\frac{M_1h\nu_2 + M_2h\nu_1}{c^2r^2}\,\hat{r} - G\,\frac{h\nu_1h\nu_2}{c^4r^2}\,\hat{r} \\
&\quad + \frac{Q_1Q_2}{r^2}\,\hat{r} + \frac{Q_1C_2 + Q_2C_1}{r^2}\,\hat{r} + \frac{C_1C_2}{r^2}\,\hat{r} \\
&\quad - i\sqrt{G}\,\frac{h\nu_1Q_2 + h\nu_2Q_1}{c^2r^2}\,\hat{r} - i\sqrt{G}\,\frac{h\nu_1C_2 + h\nu_2C_1}{c^2r^2}\,\hat{r} \\
&\quad - i\sqrt{G}\,\frac{M_1Q_2 + M_2Q_1}{r^2}\,\hat{r} - i\sqrt{G}\,\frac{M_1C_2 + M_2C_1}{r^2}\,\hat{r} \\
&= \vec{F}_{MM} + \vec{F}_{\gamma M} + \vec{F}_{\gamma\gamma} + \vec{F}_{QQ} + \vec{F}_{QC} + \vec{F}_{CC} \\
&\quad + i\vec{F}_{\gamma Q} + i\vec{F}_{\gamma C} + i\vec{F}_{MQ} + i\vec{F}_{MC} \\
&= \vec{F}_{RR} + \vec{F}_{II} + i\vec{F}_{RI}\,.
\end{aligned} \tag{10}$$

Here, we have used (1–3) and (6) for the two real and two imaginary energy expressions. The symbol $\hat{r}$ is the unit vector along the direction of radial distance.

3.3 Gravitational force — interaction between real energy

The force $\vec{F}_{MM}$ represents Newton's law for the gravitational interaction between two masses. This force governs the orbital motion of astrophysical objects including the solar system. The force $\vec{F}_{\gamma M}$ is the gravitational interaction between mass and radiation and the force $\vec{F}_{\gamma\gamma}$ is the gravitational interaction between radiation and radiation. These three types

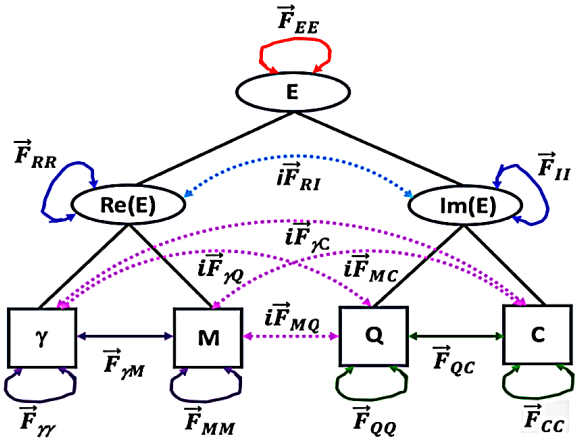

Fig. 3: Fundamental interactions among the four fundamental elements of nature: radiation, mass, electric charge and color charge. Mass and radiation are real energies, while electric and color charges are imaginary energies. Nature is a system of complex energy, and all the fundamental interactions of nature are classically unified into a single interaction between complex energies. There are six real and four imaginary interactions among the four fundamental elements.

of gravitational interactions are categorized as the interaction between real energies (Fig. 4a). Defining the radiation equivalent mass, we have a single gravitational force between masses.

When a photon of light travels relative to an object (e.g. the Sun) from $\vec{r}$ to $\vec{r}+d\vec{r}$, it changes its frequency from ν to $\nu+d\nu$. Calculating the work done by this mass-radiation force on a photon to be the energy change of the photon,

$$h d\nu = \vec{F}_{\gamma M} \cdot d\vec{r} = -G\frac{h\nu M}{c^2 r^2}\, dr\,, \tag{11}$$

the author derived Einstein's gravitational redshift without using the Schwarzschild solution of Einstein's general relativity [8, 37, 38]. First, dividing (11) by the photon energy $h\nu$ for variable separation and then integrating the radial distance from the object radius R to infinity ∞ and the photon frequency from the emission frequency ν_e to the observation frequency ν_o, we have

$$\int_{\nu_e}^{\nu_o} \frac{d\nu}{\nu} = -\int_R^{\infty} \frac{GM}{c^2 r^2}\, dr\,. \tag{12}$$

Completing this definite integration, we obtain

$$\ln\frac{\nu_o}{\nu_e} = -\frac{GM}{c^2 R}\,, \quad \text{or} \quad \frac{\nu_e}{\nu_o} = \exp\left(\frac{GM}{c^2 R}\right). \tag{13}$$

Then, the gravitational redshift can be derived as

$$Z_G = \frac{\lambda_o - \lambda_e}{\lambda_e} = \frac{\nu_e - \nu_o}{\nu_o} = \exp\left(\frac{GM}{c^2 R}\right) - 1\,. \tag{14}$$

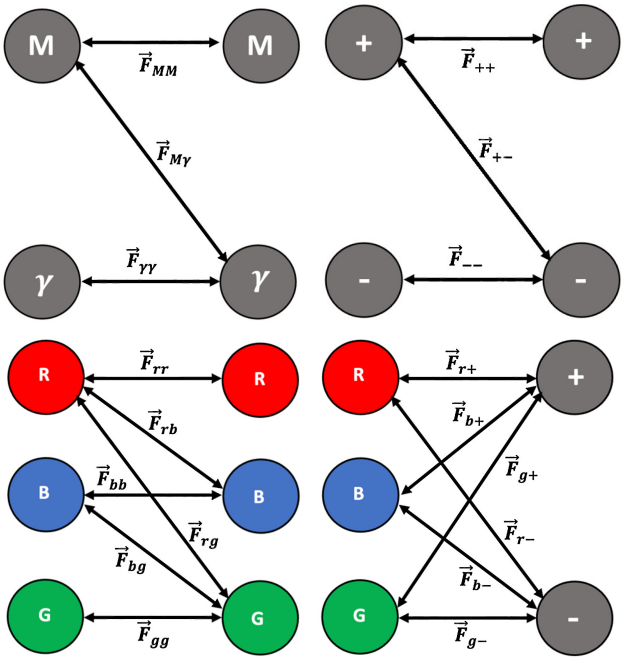

Fig. 4: (a) Top left panel shows the three types of gravitational interaction between real energies. They are the mass-mass, mass-radiation, and radiation-radiation interactions. (b) Top right panel shows the three types of electromagnetic force between electric charges. They are the positive-positive, positive-negative, and negative-negative interactions. (c) Bottom left panel shows the six types of strong interactions between color charges. They are the red-red, red-blue, red-green, blue-blue, blue-green, and green-green interactions. (d) Bottom right panel shows the six types of weak interactions between electric and color charges. They red-positive, red-negative, blue-positive, blue-negative, green-positive, and green-negative interactions.

In the weak field approximation, it reduces to

$$Z_G = \frac{GM}{c^2 R}\,. \tag{15}$$

Similarly, calculating the work done on a photon from an object by the radiation-radiation gravitation, the author further obtained a radiation redshift, which is proportional to the fourth power of temperature of the radiation. For the light from the Sun, the radiation redshift is about 10^{-13}, around seventh order lower in magnitude than the gravitational redshift [8], and hence negligible. For an extremely hot object, the radiation redshift will be significant and may be detectable.

3.4 Electromagnetic force — interaction between electric charges

The force $\vec{F}_{QQ}$ represents Coulomb's law for the electromagnetic interaction between two electric charges. This force governs the orbital motion of atomic electrons around nuclei. Electric charges have two varieties and thus three types of in-

Table 5: Gauge field interactions between different types of charges. These include the six strong field interactions between three types of color charges (coded as red), the six weak field interactions between three types of color charges and two types of electric charges (coded as blue), and the three types of electromagnetic field interactions between two types of electric charges (coded as green).

Charge	r	b	g	$+$	$-$
r	$\vec{F}_{rr}$	$\vec{F}_{rb}$	$\vec{F}_{rg}$	$\vec{F}_{r+}$	$\vec{F}_{r-}$
b		$\vec{F}_{bb}$	$\vec{F}_{bg}$	$\vec{F}_{b+}$	$\vec{F}_{b-}$
g			$\vec{F}_{gg}$	$\vec{F}_{g+}$	$\vec{F}_{g-}$
$+$				$\vec{F}_{++}$	$\vec{F}_{+-}$
$-$					$\vec{F}_{--}$

teractions (Fig. 4b, see also Table 5):

1) repelling between positive electric charges $\vec{F}_{++}$,
2) repelling between negative electric charges $\vec{F}_{--}$, and
3) attracting between positive and negative electric charges $\vec{F}_{+-}$.

Like charges repel one another and unlike charges attract one another. In the standard model of particle physics, the electromagnetic force between electric charges is described by the group $U(1)$.

3.5 Strong Force — interaction between color charges

The force $\vec{F}_{CC}$ is the strong interaction between color charges. Color charges have three varieties: red, blue, and green and thus have six types of interactions (Fig. 4c, see also Table 5):

1) the red-red interaction $\vec{F}_{rr}$,
2) the blue-blue interaction $\vec{F}_{bb}$,
3) the green-green interaction $\vec{F}_{gg}$,
4) the red-blue interaction $\vec{F}_{rb}$,
5) the red-green interaction $\vec{F}_{rg}$, and
6) the blue-green interaction $\vec{F}_{bg}$.

Fig. 4c shows these six types of color interactions or strong forces. With anticolors, there are 21 types of strong force between color charges. In the standard model of particle physics, the strong forces between color charges are described by the group SU(3).

The strong interaction is the only one that can change color of quarks in a hadron particle. A typical strong interaction is the proton-neutron scattering. This is an interaction between the color charge of one up quark in proton and the color charge of one down quark in neutron via exchanging a π^+-meson between the proton and neutron. In other words, during this proton-neutron scattering an up quark in the proton changes into a down quark by emitting a π^+, meanwhile a down quark in the neutron changes into an up quark by absorbing the π^+. Another typical strong interaction is delta decay, $\Delta^0 \to p + \pi^-$. This is an interaction between the color charge of one down quark and the color charges of the other two quarks. In this interaction, a down quark emits a π^- and then becomes an up quark, $d \to u + \pi^-$.

It should be noted here that the strong force carriers between nucleons (not quarks) are the pion mesons ($\pi^\pm$, π^0), which are the lightest hadrons, composed of one first-generation quark and one first-generation antiquark, and bind nucleons to form nuclei [33]. Gluons are the particles that mediate the strong forces that bind quarks together to form hadrons including nucleons [34]. Including antiparticles and gravitons (or gravitational force carriers), we have more fundamental particles [35]. We may categorize the strong force into two categories: (1) the nuclear force between nucleons to bind nucleons to form a nucleus and (2) the color charge interaction or force between quarks to bind quarks into hadrons.

3.6 Weak force — interaction between electric charge and color charge

The force $\vec{F}_{QC}$ is the weak interaction between electric and color charges. Considering electric charges with two varieties and color charges with three varieties, we have also six types of weak interactions (Fig. 4d, see also Table 5):

1) the positive-red interaction $\vec{F}_{+r}$,
2) the positive-blue interaction $\vec{F}_{+b}$,
3) the positive-green interaction $\vec{F}_{+g}$,
4) the negative-red interaction $\vec{F}_{-r}$,
5) the negative-blue interaction $\vec{F}_{-b}$, and
6) the negative-green interaction $\vec{F}_{-g}$.

With anticolors, there are 12 types of weak between electric and color charges. In the standard model of particle physics, the weak forces are described by the group SU(2) and carried by the W and Z bosons. The weak interaction is the only one that can change flavors of quarks in a hadron particle, which causes atoms to change from one element to another. A typical weak interaction occurs when neutron decays into proton with emissions of an electron and an electron-type antineutrino. In this process, a down quark in the neutron changes into an up quark by emitting a W-boson, which lives about 10^{-25} seconds and then breaks into a high-energy electron and an electron-type antineutrino.

3.7 Interaction between two electrically charged particles

The interaction between two electrically charged particles such as the interaction between two protons in a nucleus or the interaction between proton and electron in a hydrogen atom is given by

$$\begin{aligned}\vec{F}_{E_1E_2} &= -G\,\frac{(E_{1M}+iE_{1Q})(E_{2M}+iE_{2Q})}{c^4r^2}\,\hat{r}\\ &= -G\,\frac{M_1M_2}{r^2}\,\hat{r} + \frac{Q_1Q_2}{r^2}\,\hat{r} - i\sqrt{G}\,\frac{M_1Q_2+M_2Q_1}{r^2}\,\hat{r}\\ &= \vec{F}_{MM} + \vec{F}_{QQ} + i\vec{F}_{MQ}\,,\end{aligned} \tag{16}$$

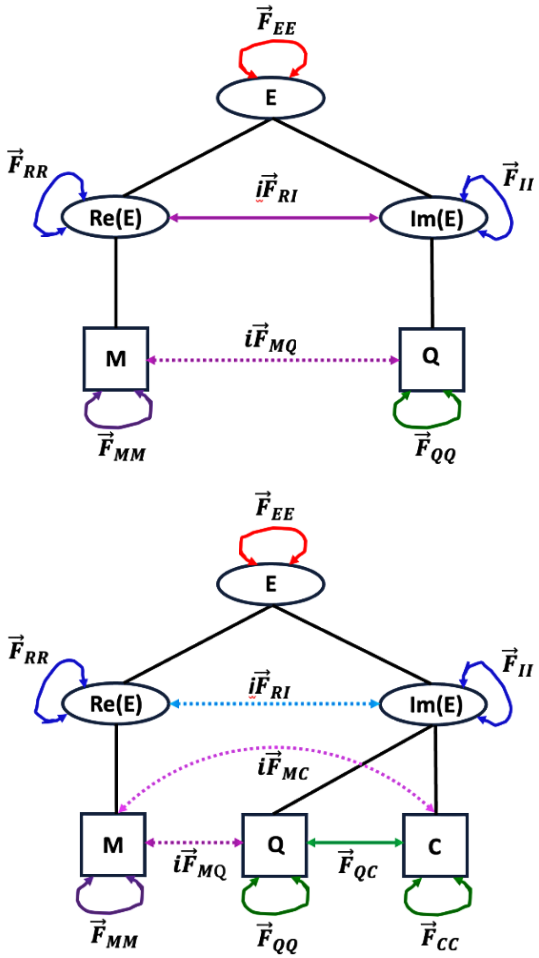

Fig. 5: (a) Top panel shows interaction between two electrically charged particles. It splits into three fundamental interactions: (1) a real force between masses $\vec{F}_{MM}$, the gravitational force governed by Newton's gravitational law, (2) a real force between electric charges $\vec{F}_{QQ}$, the electromagnetic force governed by Coulomb's law, and (3) an imaginary force between mass and electric charges $i\vec{F}_{MQ}$, which plays the role in sticking and adhering the electric charge on the mass to form electrically charged particles. (b) Bottom panel shows interaction between two quarks. It splits into six fundamental forces: (1) a real force between masses (gravitational) $\vec{F}_{MM}$, (2) a real force between electric charges (electromagnetic) $\vec{F}_{QQ}$, (3) a real force between color charges (strong) $\vec{F}_{CC}$, (4) a real force between electric and color charges (weak) $\vec{F}_{QC}$, (5) an imaginary force between mass and electric charge $i\vec{F}_{MQ}$, and (6) an imaginary force between mass and color charge $i\vec{F}_{MC}$.

or shown in Fig. 5a. It is split into two real forces and one imaginary force. The two real forces are $\vec{F}_{MM}$ and $\vec{F}_{QQ}$, governed by Newton's law of gravitation and Coulomb's law of electromagnetism, respectively. The one imaginary force is $i\vec{F}_{QC}$, which can occur inside of a particle to glue its electric charge on its mass or between two particles.

3.8 Interaction between two quarks

The interaction between two quarks in a hadron or in a quark-gluon plasma is given by

$$\begin{aligned}\vec{F}_{E_1E_2} &= -G\frac{(E_{1M}+iE_{1Q}+iE_{1C})(E_{2M}+iE_{2Q}+iE_{2C})}{c^4r^2}\hat{r}\\ &= -G\frac{M_1M_2}{r^2}\hat{r}+\frac{Q_1Q_2}{r^2}\hat{r}+\frac{Q_1C_2+Q_2C_1}{r^2}\hat{r}+\frac{C_1C_2}{r^2}\hat{r}\\ &\quad -i\sqrt{G}\frac{M_1Q_2+M_2Q_1}{r^2}\hat{r}--i\sqrt{G}\frac{M_1C_2+M_2C_1}{r^2}\hat{r}\\ &= \vec{F}_{MM}+\vec{F}_{QQ}+\vec{F}_{QC}+\vec{F}_{CC}+i\vec{F}_{MQ}+i\vec{F}_{MC}\,. \end{aligned} \tag{17}$$

or shown in Fig. 5b. It is split into four real and two imaginary forces. The four real forces are $\vec{F}_{MM}$, $\vec{F}_{QQ}$, $\vec{F}_{QC}$ and $\vec{F}_{CC}$, called by the gravitational, electromagnetic, weak and strong interactions, respectively. The two imaginary forces are $i\vec{F}_{MQ}$ and $i\vec{F}_{MC}$, gluing electric and color charges on mass.

Considering the strong interaction to be asymptotically free within a typical hadron [39], we can replace the color charge by

$$C \longrightarrow \frac{r}{r_0}C\,, \tag{18}$$

where r is the radial distance and $r_0 \sim 10^{-15}$ m is the radius of the typical hadron. This assumption represents that color charge becomes less colorful if it is closer to each other, i.e., asymptotically colorless. Then, the strong interaction between color charges of two quarks can be rewritten by

$$\vec{F}_{C_1C_2} = \frac{C_1C_2}{r_0^2}\hat{r}\,, \tag{19}$$

which is independent of the radial distance and consistent with measurements, and the weak force between electric charge of one quark and color charge of another quark becomes

$$\vec{F}_{Q_1C_2} = \frac{Q_1C_2}{r_0r}\hat{r}\,, \tag{20}$$

which is inversely proportional to the distance and consistent with measurements. The electromagnetic force between electric charges of two quarks is given by

$$\vec{F}_{Q_1Q_2} = \frac{Q_1Q_2}{r^2}\hat{r}\,. \tag{21}$$

Within a typical hadron (i.e., $r \sim r_0$) such as a proton or a neutron, the strong force can be 100 times stronger than the electromagnetic force in strength. This leads to the color-electric charge ratio of a quark to be $C/Q \sim 10$. The ratio between strong force and weak force will be about $\sim rC/(r_0Q)$. Since the weak force between electric charge and color charge has a shorter range of interaction ($r \sim 10^{-18}$ m or $r/r_0 \sim 10^{-3}$) such as within a typical quark, we have that the weak force between electric and color charge within a typical quark can be 100 times greater than the strong force between color charges of two quarks within a typical hadron. Therefore, the weak force that occurs inside a quark and causes the quark decay is not actually weak.

4 Discussions and conclusions

The new four-element theory suggests the weak force to be an interaction between electric and color charges, in analogy to the electromagnetic force to be an interaction between electric charges and the strong force to be an interaction between color charges. It occurs effectively inside a quark between its electric and color charges, so that is responsible for the excitation and decay of quarks. Considering an atom to be composed of a nucleus and electrons, a nucleus to be composed of nucleons, and a nucleon to be composed of quarks, we see radioactive decay of atoms to result from the decay of quarks that are triggered by the weak interaction between the quark's electric and color charges. This new scenario of weak interaction beyond the standard model of particle physics has important implications to the quark model, particle physics, and cosmology. Based on the new four-element theory of nature, we have developed a new quark model called two-flavor multi-excitation quark model [9, 40].

The new four-element theory of nature addresses only the ordinary matter of the universe. Based on the big bang standard model of cosmology, our universe dominates by dark matter and dark energy over 95%. The ordinary matter only takes 5%. The possible candidates of dark matter are weakly interacting massive particles (WIMPs), axions, sterile neutrinos, and primordial black holes. For the dark energy, the most favored explanation is the cosmological constant. The author proposed and developed a black hole model of the universe, which does not need dark energy [41–44]. On the other hand, the reason why distant supernovae appear dimmer than expected may be due to the redshift-luminosity relation that is conventionally applied is only an approximate expression for nearby objects [45]. If the spacetime is dynamic, our universe does not need to be accelerating and even expanding [46, 47].

As consequences of this review work, we have comprehensively reviewed the new four-element theory of nature, that was proposed and developed previously by the author to classically unify all fundamental interactions into a single interaction between complex energies. The new four-element theory of nature suggests that nature consists of four fundamental elements, which are radiation, mass, electric charge, and color charge. Any known matter or particle observed in nature or discovered in labs is a combination of one or more of the four fundamental elements. Fundamental interactions in nature are interactions among these fundamental elements. Radiation and mass are two forms of real energy. Electric and color charges are two forms of imaginary energy. All fundamental interactions are unified into a single interaction between complex energies. Interactions between real energies are gravitational field forces with three categories: mass-mass, mass-radiation, and radiation-radiation interactions. Interactions between imaginary energies are gauge field forces with also three categories: electric-electric charge (or electromagnetic), electric-color charge (or weak), and color-color charge (or strong) interactions. Interactions between real and imaginary energies are imaginary forces, which do not have observational support but may explain why electric and color charges are usually adhered on mass, rather than independently exist. The significant result obtained from the new four-element theory of nature such that the weak force is an interaction between electric and color charges would have essential implications to the quark and particle theories beyond the standard model as well as cosmology.

Acknowledgements

The work is supported by NSF HBCU-UP Research Initiation Award (#2400021). The author also acknowledges the support from the IBM-HBCU Quantum Center.

Received on August 28, 2025

References

1. Robinson A. E. Mendeleev's Periodic Table, Origins: Current Events in Historical Perspective. origins.osu.edu, 2019.
2. Machtmann O. Elementary Particle Physics: Concepts and Phenomena. Springer-Verlag, New York, 2012.
3. Martin B. R. and Shaw G. Particle Physics, 4th Edition. Wiley, 2017.
4. Hendry A. W. and Lichengburd D. B. The quark model. *Reports on Progress in Physics*, 1978, v. 41, 1707–1780.
5. Harari H. Composite models for quarks and leptons. *Physics Reports*, 1984, v. 104, 159–179.
6. Patrignani C. *et al*. (Particle Data Group) Review of particle physics. *Chinese Physics C*, 2016, v. 40, 100001.
7. Zhang T. X. Electric charge as a form of imaginary energy. *Progress in Physics*, 2008, v. 2, 79–83.
8. Zhang T. X. Fundamental elements and interactions of nature: A classical unification theory. *Progress in Physics*, 2010, v. 2, 36–42.
9. Zhang T. X. Four-element theory of nature and two-flavor multi-excitation model of quarks. American Physical Society (APS) Global Submit Conference, New Perspectives Session, Oral Presentation, Abstract #3, Anaheim, California, March 16–21, 2025.
10. Zhang T. X. New insights to the weak interaction and quark model. Quark Matter 2023 Conference, Houston, September 3–8, 2023.
11. Weyl H. Elektron und Gravitation I. *Z. Phys.*, 1929, v. 56, 330–352.
12. Xu S. Y. *et al*. Discovery of a Weyl fermion semimetal and topological Fermi arcs. *Science*, 2016, v. 349, 613–617.
13. Gell-Mann M. Symmetries of baryons and mesons. *Physical Review*, 1962, v. 125, 1067–1084.
14. McLerran L. The physics of the quark-gluon plasma. *Review of Modern Physics*, 1986, v. 58, 1021–1064.
15. Newton I. Mathematical principles of natural philosophy, Book III. 1687.
16. Einstein A. Ist die Trägheit eines Körpers von seinem Energieinhalt abhängig? *Ann. Phys.*, 1905, v. 323, 639–641.
17. Einstein A. Übereinendie Erzeugungund Verwandlung des Lichtes betreffenden heuristischen Gesichtspunkt. *Ann. Phys.*, 1905, v. 322, 132–148.
18. Planck M. The Theory of Heat Radiation, 2nd ed. Translated by Masius M., P. Blackiston's Son & Co., 1914.
19. Bohr N. On the constitution of atoms and molecules. *The London, Edinburgh, and Dublin Philosophical Magazine and Journal of Science*. 1913, v. 26, 1–25.

20. Compton A. H. A quantum theory of the scattering of X-rays by light elements. *Physical Review*, 1923, v. 21, 483–502.
21. Dirac P. A. M. The quantum theory of the electron. *Proceedings of the Royal Society of London A*. 1926, v. 117, 610–624.
22. Anderson C. D. The positive electron. *Physics Review*, 1933, v. 43, 491–498.
23. Weinberg S. Charges from extra dimensions. *Physics Letters B*, 1983, v. 125, 265–269.
24. Kaluza T. On the unification problem in physics. arXiv: physics.hist-ph/1803.08616.
25. Klein O. Quantum theory and five dimensional theory of relativity. *Z. Phys.*, 1926, v. 37, 895–906.
26. Klein O. The atomicity of electricity as a quantum theory law. *Nature*, 1926, v. 118, 516–520.
27. Coulomb C. Theoretical research and experimentation on torsion and the elasticity of metal wire. *Ann. Phys.*, 1802, v. 11, 254–257.
28. Zhang T. X. The 5D fully-covariant theory of gravitation and its astrophysical applications. *Galaxies*, 2015, v. 3, 18–51.
29. Zhang T. X. Electric redshift and quasars in physics. *The Astrophysical Journal Letters*, 2006, v. 636, 61–64.
30. Zhang T. X. Gravitational field shielding and supernova explosions. *The Astrophysical Journal Letters*, 2010, 725, L117–L120.
31. Gaillard M. K., Grannis P. D. and Sciulli F. J. The standard model of particle physics. *Reviews of Modern Physics*, 1999, v. 71, S96–S111.
32. Higgs P. W. Broken Symmetries and the Masses of Gauge Bosons. *Physical Review Letters*, 1964, v. 13, 508–509.
33. Gibbs W. R. and Gibson B. F. Pion-nucleus interactions. *Annual Review of Nuclear and Particle Science*, 1987, v. 37, 411–461.
34. Creutz M. Quarks, Gluons, and Lattices. Cambridge University Press, Cambridge, 1983.
35. Dyson F. Is a graviton detectable? *International Journal of Modern Physics A*, 2013, v. 28, 1330041 (14 pages).
36. Veltman M. Facts and mysteries in elementary particle physics. World Scientific, 2003.
37. Einstein A. Die Grundlage der Allgemeinen Relativitats theorie. *Ann. Phys.*, 1916, v. 354, 769–822.
38. Schwarzschild K. The Gravitational Field of a Mass Point According to Einstein's Theory. *Math. Phys.*, 1916, v. 1, 189–196.
39. Gross D. J. and Wilczek F. Asymptotically free gauge theories I. *Physical Review D*, 1973, v. 8, 3633–3652.
40. Zhang T. X. Two-Flavor Multi-Excitation Model of Quarks. *Journal of Modern Physics*, 2025, v. 16, 1243–1268.
41. Zhang T. X. A new cosmological model: black hole universe. *Progress in Physics*, 2009, v. 3, 3–11.
42. Zhang T. X. Cosmic microwave background radiation of black hole universe. *Astrophysics and Apace Science*, 2010, v. 330, 157–165.
43. Zhang T. X. and Frederick C. Acceleration of black holes. *Astrophysics and Space Science*, 2014, v. 349, 567–573.
44. Zhang T. X. The principles and Laws of Black Hole Universe. *Journal of Modern Physics*, 2018, v. 9, 1838–1865.
45. Zhang T. X. Key to the mystery of dark energy: Corrected relationship between luminosity distance and redshift. *Progress in Physics*, 2013, v. 3, 33–39.
46. Zhang T. X. Mach's Principle to Hubble's law and light relativity. *Journal of Modern Physics*, 2018, v. 9, 433–442.
47. Zhang T. X. Dynamic spacetime: Key to the mysteries of dark matter and dark energy. *Journal of Modern Physics*, 2024, v. 15, 416–434.

Ultrafaint Dwarf Galaxies and the Baryonic Tully-Fisher Relation (BTFR) Derived by Quantum Celestial Mechanics (QCM)

Franklin Potter
Huntington Beach, CA USA. E-mail: frank11hb@yahoo.com

All rotationally supported galaxies such as Andromeda and the Milky Way obey the baryonic Tully-Fisher relation (BTFR) of $V_f^4 \propto M_b$ for rotational velocity V_f and detected amount of baryonic mass M_b, as do all the pressure supported dwarf galaxies. However, the ultrafaint dwarf galaxies in the Local Group do not obey BTFR. Including dark matter does not resolve the issue. We investigate whether Quantum Celestial Mechanics (QCM) with its detailed derivation of the BTFR offers a reasonable resolution.

1 Introduction

At least three general types of galaxies are known: rotationally supported galaxies such as Andromeda and the Milky Way, pressure supported dwarf galaxies, and ultrafaint dwarf galaxies. The rotationally supported galaxies obey the original 1977 Tully-Fisher relation connecting their luminosity L to their outer circular velocity V [1]

$$L = V^\alpha \,, \tag{1}$$

where α is a constant that is dependent upon the specific physical properties of each galaxy and the physics model.

When more data became available in the 1990s, the baryonic Tully-Fisher relation (BTFR) determined by MOdified Newtonian Dynamics (MOND) revealed that the flat rotation velocity V_f of a rotationally supported galaxy such as Andromeda or the Milky Way depends upon its baryonic mass M_b exactly to the 4th power, i.e. $V_f^4 \propto M_b$. This relationship even holds true for dwarf galaxies that are pressure supported [2]. Or, as it is more commonly expressed [3],

$$V_f \propto M_b^{\frac{1}{4}} \,. \tag{2}$$

However, for the numerous ultrafaint dwarf galaxies of low mass with no gas component that surround the Milky Way and are gravitationally bound collections of stars only, the BTFR appears to fail [4]. The rotation velocities are too great for the amount of detected baryonic mass. Hence the possibilty exists for a significant amount of dark matter in addition to baryonic mass in their location.

In Fig. 1 are shown some of the many rotationally supported galaxies (circles), some of the numerous pressure supported galaxies including some dwarf galaxies (diamonds), and a representative sample of the ultrafaint dwarf galaxies (squares) with their very large uncertainties because of difficulties in their measurement [5]. These ultrafaints are usually too faint to be detected beyond the nearby Universe, so the sample is largely limited to the Local Group.

The straight line in Fig. 1 is the BTFR fit of the rotationally supported galaxies and the pressure supported galaxies, both of which contain a significant amount of baryonic gas among the stars, as determined [2,6] by MOdified Newtonian Dynamics (MOND) to be

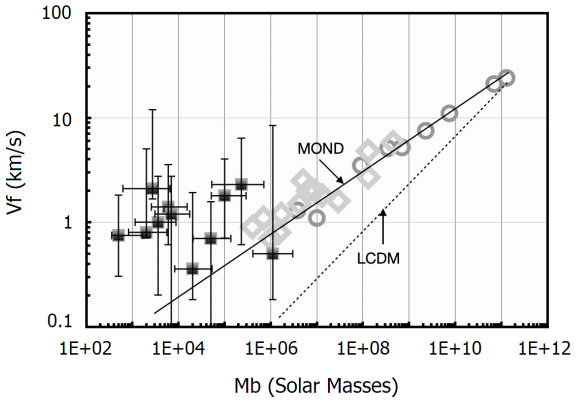

Fig. 1: $\log V_f$ vs. $\log M_b$ for rotationally supported galaxies (circles), pressure supported dwarf galaxies (diamonds), and ultrafaint dwarf galaxies (squares) in relation to the MOND predicted BTFR (straight line) at exactly V_f^4 vs. M_b, plus an example of a ΛCDM prediction (dashed line). The top two circles are Andromeda and the Milky Way. Uncertainties not shown are approximately symbol size.

$$V_f = \left(0.379\,\mathrm{km\,s^{-1}}\, M_{Sun}^{-\frac{1}{4}}\right) M_b^{\frac{1}{4}} \,. \tag{3}$$

But the ultrafaint dwarf galaxies (black squares) do not obey this BTFR relationship. Both MOND researchers and traditional lambda cold dark matter (ΛCDM) research groups have not been able to resolve this issue except by proposing that perhaps the Milky Way itself is possibly interfering with the stability of the ultrafaint systems., i.e. tidal disruptions from external gravitational field effects could be influencing a dispersion of the stars.

Moreover, the ΛCDM approach also has the fundamental problem that one cannot predict the 4th power relationship between the V_f and the baryonic mass M_b because the included dark matter in their galaxy models suggests the power relationship to be smaller than 4 as shown by the dashed line in Fig. 1.

However, the BTFR derived in quantum celestial mechanics (QCM) [7] offers a possible solution that explicitly includes more fundamental physical properties of the ultrafaint dwarf galaxies, including their baryon densities, radial sizes, and total angular momentum.

The successful application of QCM to galaxy clusters [8] explained how the dynamic baryon mass of a galaxy cluster, without requiring any dark matter, depends upon both the total angular momentum and the observed baryonic mass values. Therefore, we investigate the QCM expression for the BTFR to better understand the ultrafaint dwarf galaxies.

2 QCM derivation of the BTFR

QCM is derived from the general relativistic Hamilton-Jacobi equation [7]

$$g^{\alpha\beta}\,\frac{\partial S}{\partial x^{\alpha}}\,\frac{\partial S}{\partial x^{\beta}}\,-\mu^2c^2=0 \tag{4}$$

via the transformation that defines the wave function

$$\Psi = e^{S'/H} \tag{5}$$

to obtain a scalar gravitational wave equation (GWE)

$$g^{\alpha\beta}\,\frac{\partial^2\Psi}{\partial x^{\alpha}\partial x^{\beta}}\;+\;\frac{\Psi}{H^2}=0\,. \tag{6}$$

In these equations, S' is the classical action S divided by μc for a test particle of mass μ, with c being light speed in vacuum.

The characteristic distance H for a gravitationally bound system is defined to be

$$H=\frac{L_T}{M_T c} \tag{7}$$

where L_T is the total angular momentum for the system of total mass M_T.

In a gravitationally bound system in coordinates (t, r, θ, ϕ) obeying the Schwarzschild metric, as expected for planetary systems and galaxies, from the angular coordinates one derives the angular momentum *per unit mass* quantization condition

$$\frac{L}{\mu}=m\,\frac{L_T}{M_T} \tag{8}$$

for a mass μ in orbit with angular momentum L and for m an integer. All confirmed multi-planetary systems obey this relationship [9].

From the radial equation one obtains the energy *per unit mass* quantization

$$E=-\mu c^2\,\frac{r_s^2}{8n^2H^2}\,, \tag{9}$$

with r_s the Schwarzschild radius and integer n.

Application of the virial theorem for gravitation leads directly to the tangential rotation velocity for the test particle

$$v=\frac{r_s c}{2nH} \tag{10}$$

from which the QCM predicted BTFR can be derived.

If we assume that the galaxy is approximately a disc with a total baryonic mass $M_b = \pi h R^2\rho_0$ for average density ρ_0, thickness h, and radius R, then its total angular momentum $L_T = \alpha M_b R^2\omega$ with moment of inertia factor α and rotational velocity ω. With gravitational constant G, this BTFR becomes

$$V_f = M_b^{\frac{1}{4}}\,\sqrt{\frac{G}{n\alpha}}\,\sqrt{\pi h\rho_0}\,. \tag{11}$$

As one example, suppose h is 8 times greater than estimated, and the α and ρ_0 parameters can each vary by about a factor of 2. By combining them optimally, QCM predicts a maximum gain of about $\sqrt{8}$ times the previous value of V_f for the same baryonic mass value.

3 Conclusion

QCM predicts a BTFR relation depending upon the average density, thickness, and total angular momentum of a galaxy. Whether these three parameters in the BTFR expression derived by QCM will resolve the issue of the ultrafaint dwarf galaxy positions on the $V_f^4 \propto M_b$ graph remains to be determined when better data becomes available.

Acknowledgements

We thank physics colleagues for continuing encouragement to apply QCM to astronomical issues.

Received on November 4, 2025

References

1. Tully R. B. and Fisher J. R. A new method of determining distances in galaxies. *A&A*, 1977, v. 54, 661–673.
2. McGaugh S. S. *et al.* The Baryonic Tully-Fisher Relation in the Local Group and the Equivalent Circular Velocity of Pressure-Supported Dwarfs. *AJ*, 2021, v. 162, 202.
3. Schombert J., McGaugh S., and Lelli F. Using the Baryonic Tully-Fisher Relation to Measure H_0. *AJ*, 2020, v. 160, 71.
4. Ruan D. *et al.* Predictions for detecting a turndown in the baryonic Tully-Fisher relation. *MNRAS*, 2025, v. 541 (3), 2180–2196.
5. Durbin M. J. *et al.* The HST Legacy Archival Uniform Reduction of Local Group Imaging (LAURELIN) I. Photometry and Star Formation Histories for 36 Ultra-faint Dwarf Galaxies. *AJ*, 2025, v. 992, 106.
6. Milgrom M. The deep-MOND limit – a study in primary and secondary predictions. arXiv: gr-qc/2510.16520.
7. Preston H. G. and Potter F. Exploring large-scale gravitational quantization without $\hbar$ in planetary systems, galaxies, and the Universe. arXiv: gr-qc/0303112.
8. Potter F. Galaxy Clusters: Quantum Celestial Mechanics (QCM) Rescues MOND? *Prog. in Phys.*, 2024, v. 20 (2), 100–102.
9. Potter F. Predicting Total Angular Momentum in TRAPPIST-1 and Many Other Multi-Planetary Systems Using Quantum Celestial Mechanics. *Prog. in Phys.*, 2018, v. 14 (3), 115–120.

The Model of the Sun, Based on Wheeler's Geometrodynamics, is Confirmed by Recent Astronomical Observations

Anatoly V. Belyakov
Tver, Russia. E-mail: belyakov.lih@gmail.com

The detailed physical parameters of the gravitomagnetohydrodynamic model of the Sun, calculated earlier on the basis of Wheeler's geometrodynamics, are confirmed by recent astronomical observations.

In [1] and other studies, a mechanistic interpretation of Wheeler's geometrodynamics is used, which makes it possible to draw analogies between objects of different scales (in the widest range from elementary particles to planets and stars), regardless of the nature of their constituent environment, solely on the basis of the balance between gravitational, magnetic, electrical, and dynamic forces. This method, when applied to stellar objects, has showed that the Sun has a complex dynamic internal structure, and some of its model parameters are in good agreement with recent astronomical observations [2–4].

The balances of the aforementioned forces lead to the structuring of any medium, if these forces are present, into local vortex zones (vortex tubes) [1, 5], consisting of single vortex filaments.

Recall that the formulae for electric and magnetic forces are written in a "non-Coulomb" form, in which the electric charge is replaced by the electron's maximum momentum. In this case, the electric and magnetic constants ε_0 and μ_0 are as follows

$$\varepsilon_0 = \frac{m_e}{r_e} = 3.33 \times 10^{-16} \text{ kg/m}, \tag{1}$$

$$\mu_0 = \frac{1}{\varepsilon_0 c^2} = 0.0344 \text{ 1/N}, \tag{2}$$

so ε_0 is effectively the linear density of the vortex tube, and μ_0 is the reciprocal of the centrifugal force generated by the rotation of a vortex tube element of mass m_e at the speed of light c along a radius r_e.

In particular, the work [1] established that as an initially structureless medium becomes more complex, local vortex zones arise, where:

— the number z of the local zones for an arbitrary mass M is

$$z = \frac{1}{M^{1/4}}, \tag{3}$$

— their radius r and length l, respectively, are

$$r = M^{3/4} R_c, \tag{4}$$

$$l = M^{1/4} R_c, \tag{5}$$

— the circumferential velocity of individual vortex filaments rotating around the longitudinal axis of the vortex tubes is

$$v_0 = M^{1/4} c, \tag{6}$$

— the number of the vortical filaments in the zone

$$n = f M, \tag{7}$$

where f is the ratio of the electric forces to the gravitational ones, and M is a dimensionless mass measured in fractions of the characteristic mass

$$M_m = \frac{R_c c^2}{\gamma} = 1.012 \times 10^{36} \text{ kg}, \tag{8}$$

where the characteristic radius R_c is

$$R_c = (2\pi)^{1/2} c \times [\text{sec}] = 7.52 \times 10^8 \text{ m}, \tag{9}$$

so that for the Sun's mass is we have $M = 2 \times 10^{-6}$. It is obvious that as its own mass decreases, the object simultaneously becomes more complex, structuring itself into local zones in an increasingly finer manner.

Stars, forming from primordial matter, undergo a long evolutionary process, and at some point their structure conforms to the above relationships (for detail, see [1]). It is assumed that our Sun is also at this equilibrium stage of its existence, and therefore some parameters of the solar structure should correspond to them.

According to [1], the initial state of a stellar object is assumed to be a rotating disk, in which, as it becomes more complex, local radial-spiral zones form, which are pulled toward the centre by the radial components of gravitational forces.

Since magnetic forces also act in the solar plasma, the solar structure as a whole may consist of local zones in the form of closed contours-toroids (balance of magnetic and gravitational forces), whose conductive elements (vortex filaments) rotate around the closed axis of the torus (balance of magnetic and inertial forces), while the toroids themselves are located in the plane of the rotating disk (balance of gravitational and inertial forces). The core rotates faster than the periphery, and the toroids twist, converting their kinetic energy into other forms (and then, obviously, the reverse process). It would be a gross oversimplification to liken this system to a multi-winding, flat-spiral mechanical pendulum; nevertheless, an

oscillatory process of the object's gravimagneticodynamic structure must take place.

Indeed, paired dark spots predominantly in the Sun's equatorial zone appear to be the outcrops of local structures that undergo magnetization reversals and change their intensity and polarity with a period of 11 years. Their observed number (from a few to hundreds) is consistent with the calculated average, according to formula (3), $z = 26.6$. In [1] other models corresponding to the real parameters of the Sun are also given.

This structure turned out not to be speculative; on the contrary, it has received new direct confirmation in the recent studies mentioned below.

1. The Daniel K. Inouye Solar Telescope registered tiny structures in the Sun's corona — ultra-thin coronal loops that extend along the Sun's magnetic field lines. On average, their width was approximately 48 kilometers across, with individual loops measuring approximately 20 km [2]. It is assumed that these fine structures may be isolated elements of the solar structure.

But this is precisely the size of the vortex local zones predicted by the proposed model; according to the formulae (4) and (5), $r = 40.4$ km and $l = 28,200$ km. The latter is also consistent with observations, since the height of coronal loops can reach 10,000 km.

2. Furthermore, Prof. Richard Morton directly observed a small twisted type of wave (Alfvén waves), which can supply energy to the corona [3]. These waves cause rotational motion, which was detected by spectroscopic analysis, as the plasma's erruption toward and away from the Earth creates characteristic red and blue shifts on opposite sides of magnetic structures. This effect was observed in the movement of iron atoms heated to 1.6×10^6 °C in the corona.

But it is precisely this vortex motion that the individual filaments that make up the toroids exhibit; their circumferential velocity, according to (6), is $v_0 = 11.3 \times 10^6$ m/sec. During solar flares, the filaments are broken, causing the charged particles that comprise them to split off and rush into space at a velocity v_{0i}, which then decreases in the Sun's gravitational field to the speed in the range of 1,000–3,000 km/sec recorded at Earth.

3. Astronomers using the European Southern Observatory's (ESO) Very Large Telescope (VLT) observed the initial phase of the supernova explosion SN 2024ggi in the galaxy NGC 3621 [4]. It was discovered that the initial mass ejection was not spherical, but rather elongated and flattened. This fact also confirms the correctness of the **initial structure assumed for the star as a flat disk**.

It should also be noted that the proposed model makes it possible to directly calculate the atomic number of the element at which nuclear reactions in stars cease at the end of their evolution, namely, the atomic number of iron.

In [1], when determining the parameters of a spirally structured disk, its radius in a compressed state was determined, i.e., the radius of the star's core

$$R_0 = M^{1/3} R_c \,, \tag{10}$$

and, subsequently, the core density.

In the atoms of stellar matter (mainly hydrogen), the substance, according to the electron model [6], circulates along p^+-e^- contours having a mass $\varepsilon_0 r_0$, and the circulation speed cannot be greater than the speed of light. At the same time, the magnitude of the charge e_0 is constant for any quantum number and is equal to the momentum of the mass of the circuit $\varepsilon_0 r_0 v_0$. When $v_0 \to c$, then $r_0 \to r_{0_{\min}}$, therefore

$$r_{0_{\min}} = \frac{e_0}{\varepsilon_0 c} \,. \tag{11}$$

The density of extremely compressed hydrogen atoms is (for a spherical volume)

$$\rho_{\max} = \frac{3 m_{\mathrm{H}}}{4\pi r_{0_{\min}}^3} = 8.82 \times 10^7 \text{ kg/m}^3, \tag{12}$$

where m_{H} is the mass of a hydrogen atom.

Assuming that all matter is concentrated in the nucleus, its density is the ratio of the mass of the nucleus to the cube of its radius and, according to the formulae (8) and (10),

$$\rho_0 = \frac{M M_m}{R_0^3} = \frac{M_m}{R_c^3} = \\ = \frac{1}{2\pi\gamma \times [\sec^2]} = 2.38 \times 10^9 \text{ kg/m}^3. \tag{13}$$

That is, the core density depends only on the gravitational constant. From the $\rho_0/\rho_{\max}$ ratio, it follows that a volume equal to the volume of one compressed hydrogen atom should contain 27 atoms of the star's original material, which, in terms of proton number, corresponds to iron-group atoms. This density is typical of white dwarfs.

Thus, the highly simplified model of solar structure presented in [1] is consistent with the external manifestations of solar activity. As for the commonly used spherically symmetric quasi-static model of stellar structure, which analyzes the state of matter and pressure, temperature and luminosity as functions of radius, it is clearly insufficient, and an analysis of the Sun's gravitomagnetodynamic structure should be included.

And finally: the more complex than expected structure of stellar objects, where the dynamics of magnetic forces play a huge rôle, suggests the following idea: are enormous pressures and temperatures alone enough to trigger a controlled thermonuclear reaction?

Received on November 18, 2025

References

1. Belyakov A.V. Evolution of stellar objects according to J. Wheeler's geometrodynamic concept. *Progress in Physics*, 2013, v. 9, issue 1, 25–40.

2. Tamburri C.A., Kazachenko M.D., Cauzzi G., *et al*. Unveiling unprecedented fine structure in coronal flare loops with the DKIST. *The Astrophysical Journal Letters*, 2025, v. 990(1), L3.
3. Morton R.J., Gao Y., Tajfirouze E., Tian H., *et al*. Evidence for small-scale torsional Alfven waves in the solar corona. *Nature Astronomy*, 24 October 2025.
4. Yi Yang, Xudong Wen, Lifan Wang, *et al*. An axisymmetric shock breakout indicated by prompt polarized emission from the type II supernova 2024ggi. arXiv: 2511.08824 (2025).
5. Belyakov A.V. On materiality and dimensionality of the space. Is there some unit of the field? *Progress in Physics*, 2014, v.10, issue 4, 203–206.
6. Belyakov A.V. Charge of the electron, and the constants of radiation according to J. A. Wheeler's geometrodynamic model. *Progress in Physics*, 2010, v. 6, issue 4, 90–94.

Progress in Physics is an American scientifc journal on advanced studies in physics, registered with the Library of Congress (DC, USA): ISSN 1555-5534 (print version) and ISSN 1555-5615 (online version). The journal is peer reviewed.

Electronic version of this journal:
http://progress-in-physics.com